**Department of Aeronautical
and Vehicle Engineering**

EXPANDING THE BRUSH TIRE MODEL FOR ENERGY STUDIES

Author:
Francesco Conte

Supervisor:
Mohammad Mehdi
Davari

June 2014

Abstract

Considering the more and more important issues concerning the climate changes and the global warming, the automotive industry is paying more and more attention to vehicle concepts with full electric or partly electric propulsion systems. The introduction of electric power sources allow the designers to implement more advanced motion control systems in vehicle, such as active suspensions. An example of this concept is the *Autonomous corner module (ACM)*, designed by S. Zetterström. The ACM is a modular based suspension system that includes all features of wheel control, such as control of steering, wheel torque and camber individually, using electric actuators. With a good control strategy it is believed that is it possible to reduce the fuel consumption and/or increase the handling properties of the vehicle.

In particular, camber angle has a significant effect on vehicle handling. However, very few efforts have been done in order to analyse its effects on tire dissipated energy.

The aim of this study is to develop a new tire model, having as starting point the simple Brush Tire model, in order to analyse the tire behaviour, in terms of forces generated and energy dissipated, for different dynamic situations. In order to reach this scope, the characteristic equations of the rubber material are implemented in a 3D Multi-Line brush tire model. In this way the energy dissipated, thus the rolling resistance force, can be studied and analysed, considering also the tire geometry.

From the results of this work it is possible to assert that the angular parameters (e.g. camber angle) affect the power losses in rolling tires, as well as the tire geometry influences their rolling resistance. Thus, using a good control strategy, it is possible to reduce the power losses in tires.

Keywords: Multi-Line Brush Tire model, Masing model, rolling resistance.

Acknowledgments

This master thesis was performed at the department of Aeronautical and Vehicle Engineering, KTH Royal Institute of Technology in Sweden, during the spring of 2014.

Firstly, I would like to thank my supervisor Mohammad Mehdi Davari, for his tireless help during all the duration of the work. Secondly, I would like to thank professors Lars Drugge and Jenny Jerrelind for their classes during my academic year spent at KTH. The final thanks is addressed to my supervisor at my home university, professor Alessandro Vigliani, for his help and suggestions.

Contents

List of Figures ix

Nomenclature xiii

1 Introduction 1
- 1.1 Background 1
- 1.2 Outline of the thesis 2

2 Fundamentals of tire dynamics 3
- 2.1 Kinematics 3
- 2.2 Tire mechanics 5
  - 2.2.1 Rolling resistance 5

3 Existing tire models 7
- 3.1 Magic Formula model 8
- 3.2 Brush Tire model 10
- 3.3 Conclusion 13

4 Rubber properties and modelling 15
- 4.1 Mechanical properties 15
- 4.2 Modelling of the rubber compound 16
  - 4.2.1 Visco-elastic force 16
  - 4.2.2 Friction force 19
- 4.3 Rubber model used in this work 22
- 4.4 Conclusion 23

5 Development of a Multi-Line Brush Tire model 25
- 5.1 Introduction 25
- 5.2 Geometry 25
- 5.3 Outline of the code 27
- 5.4 Dynamics 29
- 5.5 Sliding region 31
- 5.6 Load sensitivity factors 36
- 5.7 Quarter car model 36
- 5.8 Flexible lateral carcass 39
- 5.9 Energy and work 41
  - 5.9.1 External losses 41

5.9.2 Internal losses 41
5.10 Conclusion 43

6 Validation and results 45
6.1 Validation 45
6.1.1 Comparison with Magic Formula 45
6.1.2 Comparison with experimental data 47
6.2 Results 48
6.2.1 Effect of camber 48
6.2.2 Combined slip 49
6.2.3 Self-aligning torque 53
6.2.4 Rolling resistance 54
6.2.5 Energy losses 59

7 Conclusions and recommendations 69
7.1 Conclusions 69
7.2 Drawbacks 70
7.3 Recommended future work 70

Bibliography 71

A Force code implementation 73
A.1 Visco-elastic force 73
A.2 Friction force 74

B Magic Formula Tire Model implementation 77
B.1 Longitudinal slip 77
B.2 Lateral slip 77

C Pirelli test, Multi-Line Brush Tire model coefficients 79

List of Figures

2.1 Wheel axis coordinate system ISO 8855 [2] 3
2.2 Kinematics of the wheel during braking and cornering 4
2.3 Forces acting on a free rolling tire 6

3.1 Tire models categories 7
3.2 Magic Formula factors [7] 9
3.3 Aligning torque behaviour, Magic Formula [6] 10
3.4 Brush tire model, deformation of the tire rubber (Top: side view; bottom: top view 11

4.1 Typical hysteresis loop of a harmonically excited rubber. Sinusoidal excitation with three different amplitudes. A lower frequency (1 Hz) has been set in 4.1a than in 4.1b (10 Hz) 15
4.2 Maxwell visco-elastic model. Frequency analysis (Bode diagram), $k = 1000$ N/m, $c = 10$ Ns/m 17
4.3 Kelvin-Voigt visco-elastic model. Frequency analysis (Bode diagram), $k = 1000$ N/m, $c = 10$ Ns/m 18
4.4 Three parameter maxwell visco elastic model. Frequency analysis (Bode diagram), $k_1 = 1000$ N/m, $k_2 = 1000$ N/m, $c = 10$ Ns/m 19
4.5 Scheme of the generalized Maxwell model 19
4.6 Discrete masing model 21
4.7 Force displacement loop of Masing friction model with five Jenkin elements. 21
4.8 Berg model, [16] 22
4.9 *Rubber element*, on the left the visco-elastic part is represented by a Three Parameters Maxwell model, on the right the friction part is represented by the five elements Masing model 23
4.10 Dynamic response of the rubber element for two sinusoidal inputs 24

5.1 Representation of the model with 7 lines 26
5.2 Front view of the wheel 27
5.3 Side view of the wheel 28
5.4 Phases order in the Multi-Line Matlab code for each *dt* interval time 28
5.5 Dynamic friction model, $\mu_s = 1.1$, $\mu_c = 0.9$, $v_{str} = 3.5$ m/s . . . 32

5.6 Diagram longitudinal slip - longitudinal force, comparison between a constant friction coefficient and a dynamic friction function, described by Equation 5.20 34
5.7 Longitudinal deflection of the bristles, $\kappa_x = 0.07$, difference between the deformation calculated by using Equation 5.25 (solid line) and the deformation calculated without considering the sliding region (dashed line) 34
5.8 The deflection process along the x-axis, adhesion region 35
5.9 Dependence of the force generated on the total vertical load . . 37
5.11 Flexible carcass (dashed line) and stiff carcass (solid line), $F_y = -4050$ N 40
5.12 Carcass deformation for (a) cambered wheel and for (b) not cambered wheel 40

6.1 Longitudinal force vs longitudinal slip, comparison between Magic Formula Tire model (red lines) and Multi-Line Brush model (blue lines) for different vertical load on the wheel 46
6.2 Lateral force vs side slip, comparison between Magic Formula Tire model(red line) and Multi-Line Brush Tire model (blue line) for different loads on the wheel 46
6.3 Comparison between experimental data (marker) and Multi-Line Brush Tire model (Red line) for $\alpha = -2°$ 47
6.4 Comparison between experimental data (marker) and Multi-Line Brush Tire model (Red line) for $\alpha = 4°$ 48
6.5 Lateral force for different camber angles 49
6.6 Lateral force distribution on the contact patch for (a) non-cambered wheel (a) and (b) for a positive cambered wheel, both for $\alpha = 5.7°$ ($n = 100$, $l = 25$) 50
6.7 Lateral force vs camber angle for $\alpha = 11.5°$ in (a); camber thrust ($\alpha = 0°$) for different camber angles γ in (b). 50
6.8 Contact patch with sliding region in pink in 6.8a and 6.8b; frontal view of half wheel in 6.8c and 6.8d, $F_z = 4$ kN, $\alpha = 3°$ 51
6.9 Combined slip for $\gamma = 0°$ 52
6.10 Longitudinal force with fixed slip angle and various camber angles 53
6.11 Lateral force with fixed longitudinal slip and various camber angles 53
6.12 Self aligning torque M_z for different vertical loads 54
6.13 Vertical force distribution ($n = 100$, $l = 25$) in 6.13a; internal friction forces using Masing model in 6.13b, for one single line . 55
6.14 Dependence of the rolling resistance on the vertical load F_z in 6.14a; Dependence of the rolling resistance on the vertical stiffness in 6.14b 56
6.15 Dependence of the rolling resistance coefficient on the longitudinal speed 57
6.16 Rolling resistance coefficient for different viscous coefficient in the z-axis 57

6.17 Rolling resistance dependence on camber angle, for two different vertical tire values of stiffness 58
6.18 Energy dissipation rate by friction elements along the z-axis for different vertical loads 59
6.19 Energy dissipated along the lateral direction in the time interval dt, $\alpha = 7°$ 60
6.20 Total internal power loss and internal friction power loss for different side slip angle α and camber angle γ along the lateral direction 61
6.21 Total internal friction force normalized on the lateral force . . . 62
6.22 Longitudinal friction power loss $\dot{W}_{f,x}$ in 6.22a, normalized with the wheel rotational speed ω in 6.22b 62
6.23 Sliding energy in the x-axis in 6.23a, in the lateral direction in 6.23b 63
6.24 Sliding power along the y-axis for a side slip angle $\alpha = 3°$ 64
6.25 Power dissipated by lateral sliding for different camber angles . 65
6.26 Sliding power distribution for $\kappa_x = 40\%$ 65
6.27 Longitudinal input, output and sliding power. 66
6.28 Tire efficiency for different slip ratio 67

Nomenclature

α	Side slip angle
α_0	Inclination of the sidewall tire
$\bar{\varphi}$	Angular coordinate of the bristles
$\bar{v} = (v_x, v_y)$	Velocity vector of the wheel center
$\bar{v}_s$	Vector of the slip velocity
β	Angle of the slip velocity vector
$\ddot{z}_t$	Vertical acceleration of wheel center
$\ddot{z}$	Vertical acceleration of sprung mass
$\delta_{a,x}$	Bristle deformation along the x-axis in the adhesion region
$\delta_{a,y}$	Bristle deformation along the y-axis in the adhesion region
$\delta_{s,x}, \delta_{s,y}$	Bristle deformation in the sliding region
δ_{xb}	Deformation along the x-axis of the bristle
δ_{yb}	Deformation along the y-axis of the bristle
$\dot{\Psi}$	Yaw rate
$\dot{W}_{f,x}$, $\dot{W}_{f,y}$, $\dot{W}_{f,z}$	Dissipated energy rate by internal friction along the x-, y- and z-axis direction
$\dot{W}_{t,x}$, $\dot{W}_{t,y}$, $\dot{W}_{t,z}$	Total energy rate (power) dissipated by viscous and friction forces along the x-, y- and z-axis
$\dot{z}_t$	Vertical velocity of wheel center
$\dot{z}$	Vertical velocity of sprung mass
γ	Camber angle
κ_x	Longitudinal slip
λ	Angular deflection of the carcass
μ	Friction coefficient between bristle and road
μ_x	Longitudinal friction coefficient between road and tire
μ_y	Lateral friction coefficient between road and tire

$\mu_{c,x}, \mu_{c,y}$	Dynamic friction coefficient, along x- and y-axis respectively
$\mu_{s,x}, \mu_{s,y}$	Static friction coefficient, along x- and y-axis respectively
ω	Angular wheel speed
ω_0	Wheel angular speed for free rolling
σ	Strain in the rubber compound
θ'	Segment angle
ε	Deformation in the rubber compound
B	Width of tire
b	Width of the tire tread in the X_W, Y_W, Z_W system
B, C, D, E	Magic Formula coefficients
c	Viscous element in the three parameters Maxwell model
c_{px}	Longitudinal stiffness of the bristle in the simple Brush Tire model
c_{py}	Lateral stiffness of the bristle in the Simple Brush Tire model
d_r	Torsional damping of the flexible carcass
df'_z	Normalized vertical load change for each contact line
dx	Longitudinal incremental deformation of the bristle
dy	Lateral incremental deformation of the bristle
e	Distance between the vertical load acting on the wheel center and the vertical load acting in the contact patch
F_e	Elastic force in the rubber compound
F_f	Friction force in the rubber compound
F_i	Force acting on each Jenkin element in the Masing model
F_R	Rolling resistance force
f_r	Rolling resistance coefficient
F_v	Viscous force in the rubber compound
F_x	Longitudinal force acting on the contact patch
f_x	Longitudinal force matrix
F_y	Lateral force acting on the contact patch
f_y	Lateral force matrix
F_z	Vertical force acting on the contact patch

f_z	Vertical force matrix
f_{rubber}	Force function of the rubber element
$f_{s,x}, f_{s,y}$	Forces in the sliding region
F_{ve}	Visco-elastic force in the rubber element
F_{z0}	Nominal vertical load on the wheel
F'_{z0}	Total vertical load divided by the number of lines
g	Gravity acceleration
k	Elastic stiffness in the three Parameters Maxwell model
k_r	Torsional stiffness of the flexible carcass
l	Number of longitudinal lines in the Multi-Line model
l_s	Sensitive load coefficient
$l_{z,x}$, $l_{z,y}$	Vertical load sensitivity factors
M_x	Overturning torque on the wheel center
M_y	Driving torque acting on the wheel center
M_z	Self-aligning torque acting on the wheel center
m_{sprung}	Sprung mass
$m_{unsprung}$	Unsprung mass
$M_{y,w}$	Effective driving torque on the wheel plane
M_{zr}	Residual torque, for the Magic Formula model
n	Number of rubber elements for each longitudinal line in the Multi-Line model
$p_{s,x}$, $p_{s,y}$	Power dissipated by each bristle in the longitudinal and lateral direction respectively
P_s	Total power dissipated by sliding in the contact patch
R_0	Static tire radius, i.e. unloaded wheel radius
R_e	Effective rolling tire radius
R_i	Adhesive force in the Masing model
R_r	Tire rim diameter
R_w	Radius of the tire tread in the X_W, Y_W, Z_W system
R_{mean}	Mean radius of the wheel
s_r	Percentuage ratio of the sidewall height
S_V, S_H	Magic Formula shifting coefficients

s_w	Sidewall height
t	Time
t_p	Pneumatic trail
v_c	Circumferential speed of the wheel
v_x	Longitudinal velocity of the wheel center
v_y	Lateral velocity of the wheel center
$v_{\delta_{a,x}}$	Longitudinal deformation speed of the bristle in the adhesion region
$v_{\delta_{a,y}}$	Lateral deformation speed of the bristle in the adhesion region
$v_{s,x}$	Longitudinal slip velocity
$v_{s,y}$	Lateral slip velocity
$v_{slid,x}$	Longitudinal sliding velocity of a bristle
$v_{slid,y}$	Lateral sliding velocity of a bristle
$v_{str,x}, v_{str,y}$	Stribeck velocity in the tread-road friction model
W_s	Work made by the sliding forces
$W_{f,x}$, $W_{f,y}$, $W_{f,z}$	Total energy dissipated by internal friction along the x-,y- and z-axis direction
$w_{f,x}$, $w_{f,y}$, $w_{f,z}$	Internal friction work made by each bristle along the x-, y- and z-axis direction
$W_{t,x}$, $W_{t,y}$, $W_{t,z}$	Total energy dissipated by viscous and friction forces along the x-, y- and z-axis
$w_{t,x}$, $w_{t,y}$, $w_{t,z}$	Energy dissipated by viscous and friction forces in each bristle along the x-, y- and z-axis
$x_2, F_{f,max}$	Parameters in the Berg model
X_R, Y_R, Z_R	Right-handed orthogonal axis system, centered in the contact patch
x_s, F_s	Reference state in the Berg model
X_W, Y_W, Z_W	Right-handed orthogonal axis system, centered in the wheel center
z	Vertical coordinate of sprung mass
z_t	Dynamic tire radius, z coordinate of the center wheel in X_R, Y_R, Z_R

Chapter 1

Introduction

1.1 Background

The car is one of the most common means of transport in the last decades. According to *Ward's* research, the number of vehicles in operation worldwide surpassed the one billion unit mark in 2010 for the first time ever [1]. It is one of the symbols of the country's financial resources, and its number is in perpetual growth. The vehicle propulsion is provided by an engine or motor, usually by an internal combustion engine, or an electric motor, or a combination of the two, such as hybrid electric vehicles. The commercial drilling and production of petroleum began during the mid-1850's, thus the internal combustion engine became the predominant mode of propulsion, due to the extremely high energy density of the liquid fossil fuel.

During the last two decades, the climate change issues, to which the vehicle emissions play an important role in the formation of the greenhouse gases, and the diminishing fossil fuel resource become problems of primary importance. The future trends of the new vehicle concepts seems to go towards the complete, or partial, electrification of the propulsion system. Thanks to the introduction of electric power source, more advanced motion control systems, such as active suspension and individual wheel control, can be implemented, by the increasing use of electric actuators. Consequently, various chassis strategy and suspension control systems can be implemented in the vehicle, in order to optimize performance and fuel consumption.

The camber angle, γ, denotes the outward angular lean of the wheel plane relative to the vehicle reference frame [2]. In conventional vehicles (cars, trucks) the camber angle is small, and it is function of the suspension design. However, electrification of vehicle actuators enable active control of camber angles instead of passively tilting the wheel, according to suspension geometry. One example of a suspension system realized with active camber control is the *Autonomous corner modul* (ACM), designed by S. Zetterström in 1998 [3]. The ACM is a modular based suspension system that includes all features of wheel control, such as control of steering, wheel torque and camber individually.

The aim with this work is to investigate and get increased understanding of the effect of camber as well as different operating conditions on the energy dissipation in rolling tires, using a dynamic model, typical of studies concerning the *rubber* behavior. It is motivated by the constant research on the minimization of the energy needed to move vehicles.

1.2 Outline of the thesis

The work is divided in seven chapters: in the first one the background and the motivations of this work are explained; in Chapter 2 the fundamental notions about tire and tire dynamics are briefly described, including the wheel axis system used in the thesis; in Chapter 3 the two most famous and utilized tire models are described and commented, the Magic Formula and the Brush Tire model; the mechanics of rubber and its modelling are discussed in Chapter 4, where the rubber model used in the work is discussed and analysed; in Chapter 5 the Multi-Line Brush tire model is derived, explaining all the factors and the dynamics involved; the validation and the results coming from the model are discussed in Chapter 6. Finally, in Chapter 7, some conclusions of the work is made as well as some recommendations for future work.

Chapter 2

Fundamentals of tire dynamics

In this chapter a brief review of the fundamental aspects of wheel dynamics and kinematics are shown. But first a brief introduction on axis and coordinate systems is discussed.

It's very important to define correctly the axis coordinate system, in order to avoid misunderstandings about the sign of forces and torques. In literature two main axis orientation exists, both of them *right-handed*: the ISO 8855 [4] and the SAE J670e [5]. In this work the ISO 8855 is taken as reference, it means that the z-axis is pointing up from the ground plane, the x-axis is pointing forward and the y is pointing to the left-hand-side of the vehicle. The X_R, Y_R, Z_R is the right-handed orthogonal axis system whose Z_R axis is normal to the road surface at the center of tire contact, and whose X_R axis is perpendicular to the wheel spin axis Y_W, as shown in Figure 2.1. The camber angle γ is positive if it rotates about X_R axis, and the slip angle α is positive if it rotates about Z_R axis.

2.1 Kinematics

This section deals with the kinematics in tires, and describes the definitions and the notations used in the thesis. The most important entities are illustrated in Figure 2.2. In the figure the vectors are illustrated by a bar over

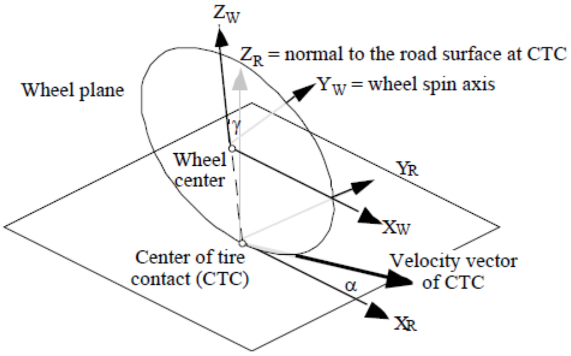

Figure 2.1: Wheel axis coordinate system ISO 8855 [2]

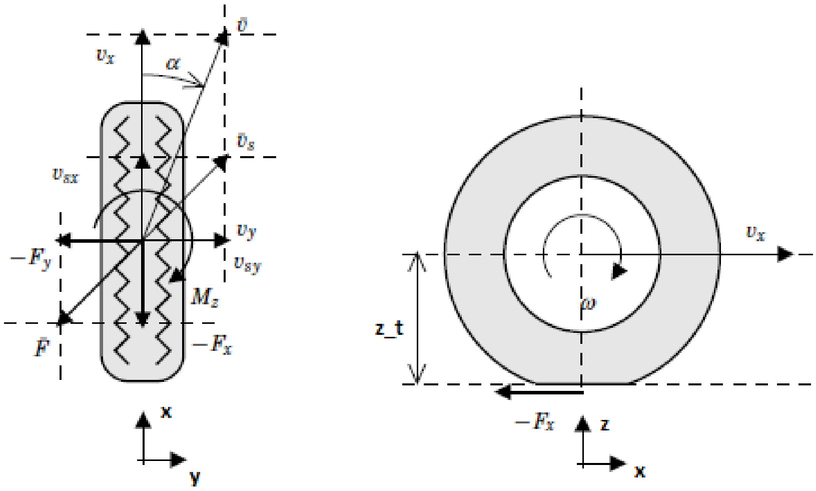

Figure 2.2: Kinematics of the wheel during braking and cornering.
(Left: bottom view; right: side view)

the letter, the magnitude of vectors is expressed by their components. The *wheel travel velocity* is denoted by vector $\bar{v} = (v_x, v_y)$, it is the velocity of the wheel center, different from the X_R axis (longitudinal axis of the wheel plane pointed in the contact patch) by the slip angle α:

$$\tan(\alpha) = \frac{v_y}{v_x} \tag{2.1}$$

The circumferential speed of the wheel is equal to:

$$v_c = \omega R_e \tag{2.2}$$

where ω is the wheel angular velocity, and R_e is the *effective rolling radius*, defined as the ratio $R_e = {}^{v_x}/_{\omega_0}$ between the longitudinal wheel speed and the wheel angular velocity in *free* rolling. It's important to notice that the effective rolling radius R_e is not equal to the height of the center wheel above the ground z_t neither to the wheel unloaded radius R_0, but something in the middle. The difference between z_t and R_e creates a longitudinal slip velocity, that allows the tire to generate a longitudinal force needed to balance the rolling resistance force (this will be discuss in the chpater 5). The *slip velocity* is the relative motion of the tire in contact with the ground in the contact patch. It is defined as:

$$\bar{v}_s = (v_x - v_c, v_y) \tag{2.3}$$

Thus the direction of the vector *slip velocity* is indicated by the angle β, defined as:

$$\tan(\beta) = \frac{v_{s,y}}{v_{s,x}} = \frac{v_y}{v_x - v_c} \tag{2.4}$$

It's common to use the tire slip instead of the slip velocity as variable for studying the forces generation in the contact patch. The tire slip is obtained

Table 2.1: Forces and moments acting on the wheel

Axis	Force	Moment
x	Longitudinal force (F_x)	Overturning torque (M_x)
y	Lateral force (F_y)	Rolling resistance torque (M_y)
z	Vertical force (F_z)	Aligning torque (M_z)

by normalizing the slip velocity with a reference velocity. Three slip definitions are commonly used, based on different reference speed. However, in this work the longitudinal slip κ_x is defined following the ISO 8855 [4]:

$$\kappa_x = \frac{\omega - \omega_0}{\omega_0} = \frac{\omega R_e - v_x}{v_x} \tag{2.5}$$

where ω is the angular velocity of the wheel about its spin axis and ω_0 is the free rolling angular velocity of the wheel that would be measured at zero *slip angle* and zero *camber* angle. It means that ω_0 is the longitudinal velocity of the wheel center divided by the effective rolling circumference of the tire at that speed and load condition. Thus κ_x will be negative for braking operations (negative F_x force) and positive for accelerating operations (positive F_x force).

2.2 Tire mechanics

The forces and torques generated in the contact patch are considered positive if they have the same direction of the axis system of Figure 2.1. The longitudinal force F_x is positive if pointing forward (accelerating wheel), the lateral force F_y is positive if pointing to the left-hand side of the vehicle, and F_z is positive if pointing up. The longitudinal and lateral forces, F_x and F_y, lie on the *road* plane, defined by X_R and Y_R axis respectively. In the same way the generated moments are positive if pointing on the same direction of their reference axis (Table 2.1). Forces and torques are created in the contact patch between wheel and ground by the velocity difference between the *tread* of the wheel and the road. As previously discussed, the velocity difference is expressed by the *slip* parameters, κ_x for longitudinal slip and α for lateral slip. Two different kinds of slip exist: *pure slip* signifies that either α or κ_x are zero, instead *combined slip* means that both α and κ_x have non-zero values. These two different situations will be studied further.

2.2.1 Rolling resistance

When a tire is vertically loaded on a flat surface the greatest part of its deformation will be in the contact region between tire and ground. Thus the circular profile of the tread surface is flattened, the tread elements are compressed and the sidewalls deformed. If the tire then is rolling on the surface, each element of the tread is repeatedly compressed and deformed

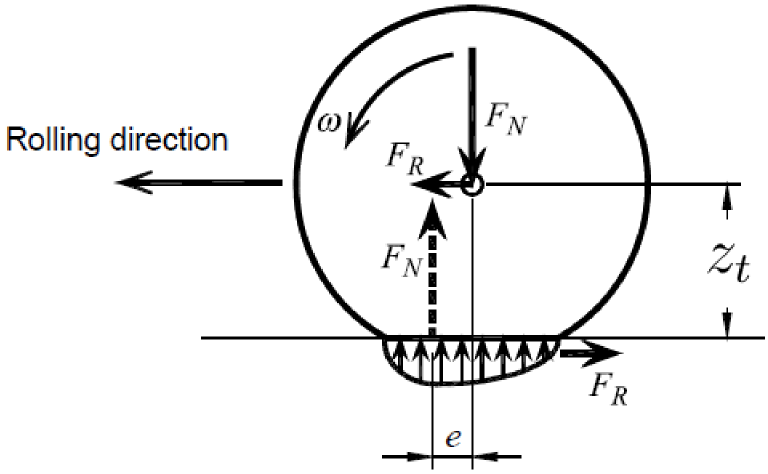

Figure 2.3: Forces acting on a free rolling tire

as it passes through the contact patch. Since the rubber is not a perfectly elastic material, these compression-recovery cycles cause an *internal* energy loss, indeed, the energy used to deform the radial section of the tire doesn't all return when the section takes its original shape. This *internal* energy loss must not be confused with other *external* energy loss sources, such as a deformable road surface (sand or snow) or the slip between road and tire. For a non-rolling tire the vertical pressure distribution on the contact path is symmetric along the longitudinal direction. However, when the tire is rolling this distribution shifts forward, and the center of application is not under the wheel center anymore, but shifted forward at a distance e (Figure 2.3). The uneven vertical pressure distribution creates a torque about the center of the wheel, opposite to ω. The distance e may be calculated from moment balance around the wheel axle:

$$e = z_t \frac{F_R}{F_N} \tag{2.6}$$

where F_R is the rolling resistance force, F_N the tire normal load and z_t the loaded tire radius. The rolling resistance coefficient, f_r, is defined as

$$f_r = \frac{F_R}{F_N} \tag{2.7}$$

By using Equation 2.6 in Equation 2.7, f_r can be expressed as

$$f_r = \frac{e}{z_t} \tag{2.8}$$

In the following another way to calculate the rolling resistance coefficient f_r will be defined, knowing the vertical pressure distribution. Secondary causes of rolling resistance are the fan effect of the rotating tire by the air outside ($2 - 4\%$ of the total rolling resistance force) and the slippage between tread and road ($\sim 5\%$).

Chapter 3

Existing tire models

The tire represents the only link between the vehicle and the ground, thus it is of extreme importance a good knowledge about its behaviour under different operating conditions. Great efforts have been done by the automotive industry in the field of tire modelling, thus an extensive bibliography is available. Figure 3.1 briefly describes different approaches used in tire modelling. Semi-empirical tire models, such as Magic Formula, that fit to tire test data were developed to represent tires in vehicle dynamic simulations. With the improvement of computational power, complex tire models were studied in order to predict the force and moment characteristics of the tire based on its physical features and construction. While the later are widely used for ride, comfort and durability purposes, the semi-empirical models are more common for dynamic handling simulations, since the computational efforts are smaller. In this chapter the two simplest tire models are briefly described: the *Magic Formula* and the Brush Model.

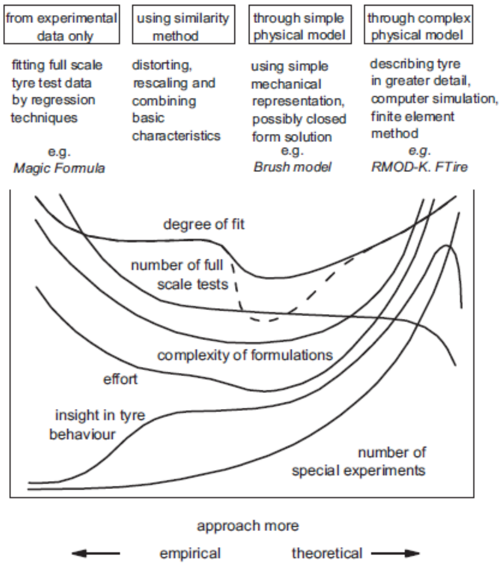
from experimental data only
using similarity method
through simple physical model
through complex physical model
fitting full scale tyre test data by regression techniques
distorting, rescaling and combining basic characteristics
using simple mechanical representation, possibly closed form solution
describing tyre in greater detail, computer simulation, finite element method
e.g. Magic Formula
e.g. Brush model
e.g. RMOD-K. FTire
degree of fit
number of full scale tests
complexity of formulations
effort
insight in tyre behaviour
number of special experiments
approach more
empirical
theoretical

Figure 3.1: Four categories of possible types of approach to develop a tire model [6]

3.1 Magic Formula model

The *Magic Formula* is a semi-empirical tire model developed by Hans B. Pacejka [6]. Semi-empirical means that the equations describing the force generation have no particular physical basis, but they can fit a wide variety of experimental data with good accuracy. Since there is no physical background, scaling factors have to be obtained from measurements.

The general form of the *Magic Formula* is [6]:

$$y = D \sin\big[C \arctan[(1-E)x + (E/B)\arctan(Bx)]\big] \tag{3.1}$$

where y represents the force (lateral or longitudinal) or the torque (self-aligning torque) and x is the slip quantity the force or torque depends on. B, C, D, E are factors that have a particular geometric meaning, in fact, referring to Figure 3.2:

- B is a stiffness factor;
- C is a shape factor;
- D is the peak value;
- E is a curvature factor;
- the product BCD is the slope of the curve at the origin;

The relation in Equation 3.1 can be used in case of ply-steer and conicity effects as well as wheel camber by adding new parameters, like a vertical or an horizontal offset:

$$Y(X) = y(x) + S_V, x = X + S_H$$

in this relation S_V and S_H represent the vertical and horizontal shift respectively. The values obtained are normalized to the vertical load acting on the wheel.

Approximation of the normal load dependence may be introduced as:

$$C = a_0 \tag{3.2}$$

$$D = a_1 F_z^2 + a_2 F_z \tag{3.3}$$

$$B = (a_3 F_z^2 + a_4 F_z)/(CDe^{a_5 F_z}) \tag{3.4}$$

$$E = a_6 F_z^2 + a_7 F_z + a_8 \tag{3.5}$$

The entire model is presented in [6]. The Magic Formula typically produces a curve that passes from the origin, reaches a maximum and subsequently tends to a horizontal asymptote, see Figure 3.2.

The aligning torque is obtained by multiplying the lateral force, calculated using 3.1, with the *pneumatic trail* t_p, plus the residual torque M_{zr}:

$$M_z = -t_p F_y + M_{zr} \tag{3.6}$$

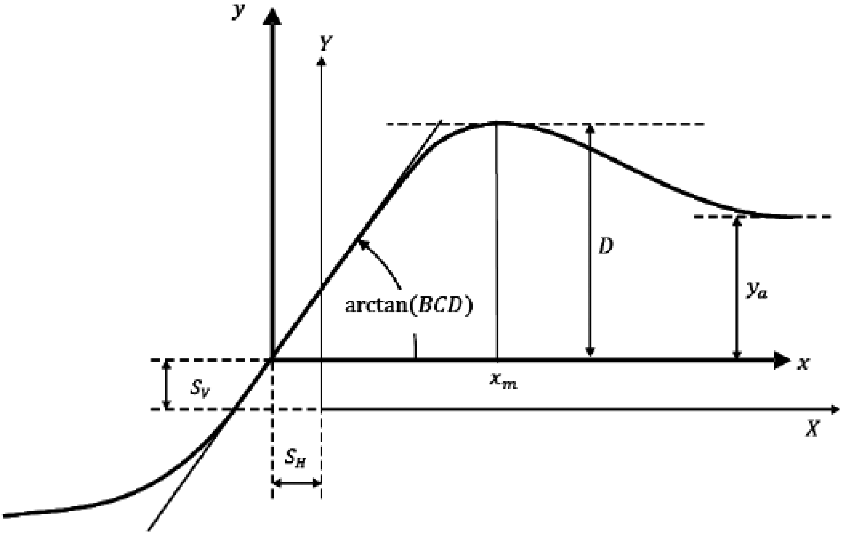

Figure 3.2: Magic Formula factors [7]

The pneumatic trail is the distance between the application point of the total lateral force and the Y_R axis. Its behaviour is described by another trigonometrical function:

$$t_p(\alpha_t) = D_t cos\big[C_t \arctan[B_t\alpha_t - E_t\big(B_t\alpha_t - arctan(B_t\alpha_t)\big)]\big] \tag{3.7}$$

where α_t is function of the slip angle plus an offset:

$$\alpha_t = \tan\alpha + S_{Ht} \tag{3.8}$$

In the same way the residual torque M_{zr} is described by a cosine relation:

$$M_{zr}(\alpha_r) = D_r \cos[\arctan(B_r\alpha_r)] \tag{3.9}$$

with:

$$\alpha_r = \tan\alpha + S_{Hf} \tag{3.10}$$

The cosine function allows the curve to have a peak shifted sideways, and to tend to an asymptote close to zero. As possible to see in Figure 3.3 the peak is shifted horizontally by a quantity equal to $-S_H$, D determines the magnitude of the peak value, as well as C determines the shape of the curve, influencing the asymptotic value y_a.

Some observations about this model have to be done. The Magic Formula model is limited to quasi steady-state conditions only, in case of pure cornering or braking or a combination of those two. It is a *global* method, i.e. it doesn't describe what happens in each point of the contact patch, but just the final result (force, torque). It has not a physical background, but it's just a very accurate way to fit experimental data. Moreover, it doesn't describe the energy dissipated inside the material and during the sliding conditions (for high slip velocity), as well it doesn't describe the behaviour of rolling resistance.

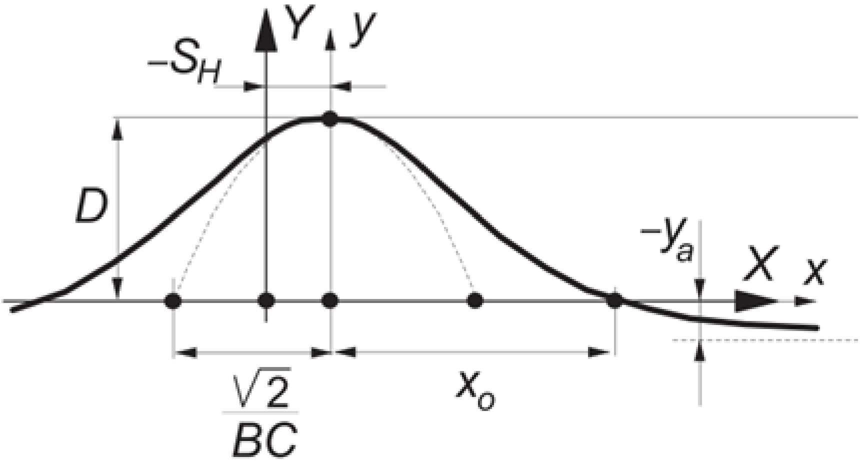

Figure 3.3: Aligning torque behaviour, Magic Formula [6]

In this work the Magic Formula represents the basis for comparison of the Multi-Line Brush model that is developed during this thesis, in order to validate it for steady-state handling issues.

3.2 Brush Tire model

The Brush Tire model is a very simplified way to model the creation of forces and torques between tire and road. A great number of works describes this approach, see e.g. [5, 8, 9], and it was quite popular in the 1960's and 1970's, before empirical approaches became the most used. In this section its basis are discussed.

The Brush Tire model describes the generation of forces in the contact patch considering the contact region formed by small volumes of rubber, acting as springs. Considering Figure 3.4, a system of coordinate axis is set in such a way that the origin is in the middle of the contact patch. Thus the x-axis is pointing forward, along the longitudinal direction of the wheel, and the y-axis is pointing laterally, as described in chapter 2. The contact patch is $2a$ long. On the top of the bristles a vertical pressure distribution is applied, and they are stretched longitudinally and laterally because of the slip velocity $\bar{v}_s$. This model is based on these assumptions:

- the normal load has a parabolic distribution along the contact patch, assuming zero value at the edges;
- the friction between the bristles and the ground is described by the simple Coulomb model:

  $$F_{x,y} = \mu F_z \quad \text{if} \quad F_{x,y} > \mu F_z \quad \text{(sliding condition)} \tag{3.11}$$

  where μ is the friction coefficient between bristles and road, F_x and F_y are the longitudinal and lateral force respectively generated by the

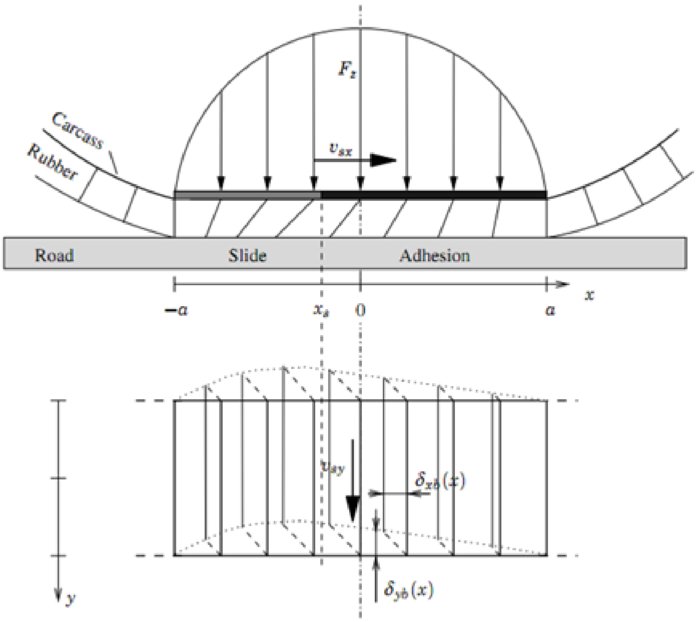

Figure 3.4: Brush tire model, deformation of the tire rubber (Top: side view; bottom: top view

stretching of the bristle, and F_z is the vertical load applied on that bristle. In this way it is possible to divide the contact patch into the adhesive and the sliding region;

- the carcass is considered as infinitely stiff;
- each bristle is assumed to deform independently in the longitudinal and lateral directions;

In the adhesive region the bristles adhere to the road surface and the deformation is allowed by the static friction. In the sliding region, instead, the forces produced are function of the sliding friction through Equation 3.11, thus the resulting force is independent of bristle deformation [10]. From Figure 3.4 it is possible to depict the deformation of the bristle δ_{xb} along the x-axis as well the deformation δ_{yb} along the y-axis. Considering a slip angle α, in the adhesion region the bristle is forced to follow a straight line with slope equal to $\tan\alpha$, from the leading edge $(a, 0)$ as long as no sliding occurs. Thus the lateral deformation δ_{yb} is function of the longitudinal coordinate x:

$$\delta_{yb} = (a - x)\tan\alpha \tag{3.12}$$

Consequently, assuming the lateral stiffness of the bristle equal to c_{py}, the lateral force per unit of length in the adhesion region for each bristle is:

$$F_{yb,a} = c_{py}\delta_{yb} \tag{3.13}$$

The sliding region occurs when the relation 3.11 is true, in this case when:

$$F_{yb,a} > \mu F_{zb} \tag{3.14}$$

where F_{zb} is the normal load applied on top of the bristle at the x coordinate. If Equation 3.14 is valid, then the lateral force will be equal to:

$$F_{yb,s} = \mu F_{zb} \tag{3.15}$$

The total lateral force will be equal to the sum of the forces generated by each bristle along the whole contact patch:

$$F_y = \int\limits_{-x_t}^{a} F_{yb,a} \mathrm{d}x + \int\limits_{-a}^{-x_t} F_{yb,s} \mathrm{d}x \tag{3.16}$$

as well the aligning torque M_z will be the algebraic sum of the aligning torques of each bristle around z-axis:

$$M_z = \int\limits_{-x_t}^{a} x F_{yb,a} \mathrm{d}x + \int\limits_{-a}^{-x_t} x F_{yb,s} \mathrm{d}x \tag{3.17}$$

where $-x_t$ is the longitudinal coordinate where sliding occurs. The bristles have similar behaviour in the longitudinal direction. For pure longitudinal slip, if v_x is the longitudinal wheel center speed, the coordinate for a bristle tip at the contact area front edge will after time Δt be:

$$x_l = a - v_x \Delta t \tag{3.18}$$

On the other hand the upper tip of the bristle, which moves with a velocity $R_e \omega$, will have the coordinate:

$$x_u = a - R_e \omega \Delta t \tag{3.19}$$

Consequently, using equation 2.5 the longitudinal bristle deformation will be:

$$\delta_{xb} = x_l - x_u = \kappa_x (v_x \Delta t) = \kappa_x (a - x) = -\kappa_x (x - a) \tag{3.20}$$

Introducing the longitudinal bristle stiffness c_{px} and dividing the region in adhesion and sliding part, as done before, it's possible to obtain the same result for the total longitudinal force:

$$F_x = \int\limits_{-x_t}^{a} F_{xb,a} \mathrm{d}x + \int\limits_{-a}^{-x_t} F_{xb,s} \mathrm{d}x \tag{3.21}$$

where $F_{xb,a} = c_{px} \delta_{xb}$ (adhesion region) and $F_{xb,s} = \mu F_{zb}$ (sliding region).

In this demonstration the friction coefficient μ is assumed to be equal for both lateral and longitudinal direction, and not function of the velocity of the wheel center v_x. These assumptions make the problem much more easier comparing to reality. In the same way the assumption on the symmetric normal load is not true, because in reality the application point of the normal load is not the origin $(0, 0)$, but it is a point shifted forward, as will be seen in chapter 5. Moreover, using just one line of bristles, it doesn't allow to have a 3D picture of all the forces acting in the contact patch, and this is a big drawback if the effects of camber angle have to be studied.

However, even with these assumptions, the brush tire model reaches to explain the nature of the forces in the contact patch with a strong physical background. Meanwhile it requires smaller number of model parameters for describing the steady-state characteristic.

3.3 Conclusion

In this chapter the two simplest tire models had briefly reviewed. They represent two different approaches to the modelling problem: the *Magic Formula* is an empirical model, that fits experimental data to some trigonometrical expressions. It has not a physical background and requires the determination of a great number of parameters. The Brush Tire model is a simple theoretical model, which can describe physically the nature of the force born in the contact patch. Due to its simplicity, it could give good results just for some simple situations.

In the next chapter, the *Brush Tire* model will be used as basis for the development of a Multi-Line Brush model, and a certain number of features will be added, to represent the reality as accurate as possible with a physical model, instead the *Magic Formula* will be used as reference.

Chapter 4

Rubber properties and modelling

In the previous chapter the Brush Tire model has been explained. It is a theoretical model useful to understand and simulate the generation of forces in the tire-road contact. However, the elements used to describe the rubber behaviour are just linear elastic springs, very simple to deal with but they don't represent real rubber behaviour. In this chapter the principal mechanical properties of rubber are presented, as well as the main models used in literature to describe its mechanical behaviour.

4.1 Mechanical properties

A tire is an advanced engineering product made of rubber and a series of synthetic components cooked together [11]. The materials of modern pneumatic tires are synthetic rubber, natural rubber, fabric, wire, carbon black and other chemical compounds. This mix produces a mechanical behaviour not easily predictable, that is function of a great number of parameters: amplitude and phase of the harmonic force applied, temperature, wear and so on. For the purpose of this work the response of this mix to harmonic excitations is of primary importance.

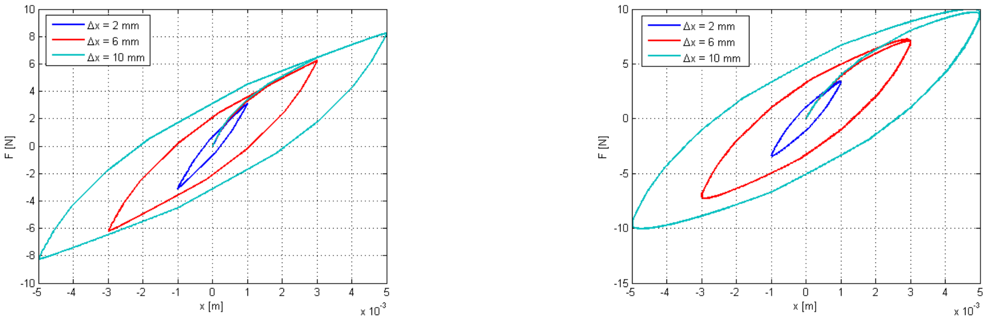

(a) **(b)**

Figure 4.1: Typical hysteresis loop of a harmonically excited rubber. Sinusoidal excitation with three different amplitudes. A lower frequency (1 Hz) has been set in 4.1a than in 4.1b (10 Hz)

The main characteristic of the rubber is its elasticity, which in most cases is non-linear. The response to a harmonic excitation of a rubber component is similar to that in Figure 4.1. The force (F) and displacement (x) graph shows a clear hysteresis loop. It means that the force needed to deform the material of a certain quantity x is greater than the force released by the material during the recovery phase, therefore a certain quantity of energy is dissipated inside the material itself. Since the force-displacement curves are not the same during the loading and unloading phase, they create a *loop*, and the area within the loop is the amount of dissipated energy (converted in thermal energy). The hysteresis is function of the amplitude and of the frequency: the dissipated energy increases with increasing frequency, this is due to viscous effects. There will always be hysteresis in the material, no matter how low the frequency is, because of friction effect inside the material. Thus it is possible to divide the characteristics of rubber into three different parts:

- Elastic part;
- Viscous part;
- Friction part;

How much each of these effects acts on the final mechanical behavior of the rubber is function of the compound of the rubber itself, as well as other parameters like temperature and geometry.

It is not easy to model precisely the rubber response to a given input, that is why some assumptions have to made, in order to simplify the problem.

4.2 Modelling of the rubber compound

As explained in the previous section, three different effects are simultaneously present in a rubber compound: elastic, viscous and friction effects. Thus the response of the rubber will be the sum of these effects:

$$F = F_e + F_v + F_f \tag{4.1}$$

where F_e is the elastic force, F_v is the viscous force and F_f is the friction force. A fundamental assumption needed to try to represent correctly the rubber behaviour is that these three effects are independent of each other. In reality this is not completely true, but is necessary for the establishment of a simple mathematical model. In the same way, the effects due to the temperature dependence are not taken into account, since they make the computational and modelling effort much bigger.

4.2.1 Visco-elastic force

The elastic and the viscous part represent the so called *viscoelastic* effect. Mathematically, the elastic part can be represented by a spring element, as well as the viscous effect can be represented by a dash-pot element. Many

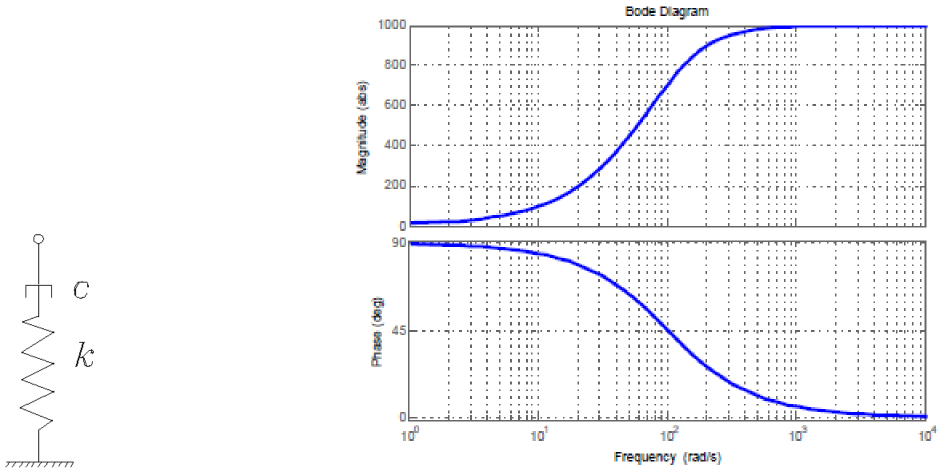

(a) **(b)**

Figure 4.2: Maxwell visco-elastic model. Frequency analysis (Bode diagram), $k = 1000$ N/m, $c = 10$ Ns/m

efforts have been made in the literature to present a model, that is a combination of springs and dash-pot elements, that can represent and simulate the rubber behavior. Some of them are presented below.

The Maxwell model

The Maxwell model [12] is presented as a spring element (with elastic constant k) connected in series with a dash-pot element (c). The stress σ and the strain ε are function of time through the relation:

$$\frac{\dot{\sigma}(t)}{k} + \frac{\sigma(t)}{c} = \dot{\varepsilon}(t) \tag{4.2}$$

This model is usually applied to the case of small deformations. If a sudden deformation ε_0 is applied and held on, the stress decays from the inital value $k\varepsilon_0$ to zero with a characteristic time of c/k. In Figure 4.2 the frequency analysis of a Maxwell element is shown. For low frequency the amplitude of the response is neglictable, this does not represent the reality, as well as the loss factor ϕ is null for high frequencies.

Kelvin-Voigt model

The Kelvin-Voigt model [13] represents the viscous and elastic effect with a spring element connected in parallel with a dash-pot element, as can be seen in Figure 4.3. The stress σ and the strain ε are governed by the law 4.3:

$$\sigma(t) = k\varepsilon(t) + c\dot{\varepsilon}(t) \tag{4.3}$$

Acccording to [14] the Kelvin-Voigt model doesn't represent dynamic stiffness and damping very good when optimized over a large frequency range. In fact, for high frequencies, the dynamic stiffness becomes too high, because of the dash-pot element. This does not allow to model the real case.

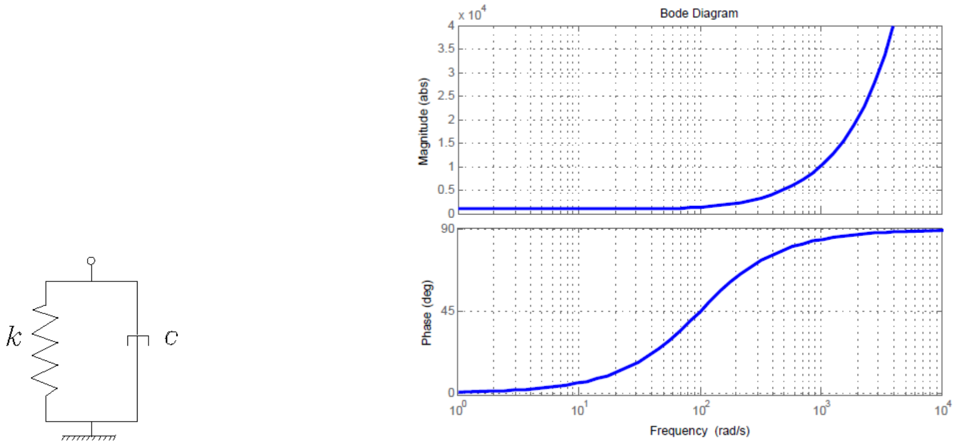

(a) (b)

Figure 4.3: Kelvin-Voigt visco-elastic model. Frequency analysis (Bode diagram), $k = 1000$ N/m, $c = 10$ Ns/m

Standard Linear Solid (SLS) model

The Standard Linear Solid model, also known as *Zener* model [12], is formed by a spring connected in parallel with a Maxwell element (dashpot plus spring). It is also called the *Three Parameters Maxwell* model, where the three parameters are the elastic stiffnesses of the springs and the damping of the dash-pot element. A representation is shown in Figure 4.4. From the Bode diagram of the same figure it is possible to notice that the dynamic stiffness is limited both for low frequency and high frequency. For low values of excitation frequency the dynamic stiffness has a value next to the elastic stiffness of the spring 1, because of the dash-pot element, which nullify the effect of the spring 2. On the other hand, for high values of frequency, the dash-pot element acts as a rigid connection, and the dynamic stiffness becames the sum of the elastic stiffness of the two springs. Moreover, it's of fundamental importance for the dynamic of the Multi-Line Brush model to notice the peak in the loss factor ϕ, for frequencies around k_2/c.

The three parameter Maxwell model follows the relation 4.4.

$$\dot{\sigma}(t) = -\frac{k_2}{c}\sigma(t) + \frac{k_1 k_2}{c}\varepsilon(t) + (k_1 + k_2)\dot{\varepsilon} \tag{4.4}$$

There is no easy analitical solution to equation 4.4, thus it is solved numerically.

Generalized Maxwell model

The Generalized Maxwell model [12], also known as Maxwell-Wiechert model, it is the most general form of linear model for viscoelasticity. Here a spring element is connected in parallel with i Maxwell elements (see Figure 4.5). It is a more general case of the Three Parameter Maxwell model: in fact for $i = 1$ the generalized Maxwell model becomes the Three Parameter Maxwell

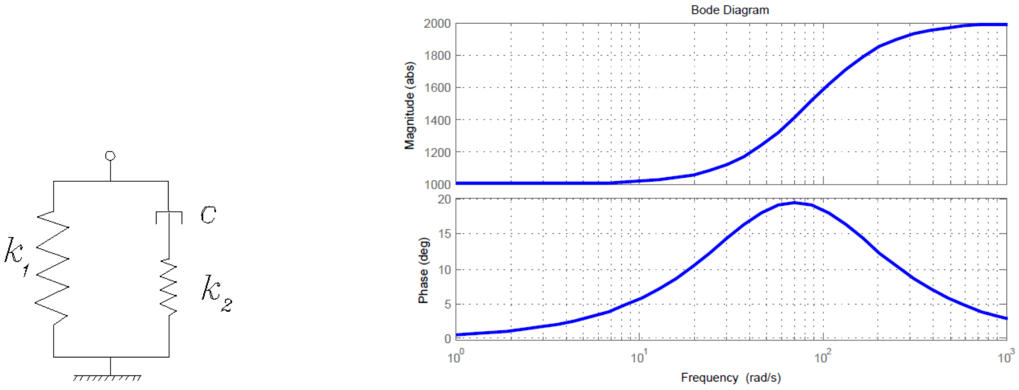

(a) **(b)**

Figure 4.4: Three parameter maxwell visco elastic model. Frequency analysis (Bode diagram), $k_1 = 1000$ N/m, $k_2 = 1000$ N/m, $c = 10$ Ns/m

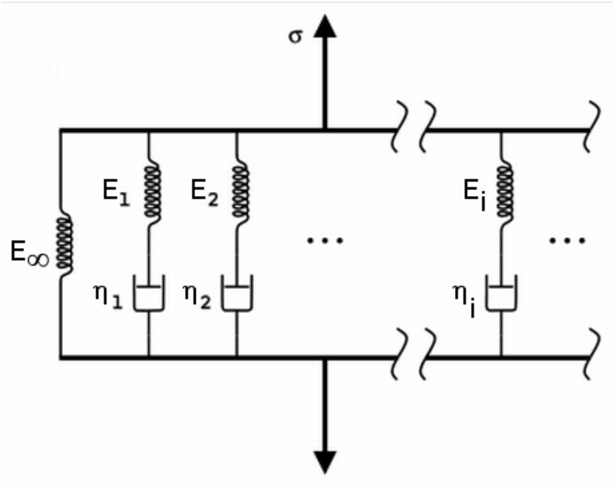

Figure 4.5: Scheme of the generalized Maxwell model

model. Using different Maxwell elements it can take into account the relaxation which doesn't occur at a single time, but in a sets of time. However it's more complex to deal with, since the number of parameters increases notably.

From previous attempts of modelling the rubber behavior in a rolling tire [15] the Three Parameters Maxwell model has been chosen as the one which can simulate more realistically the visco-elastic forces, thus it will be used in the next chapters to model the visco-elastic effects of the rubber in the Multi-Line Brush model.

4.2.2 Friction force

As said previously, the tire is made of a compound of materials, first of all rubber (natural or synthetic) cooked together with carbon black, silica, fabric, steel, nylon and other elements. The synthetic rubber used to manufacture tires is made by the polymerization of a great variety of petroleum-based monomers. During the polymerization, monomers form long chains of polymers which, during their deformation, dissipate energy, because of the inner friction caused by the stretching of these chains. This inner friction allows the generation of the *hysteresis loop* in the force-deformation diagram (see Figure 4.1) and represent the rate independent energy dissipation.

Different models try to simulate friction, in different ways. Here the Masing model and the Berg model [16] are briefly examinated.

The Masing model

The Masing model describes the friction effect using Coulomb friction elements. It is a discrete model, i.e. it uses a finite number (n) of Jenkin elements connected in parallel (Figure 4.6). The Jenkin elements are composed by a spring element (with elastic constant k_i) in series with a Coulomb friction element with the adhesive force R_i.

The total friction force caused by a $x(t)$ displacement is described by:

$$F_f(x) = \sum_{i=1}^{n} F_i(x(t)) \tag{4.5}$$

where F_i is the force of the i:th Jenkin element. Since there is a Coulomb friction element, the force F_i can assume two values, the first relation in Equation 4.6 is valid if the Coulomb element is sticking, the second one if it is not:

$$\dot{F_i} = \begin{cases} k_i \dot{x} & |F_i| < R_i \text{ or } (|F_i| = R_i \text{ and } sign(\dot{x}F_i)) \leq 0 \\ 0 & \text{else} \end{cases} \tag{4.6}$$

Since in equation 4.6 the function *sign* is used, it is not a linear function, thus some problems could arise when it is implemented in the Matlab code. In the Appendix it is reported how the Equation 4.6 is implemented. This non linearity obligate us to use a fixed-step integration/derivation in time, increasing the computational effort.

Figure 4.7 shows an example of a Masing friction model with five Jenkin elements. From the figure the Payne effect is captured. The Payne effect describes the reduction of stiffness (defined as the ratio of the maximum Force achieved to maximum deflection) with increasing amplitude, typical of rubber elements. This graph has been obtained with a fixed-step integration in time.

The Berg model

Berg [16] models the friction of rubber bushings using two parameters, x_2 and $F_{f,max}$, and two reference states, x_s and F_s, that are the displacement and the force at the turning poing respectively. More about this model can

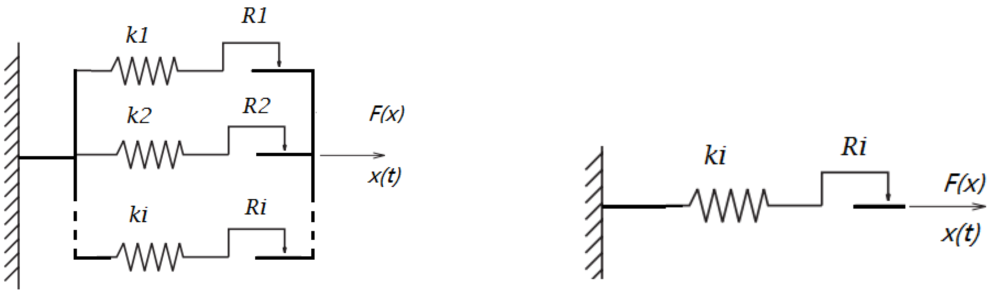

(a) Masing model **(b)** Jenkin element

Figure 4.6: Discrete masing model

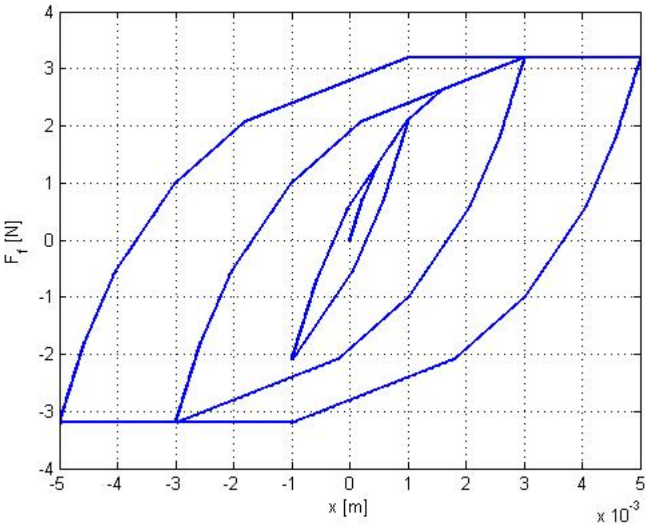

Figure 4.7: Force displacement loop of Masing friction model with five Jenkin elements.

be found in [14] and in [16]. The friction force F_f in the Berg model is described as:

$$F_f = F_{fs} \quad \text{if } x = x_s \tag{4.7}$$

$$F_f = F_{fs} + \frac{x - x_s}{x_2(1-\alpha) + (x - x_s)}(F_{f,max} - F_{fs}) \quad \text{if } x > x_s \tag{4.8}$$

$$F_f = F_{fs} + \frac{x - x_s}{x_2(1+\alpha) - (x - x_s)}(F_{f,max} + F_{fs}) \quad \text{if } x < x_s \tag{4.9}$$

where

$$\alpha = \frac{F_{fs}}{F_{f,max}} \tag{4.10}$$

x_2 is the displacement needed to create the friction force $F_f = F_{f,max}/2$ from the state $(x_s, F_{fs}) = (0, 0)$. $F_{f,max}$ is the maximum friction force that can be developed and x_2 controls how fast this force is developed in relation to

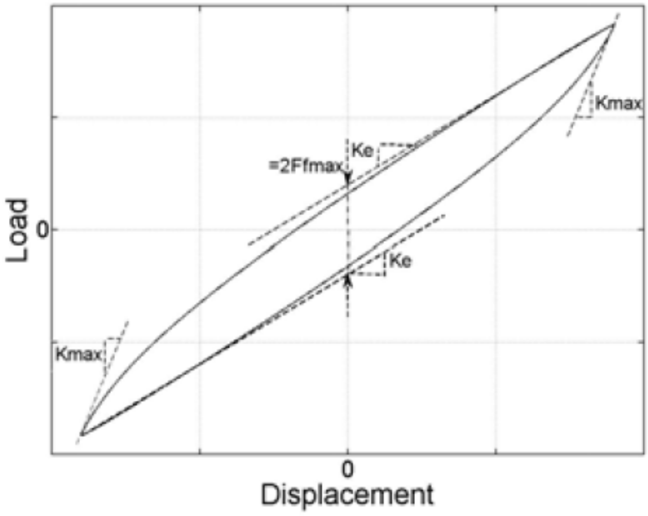

Figure 4.8: Berg model, [16]

displacement. The Figure 4.8 shows how a Berg friction curve looks like. When this function is excited at constant amplitude, after some cycles of transient response it reaches a steady state. The parameterizations of the Berg friction model is made from experimental data at low frequency, since the viscous force can be neglected then. In [14] a comparison between these friction models is discussed. In [15] the author uses and compares both the Masing and the Berg model, in order to establish which one is the best to represent the internal friction forces for a turning wheel. The main result is that the Berg model doesn't manage to converge to a stable value, but it oscillates. That's why the Masing model will be used in the next chapter to simulate the friction forces of a tire.

4.3 Rubber model used in this work

The final model chosen for describing the rubber behaviour in the Multi-line brush model is composed by a three parameters Maxwell element in parallel with a five elements Masing model (figure 4.9). From now on this model will be called *rubber element*, to simplify the notation along the work.

Thus the law that governs the *rubber element* is:

$$F = F_{ve} + F_f \tag{4.11}$$

where F_{ve} is the force of the Three Parameters Maxwell visco-elastic model:

$$\dot{F}_{ve}(\delta, t) = -\frac{k_2}{c} F_{ve}(t) + \frac{k_1 k_2}{c}\delta(t) + (k_1 + k_2)\dot{\delta} \tag{4.12}$$

and F_f is the friction force of the Masing model:

$$F_f(\delta) = \sum_{i=1}^{n} F_i(\delta(t)) \tag{4.13}$$

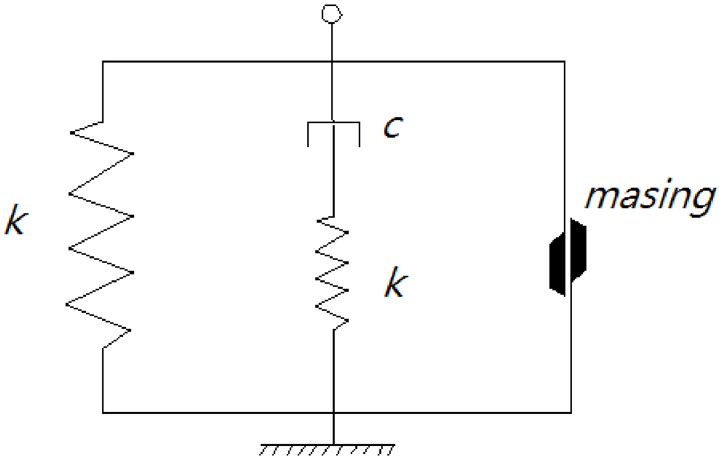

Figure 4.9: *Rubber element*, on the left the visco-elastic part is represented by a Three Parameters Maxwell model, on the right the friction part is represented by the five elements Masing model

with F_i are defined by Equation 4.6. δ represents the deflection of the rubber element, and it can be along the X_R, Y_R or Z_R axis. Since this is the first approach to study the rolling tire dynamics with rubber modelling properties, the elastic stiffnesses of the springs in the visco-elastic model have the same values, in order to simplify the problem.

An example of the response of the *rubber element* to a sinusoidal displacement input is shown in Figure 4.10. As can be seen for increasing values of frequency the hysteresis loop becames bigger, it means a bigger quantity of energy is dissipated throught the viscous and the friction part. The energy dissipated dependance on the frequency is due to the viscous part, according to Figure 4.4 (b), in particular the loss factor increases with the frequency until it reaches the peak. After that, the energy dissipated, i.e. the area hemmed-in by the force-displacement curve, starts to decrease.

The presented *rubber element* will be used to construct the brush model, and it will be used in place of the elastic springs of the original Brush model.

4.4 Conclusion

In this section the mechanical properties of rubber materials have been discussed. The response of the material to a displacement is a force made by three components: elastic, viscous and friction part. The first one is the most evident characteristic of a rubber material, and in this work it will be represented by a linear elastic element (spring), even if in reality the behaviour is more similar to a cubic curve. The viscous part represents the rate dependent response, the energy dissipated by viscous forces is function of the frequency of excitation of the rubber element. The latter one, the friction part, represents the rate-independent energy dissipation, it is not

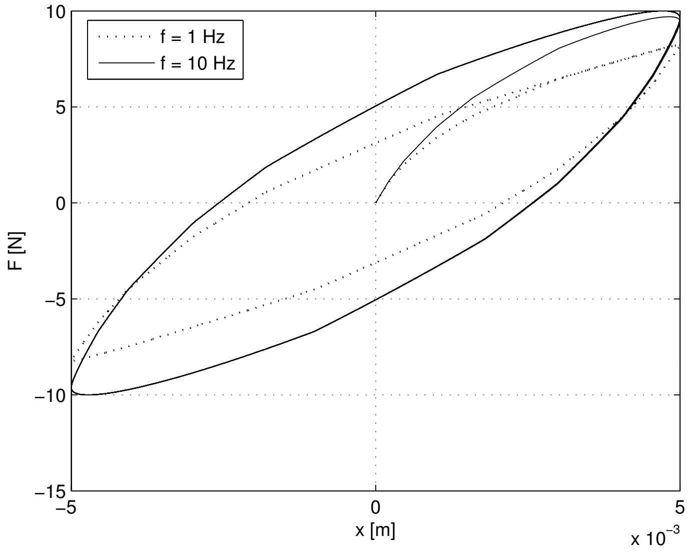

Figure 4.10: Dynamic response of the rubber element for two sinusoidal inputs

function of the frequency and it is represented by a five elements Masing model. The three components of the force response are gathered together into a *rubber element* model.

The *rubber element* model is the fundamental component of the Multi-Line Brush model, developed in the next chapter.

Chapter 5

Development of a Multi-Line Brush Tire model

In this chapter a 3D Multi-Line Brush tire model is developed, according to the Brush tire theory. The model takes as input the side slip angle α, the longitudinal slip κ_x, the camber angle γ, the longitudinal velocity of the wheel v_x and the normal load acting on the wheel F_z. It gives as output the longitudinal and lateral forces (F_x and F_y), the overturning, rolling resistance and aligning torques (M_x, M_y and M_z), as well as the rolling resistance factor and the distribution of energy dissipated.

5.1 Introduction

The tire is modelled as it is formed by l longitudinal lines, and each line contains n *bristle* elements, as can be seen in Figure 5.1. Each *bristle*[1] element is composed by three *rubber elements*, one for each direction X_R, Y_R and Z_R, which behave independently for each direction. Each *rubber element* can't create torque, but torques on the wheel are created by the different distribution of the forces of each *bristle* along the contact patch. The sum of the forces created by each *bristle* gives the total force for the direction considered. The coordinate system used is explained in Chapter 2. The longitudinal velocity v_x will always be considered positive, but the model is valid also for negative values.

5.2 Geometry

For the construction of the geometry of the tire let's consider the code of a real tire. An example of ISO code of a tire could be:

$$\underbrace{225}_{B}/\underbrace{45}_{s_r}\quad\underbrace{R17}_{2R_r} \tag{5.1}$$

---

[1] "Bristle" here has not the meaning of *spring*, but it is the elementary part of the tire model.

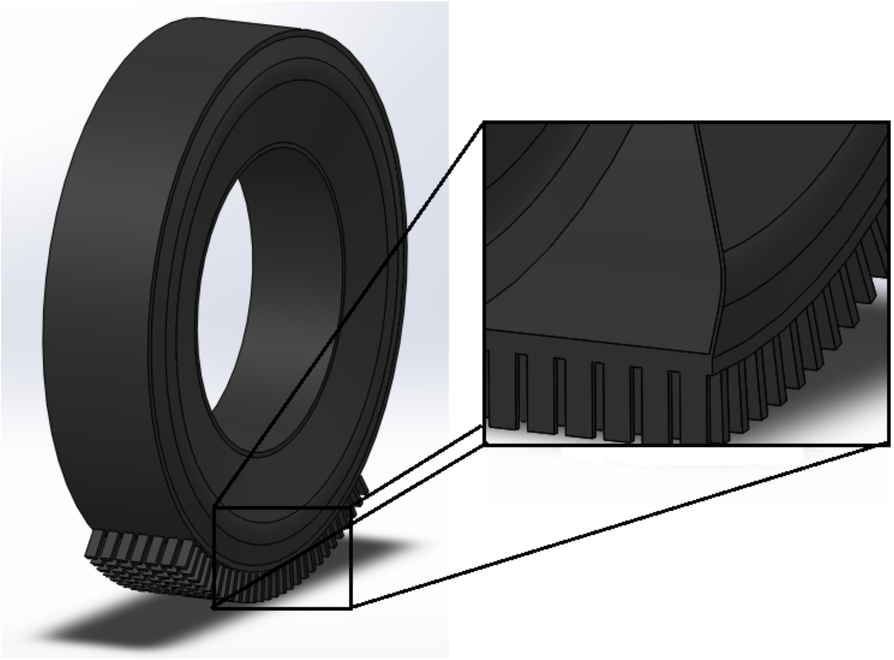

Figure 5.1: Representation of the model with 7 lines

where B is the cross-section width of the tire (in mm), s_r is the percentage ratio of B to the side-wall height s_w, R_r is the tire rim radius (in inches). Other parameters are w_r that is the width of the tire rim and α_0, that is the angle between the side-wall and the axis Z_W. In figure 5.2a the shape of the wheel is schematically shown. In this case the lateral angle is $\alpha_0 = 5\,\text{deg}$. The tread is modelled as a very flat parabola, in order to simulate the real vertical load distribution. The peak of the parabola is 2 mm deeper than the height of the side-wall s_w. In Figure 5.2c the tread shape is shown in blue, where R_{mean} is the mean tread radius on the (Y_W, Z_W) plane (see Section 5.4).

From Figure 5.2b each element of the tread has been parametrized to the wheel axis system (X_w, Y_w), in such a way to have a $R_w(i,k)$ coordinate, which stands for the distance of the point considered from the Y_w axis (considered positive if it stands in the negative Z_w plane, in order to avoid negative values), and a $b(i,k)$ coordinate, which is the distance of the point from the Z_w axis. i is the index for each bristle in the line, k is the index of each line. From their definition it's important to notice that R_w and b don't depend on the camber angle γ, since they are defined in the wheel axis system. Moreover, since the wheel is axis-symmetric, the radius of the bristles R_w varies only along the Y_w direction, thus:

$$R_w(i,k) = R_w(k) \tag{5.2}$$

In the same way also the distance $b(i,k)$ is function only of the line considered, thus:

$$b(i,k) = b(k) \tag{5.3}$$

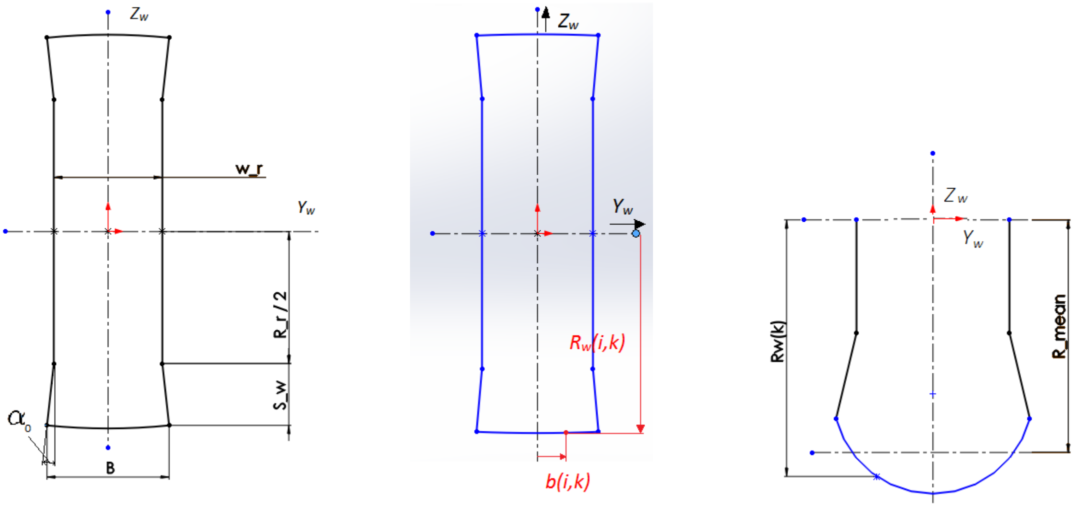

(a) (b) (c)

Figure 5.2: Front view of the wheel

The Equation 5.3 is not true in the real case, because the cross sections of the tread can move laterally. However, since in this model there are not elements that link the bristles to each other (it is not a finite element model), the Equation 5.3 is necessary. From Figure 5.3, on each line a segment angle θ' is introduced, to enclose the whole area of interest. The segment angle is equally divided in $n-1$ parts, so the vector of angular coordinate can be constructed as:

$$\bar{\varphi} = (\varphi_1, \varphi_2, \ldots, \varphi_n) \tag{5.4}$$

in such a way that:

$$\varphi_i - \varphi_{i-1} = \theta'/(n-1) \tag{5.5}$$

where n is the number of bristles on each line. Obviously the segment angle is bigger than the angle formed by the bristles in contact with the ground. A value of $\theta' = 90$ is big enough for normal conditions. φ_i represents the angular coordinate of each bristle. The vector $\bar{\varphi}$ is not function of the line considered, since each line has the same number of bristles in the same angular position. Thus a simple vector is enough to describe all the angular position of all the lines.

5.3 Outline of the code

In order to calculate the forces and the deflections acting on the tire bristles a precise order in the different phases of the code is followed, and it is showed in Figure 5.4. Setting the initial vertical coordinate of the wheel center equal to the unloaded wheel radius, the vertical deflection of each bristle is calculated first. Thus, from the rubber model, the vertical force developed by each bristle is calculated, and, from its sign, it is possible to establish which bristles are in contact with the road. Those bristles can

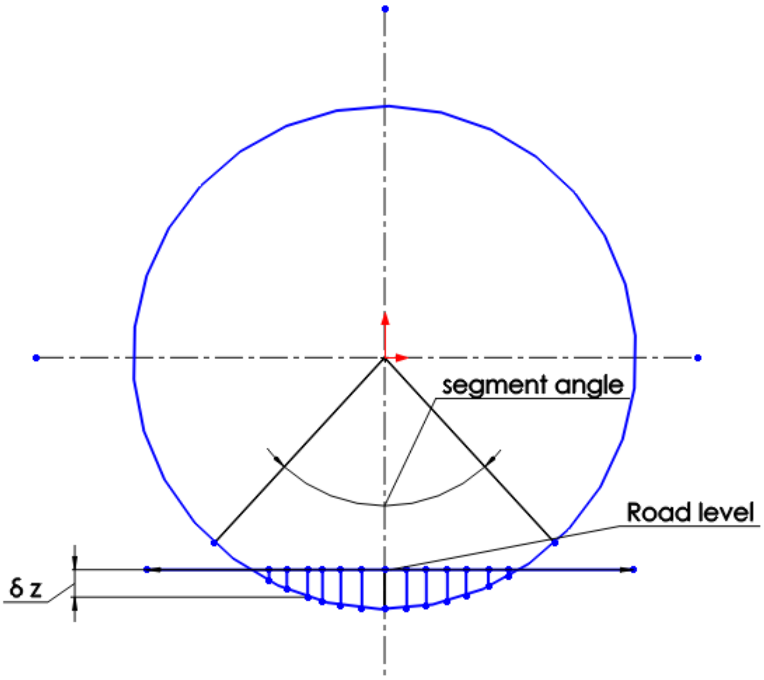
segment angle
Road level
δ z

Figure 5.3: Side view of the wheel

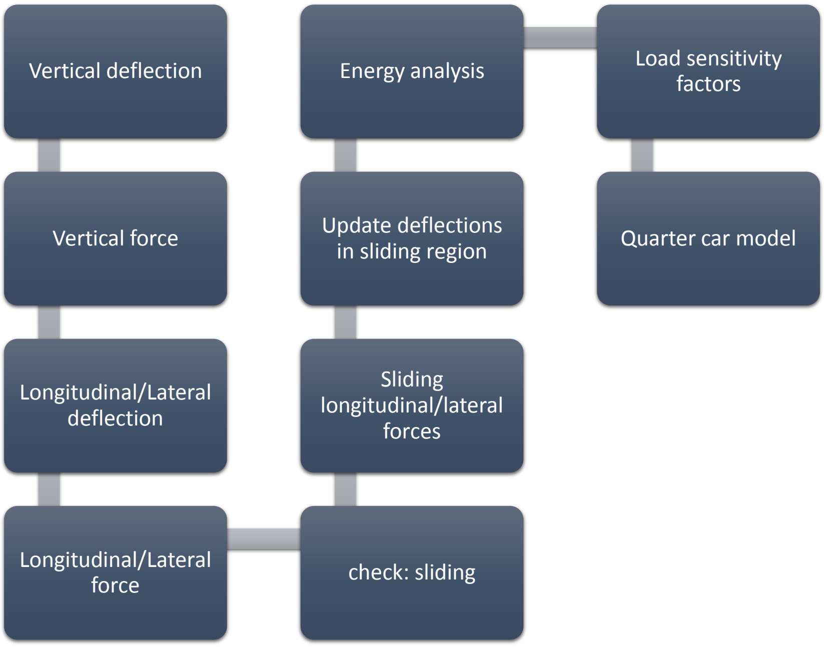
Vertical deflection
Vertical force
Longitudinal/Lateral deflection
Longitudinal/Lateral force
check: sliding
Sliding longitudinal/lateral forces
Update deflections in sliding region
Energy analysis
Load sensitivity factors
Quarter car model

Figure 5.4: Phases order in the Multi-Line Matlab code for each *dt* interval time

generate a longitudinal and lateral force, that can be calculated from the lateral and longitudinal deflection. Then, if the force generated (combination of longitudinal and lateral) is bigger than the friction limit of the bristles with the ground, the same force is limited to the friction limit, losing in this way the information about the longitudinal and lateral deflections of bristles. Thus they are calculated again in an approximated way, later explained. At this point, the forces and the deflections in all the directions are known, thus it's possible to analyse the energy and power dissipated, both by internal friction and by sliding. After that, the total forces (sum of the forces of each bristle) are updated with the load sensitive factors. The total forces and moments are then used in the quarter car model to find out the new vertical position of the wheel center, and all the cycle starts again.

Each cycle analyses a finite time interval *dt*, and it is repeated until a certain final time is reached, around 2 seconds.

5.4 Dynamics

As the tire starts to roll, the angular position of all the bristles change, and it is updated in this way:

$$\bar{\varphi} = \bar{\varphi} - \omega \cdot dt \tag{5.6}$$

where *dt* is the time step considered, and ω is calculated as:

$$\omega = (1 + \kappa_x)\frac{v_x}{R_{mean}} \tag{5.7}$$

In the Equation 5.7 R_{mean} is the mean radius of the wheel, i.e. the mean of the vector R_w. The R_{mean} is used instead of R_e because the effective rolling radius is not so easy to calculate. This means that a longitudinal force F_x will occur only if $\kappa_x \neq 0$. It is possible that the bristle φ_i moves out from the segment-angle θ', if this happens, then the angular coordinate of that element will be modified as:

$$\varphi_i = \varphi_i - \theta' \quad \text{if } \varphi_i > \theta'/2 \tag{5.8}$$

$$\varphi_i = \varphi_i + \theta' \quad \text{if } \varphi_i < -\theta'/2 \tag{5.9}$$

Knowing the angular position it is possible to calculate the deflection δ along the three axis X_R, Y_R and Z_R (the contact between the ground and the tire happens on the road plane, that is why the deflection are calculated on the *road* axis system). Introducing the time j, the deformation along the vertical axis δ_z will be:

$$\delta_z = -z_t(j) + R_w(k) \cdot cos(\bar{\varphi}) \cdot cos(\gamma) - b(k) \cdot sin(\gamma) \tag{5.10}$$

where δ_z is the matrix of the vertical deflections. It has l rows (number of bristle lines) and n columns (number of bristles for each line). z_t is the vertical coordinate of the wheel center in the *road* axis system, it means that in steady state condition z_t is equal to the radius of the loaded wheel (positive). Its value is updated by the quarter car model. The value of the deflection along the Z_R axis is used to calculate the vertical force acting on each bristle: if the deflection is positive it means that the bristle is *compressed* between the rim and the road, if negative it means that the bristle is not in contact with the road. Thus the following control is set:

$$\delta_z = 0 \quad \text{if } \delta_z \leq 0 \tag{5.11}$$

In order to calculate the vertical force on each bristle the Equations on the *rubber element* are used, in particular the Equation 4.11, from which it is possible to establish:

$$f_z = f_{rubber}(\delta_z) \tag{5.12}$$

In the Equation 5.12 f_z is the matrix of the vertical forces applied to the bristles, and it assumes positive values if the force is applied from the ground to the bristle (positive according to Z_R axis), i.e. the bristle is compressed. It has the same size of the matrix δ_z, l rows and n columns. Since the dynamics of the problem is not linear (as a simple spring of the traditional brush model), for some bristles of the contact patch the resulting force f_z could be negative, meaning that the road is "pulling" the bristle down. Obviously this phenomenon couldn't happen in reality, that's why in code the sequent control is needed:

$$f_z = 0 \quad \text{if } f_z < 0 \tag{5.13}$$

Thus

$$in\_contact = \begin{cases} 1 & \text{if } f_z = 0 \\ 0 & \text{if } f_z > 0 \end{cases} \tag{5.14}$$

For the vertical direction it is possible to calculate directly the value of the deflection. For the longitudinal and lateral direction, however, this is not possible, but the deflection $\delta_{x,y}$ will be the integration of the time-step deformation dx and dy in time:

$$\delta_{a,x} = \delta_{a,x} + dx \tag{5.15a}$$

$$\delta_{a,y} = \delta_{a,y} + dy \tag{5.15b}$$

where $\delta_{a,x}$ and $\delta_{a,y}$ are the longitudinal and lateral deflections respectively in the adhesion region. When the bristle is entering the contact patch, its deflections $\delta_{a,x}$ and $\delta_{a,y}$ are null. In order to calculate the deflection after entering the contact patch, the tip of the bristle is assumed as stick to the ground (that moves with a speed v_x), instead the top of the bristle,, fixed to the carcass, has a speed equal to $w \cdot R_{mean}$. The longitudinal and lateral increment dx and dy of the bristles are respectively:

$$dx = v_{\delta_{a,x}} \cdot dt \tag{5.16a}$$

$$dy = v_{\delta_{a,y}} \cdot dt \tag{5.16b}$$

where $v_{\delta_{a,x}}$ and $v_{\delta_{a,y}}$ are respectively the longitudinal and lateral deformation velocity of the bristles in the adhesion region. Since the tip of the bristle adheres to the road, the deformation velocity of the bristles in the adhesion region are equal to the slip velocity $v_{s,x}$ and $v_{s,y}$, i.e. the difference of the road velocity and the wheel circumferential speed:

$$v_{\delta_{a,x}} = v_{s,x} \tag{5.17a}$$

$$v_{\delta_{a,y}} = v_{s,y} \tag{5.17b}$$

where:

$$v_{s,x} = \omega \cdot R_{mean} - v_x \cdot - \dot{\Psi} \cdot b(k) \tag{5.18a}$$

$$v_{s,y} = - \omega \cdot R_{mean} \cdot sin(\bar{\varphi}) \cdot sin(\gamma) - v_y - R_w \cdot \sin(\bar{\varphi}) \cdot \dot{\Psi} \tag{5.18b}$$

where $\dot{\Psi}$ is the yaw rate (considered equal to 0 if not specified). In the Equation 5.18a the speed of deformation of the bristle $v_{\delta_{a,x}}$ is not function of the radial coordinate $R_w(k)$, this means that the longitudinal force is symmetric about the X_R axis, whatever the camber angle γ is.

The deflections $\delta_{a,x}$, $\delta_{a,y}$, and the deformation speeds $v_{\delta_{a,x}}$ and $v_{\delta_{a,y}}$, are set to 0 if the bristles are not in contact with the ground. This operation is done because the bristles considered are only the ones of the segment angle θ', so it is impossible to study the free dynamics of part of the wheel that are not in contact with the road.

From the Equations 5.15 the force matrices $f_{a,x}$ and $f_{a,y}$ in the adhesion region are calculated using the *rubber element* equation 4.11:

$$f_{a,x} = f_{rubber}(\delta_{a,x}) \tag{5.19a}$$

$$f_{a,y} = f_{rubber}(\delta_{a,y}) \tag{5.19b}$$

The values of the forces are correct only in the adhesion region. For this reason the case where the bristle starts to slide has to be discussed.

5.5 Sliding region

When longitudinal slip or lateral slip occurs, the deflection $\delta_{x,y}$ increases from the leading edge to the trailing edge. In the same way the forces $f_{x,y}$ increase as well, until they became so high that overcome the friction limit with the road.

The friction between road and tread is not easy to model, it is function of the rubber compound, the pattern of the tread as well as the road, the relative velocity of the surfaces. In the original brush model the friction is modelled with just two parameters, the static friction and the dynamic friction. When the resultant force on the (X_R, Y_R) plane is greater than the product between the static friction and the vertical force acting on the bristle, the resultant force is limited itself by the dynamic friction. A focus on the friction in the Brush Tire model can be found in [10], and a deeper focus on the friction effect and modelling can be found in [17], [18] and [19].

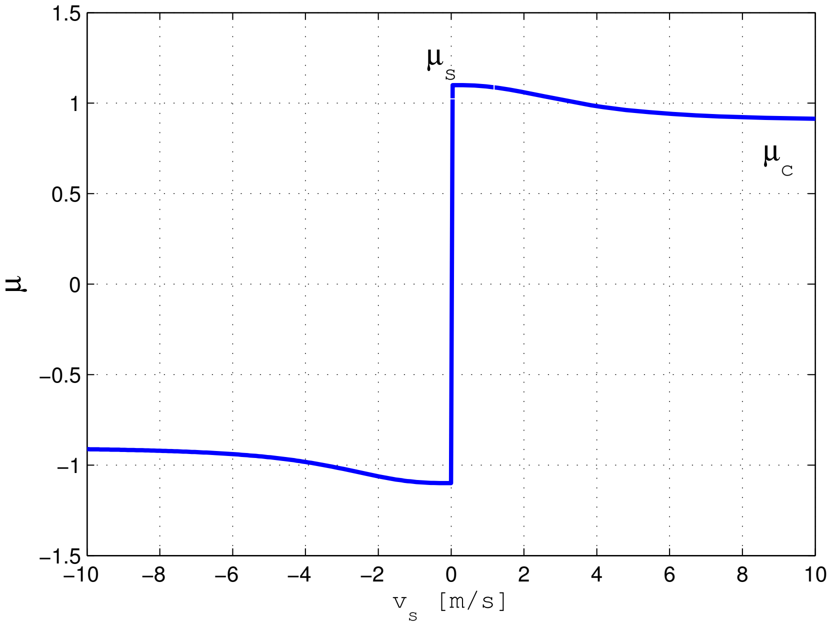

Figure 5.5: Dynamic friction model, $\mu_s = 1.1$, $\mu_c = 0.9$, $v_{str} = 3.5$ m/s

In this work a $friction function$ is used. It depends on the sliding velocity between the tread and the road with a function described in Equation 5.20 for both longitudinal and lateral direction:

$$\mu_x(v_{slid,x}) = \mu_{c,x} + \frac{\mu_{s,x} - \mu_{c,x}}{1 + |v_{slid,x}/v_{str,x}|^{2.5}} \tag{5.20a}$$

$$\mu_y(v_{slid,y}) = \mu_{c,y} + \frac{\mu_{s,y} - \mu_{c,y}}{1 + |v_{slid,y}/v_{str,y}|^{2.5}} \tag{5.20b}$$

where $v_{slid,x}$ and $v_{slid,y}$ are the sliding velocity of the surfaces in contact. μ_s is the value of the friction when the sliding velocity is null, i.e. the static friction. μ_c is the value of the friction at the asymptote and v_{str} is the Stribeck velocity. In Figure 5.5 it is shown an example of dynamic friction function.

The dynamic friction is function of the sliding velocity between the surfaces, in the case of rolling tire the two surfaces are the tread and the road, i.e. the tip of the bristle and the road. However, implementing the sliding velocity in the code results in numerical problems, such as stability and convergence. For this reason the deformation velocity will be used, instead of the actual sliding velocity. The difference in the resulting forces is very small, since the difference in the friction coefficient μ is small. In the following chapter the difference will be showed.

$$v_{slid} \approx v_\delta \tag{5.21}$$

The friction coefficient in the Equation 5.20 is different between the two directions (lateral and longitudinal) because in most part of real cases the friction is anisotropic. In [10] the author deals with different methods of considering an anisotropic friction. The individual bristle starts to slide when the relation 5.22 is valid:

$$\frac{f_x^2}{(\mu_{s,x} f_z)^2} + \frac{f_y^2}{(\mu_{s,y} f_z)^2} > 1 \tag{5.22}$$

which is the equation of the friction ellipse, described in [10]. If the condition in Equation 5.22 is valid, then the forces (lateral and longitudinal) can't be calculated using Equation 5.19, but it will be a function of the friction coefficient μ and of the vertical load F_z:

$$f_{s,x} = \frac{\mu_x^2 v_{slid,x}}{(\mu_x v_{slid,x})^2 + (\mu_y v_{slid,y})^2} f_z \tag{5.23a}$$

$$f_{s,y} = \frac{\mu_y^2 v_{slid,y}}{(\mu_x v_{slid,x})^2 + (\mu_y v_{slid,y})^2} f_z \tag{5.23b}$$

where μ_x and μ_y are those obtained with the Equations 5.20. Equation 5.23 represents the distribution of the total force (limited by friction) in the X_R, Y_R plane between the longitudinal and lateral direction. In this case the Maximum Dissipation Rate principle is used. The theory is presented in [20], and it asserts that the total friction force is generated in such a way that the mechanical work $W = -\bar{v}_s \cdot \bar{F}_s$ is maximized under the constraint:

$$\left(\frac{f_{s,x}}{f_z \mu_x}\right)^2 + \left(\frac{f_{s,y}}{f_z \mu_y}\right)^2 \leq 1 \tag{5.24}$$

This results in the Equations 5.23. According to literature this is the most correct way to deal with anisotropic friction.

Figure 5.6 shows the difference in the slip-force diagram between a constant friction coefficient and a dynamic friction model.

However, applying the equation 5.23 for the calculation of the forces in the sliding region, the relation on the displacement of the bristles, Equation 5.15, loses its validation, as well as the knowledge about the visco-elastic and friction forces. In order to evaluate the new internal friction force in the rubber element, the evaluation of the actual deformation in the sliding region is needed. Since the relation in Equation 5.19 is not linear, it is not so easy to elaborate the inverse relation of the *rubber element* equation. Thus, for the calculation of the deflection in the sliding region only the Three Parameters Maxwell Model is used.

$$\delta_{s,x} = f_{3pM}(f_{s,x}) \tag{5.25a}$$

$$\delta_{s,y} = f_{3pM}(f_{s,y}) \tag{5.25b}$$

The Figure 5.7 shows the difference between the longitudinal deflection in the contact patch, calculated using the relations 5.25 (solid line) and the relations 5.15, thus without considering the sliding phenomenon.

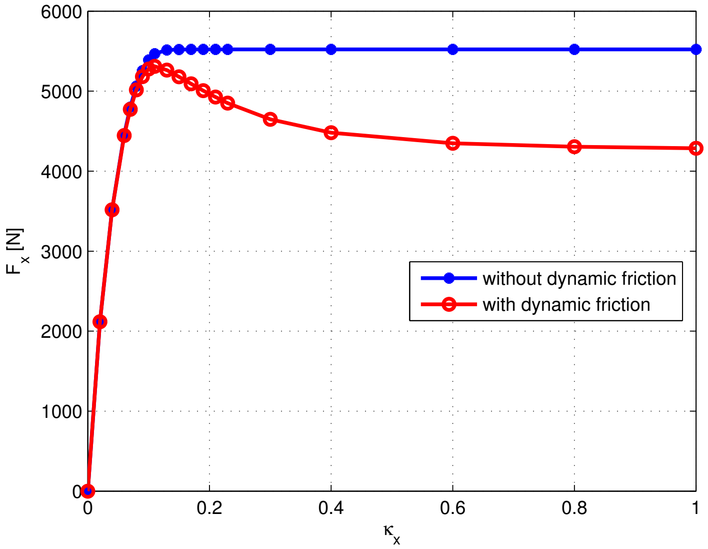

Figure 5.6: Diagram longitudinal slip - longitudinal force, comparison between a constant friction coefficient and a dynamic friction function, described by Equation 5.20

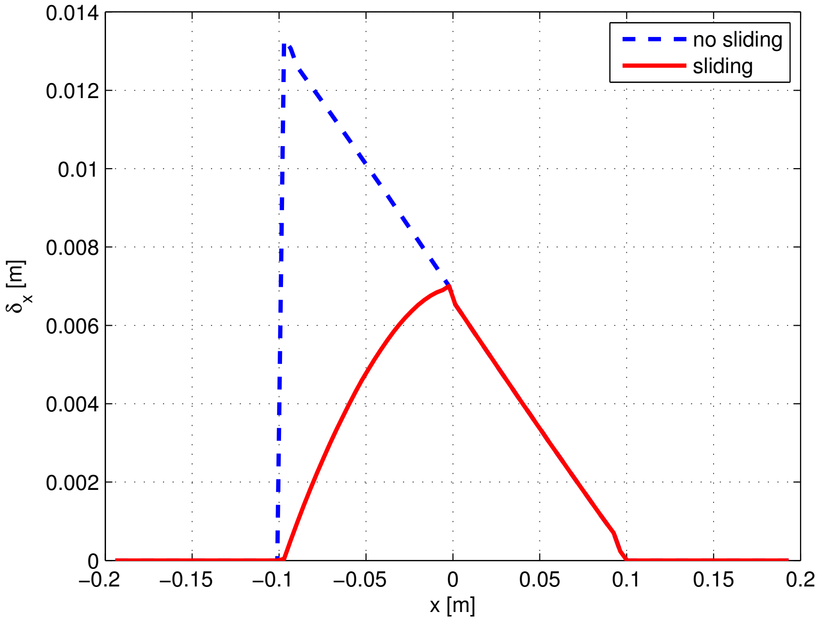

Figure 5.7: Longitudinal deflection of the bristles, $\kappa_x = 0.07$, difference between the deformation calculated by using Equation 5.25 (solid line) and the deformation calculated without considering the sliding region (dashed line)

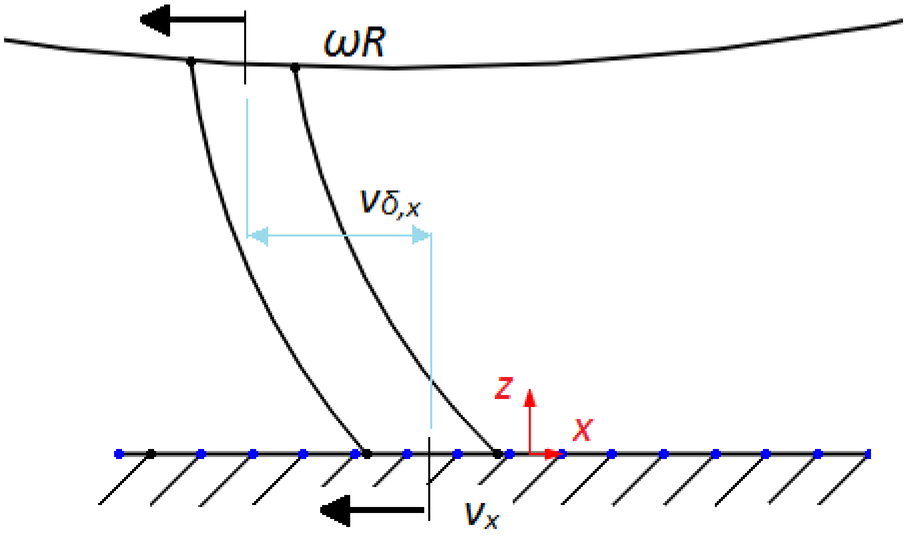

Figure 5.8: The deflection process along the x-axis, adhesion region

In Figure 5.8 the deflection process along the x-axis is shown. The top of the bristle moves with a velocity equal to ωR_{mean}, the bottom is stuck to the ground, thus it moves with the velocity of the road (v_x), the deflection velocity $v_{\delta,x}$ will be then calculated with Equation 5.18a. However, when the bristle slides, the bottom part of the bristle is not moving with the velocity of the road, but with an higher velocity. It is possible to calculate it using Equation 5.25. In fact the deformation velocity of the bristle will be equal to:

$$v_{\delta,x} = \frac{\delta_x(t) - \delta_x(t-dt)}{dt} \tag{5.26a}$$

$$v_{\delta,y} = \frac{\delta_y(t) - \delta_y(t-dt)}{dt} \tag{5.26b}$$

where $\delta_x = \delta_{a,x}$ and $\delta_y = \delta_{a,y}$ in the adhesion region, and $\delta_x = \delta_{s,x}$ and $\delta_y = \delta_{s,y}$ for the sliding region. Thus the sliding velocity of the bristle on the road will be:

$$v_{slid,x} = v_{s,x} - v_{\delta,x} \tag{5.27a}$$

$$v_{slid,y} = v_{s,y} - v_{\delta,y} \tag{5.27b}$$

where $v_{s,x}$ and $v_{s,y}$ are the slip velocities defined in Equation 5.18. This should be the correct velocities that have to be used in the equations for the calculus of the friction coefficient between road and tire. However, since their calculation is done after the estimation of the friction coefficient itself with the approximation considered in Equation 5.21, it generates numerical instability. A deeper focus could be done in order to stabilize the calculation, but this is not done in this work.

5.6 Load sensitivity factors

In reality the forces (longitudinal and lateral) developed in the contact patch, are function of the vertical load applied on the wheel. It means that the ratio F_x/F_z is not constant for different vertical load, but decreases for increasing vertical load. This behaviour is set into the model in two ways. When the wheel is cambered, for instance, the vertical load distribution is not equal on the contact patch, thus some lines will be more loaded than others. This uneven load distribution will affect the total force that the tire can develop. For each contact line the nominal vertical load is:

$$F'_{z0} = (m_{sprung} + m_{unsprung})g/l \tag{5.28}$$

where l is the number of lines of the model. Thus the normalized change for each contact line in the vertical load is:

$$df'_z(k) = \frac{\sum_{i=1}^{n} f_z(i,k) - F'_{z0}}{F'_{z0}} \tag{5.29}$$

The update forces for each line will be then:

$$f_x(i,k) = f_x(i,k) \cdot (1 - l_s df'_z(k)) \tag{5.30a}$$
$$f_y(i,k) = f_y(i,k) \cdot (1 - l_s df'_z(k)) \tag{5.30b}$$

where l_s is the sensitive load coefficient, equal to 0.15. The coefficient l_s affects the generation of forces for different distribution of vertical load (different inclination of the wheel), but maintaining constant the total vertical load F_z.

Moreover the generation of forces is function of the vertical load total value, thus a second load sensitivity factor has to be set up:

$$df_z = \frac{F_z - F_{z0}}{F_{z0}} \tag{5.31}$$

$$f_x(i,k) = f_x(i,k) \cdot (1 - l_{z,x} df_z) \tag{5.32a}$$
$$f_y(i,k) = f_y(i,k) \cdot (1 - l_{z,y} df_z) \tag{5.32b}$$

where F_{z0} is the nominal tire load, F_z is the effective vertical load on the wheel, $l_{z,x}$ and $l_{z,y}$ are the total load sensitivity factors, and they are set up in order to fit the experimental data in the best way. In the Figure 5.9 the effect of the total load sensitivity factor is shown, and it reflects the real phenomenon. The same phenomenon happens for the lateral force.

5.7 Quarter car model

The forces on each bristle, calculated with Equation 5.12 and 5.19, and modified with the load sensitivity factors and with the dynamic friction

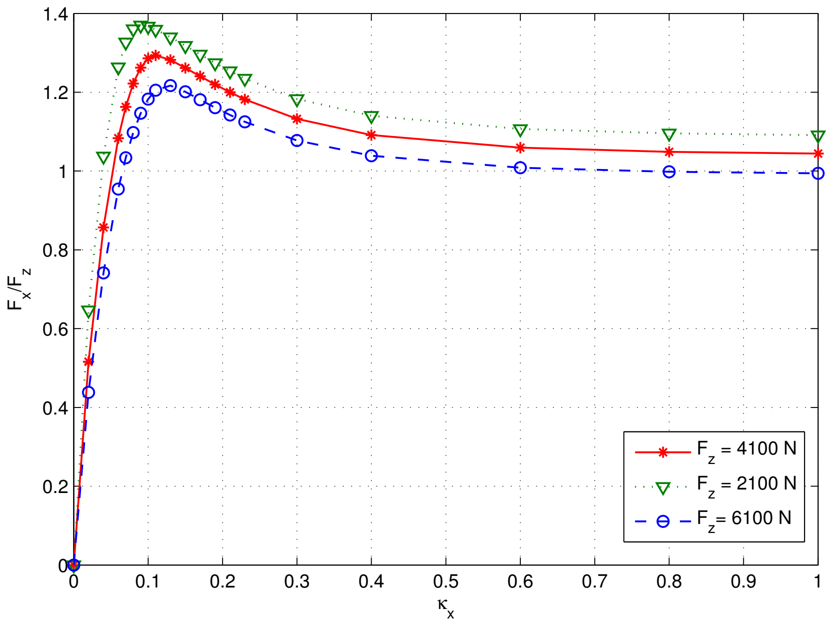

Figure 5.9: Dependence of the force generated on the total vertical load

relation, are added together to obtain the total values of the forces for each time step:

$$F_x(j) = \sum_{i=1}^{n} \sum_{k=1}^{l} f_x(i,k) \tag{5.33a}$$

$$F_y(j) = \sum_{i=1}^{n} \sum_{k=1}^{l} f_y(i,k) \tag{5.33b}$$

$$F_z(j) = \sum_{i=1}^{n} \sum_{k=1}^{l} f_z(i,k) \tag{5.33c}$$

The forces generated are included in a *quarter car* model, where the wheel is connected to the suspension, modelled as a spring and a damper, and to the sprung masses, loaded on top of the suspension. The initial vertical position z_t of the center wheel is set just some millimetres bigger than the unloaded radius R_w. The vertical force, output from the wheel model F_z represents the input for the quarter car model, and it gives as output the position of the sprung mass:

$$F_s = k_{susp} \cdot (z_t(j) - z(j)) + c_{susp} \cdot (\dot{z}_t(j) - \dot{z}(j)) \tag{5.34a}$$

$$\ddot{z}(j+1) = F_s/m_{sprung} - g \tag{5.34b}$$

$$\dot{z}(j+1) = \dot{z}(j) + \ddot{z}(j+1) \cdot dt \tag{5.34c}$$

$$z(j+1) = z(j) + \dot{z}(j+1) \cdot dt \tag{5.34d}$$

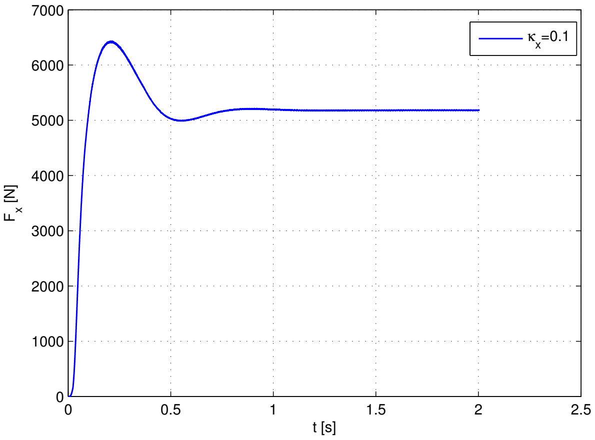

(a) Evolution in time of the longitudinal force for $\kappa_x = 0.1$

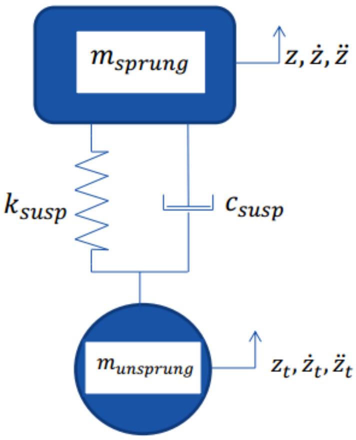

(b) Quarter car model

Instead for the unsprung mass:

$$\ddot{z}_t(j+1) = (F_z(j) - F_s)/m_{unsprung} - g \tag{5.35a}$$
$$\dot{z}_t(j+1) = \dot{z}_t(j) + \ddot{z}_t(j+1) \cdot dt \tag{5.35b}$$
$$z_t(j+1) = z_t(j) + \dot{z}_t(j+1) \cdot dt \tag{5.35c}$$
$$\tag{5.35d}$$

The j is the time index, and it should be little enough to avoid a bad discretization in time. The Figure 5.10a shows the evolution in time of the longitudinal force for a $\kappa_x = 0.1$ and $F_z = 4100$ N, and for $k_{susp} = 45000$ N/m and for $c_{susp} = 5000$ Ns/m.

Moreover, with the forces matrices f_x, f_y and f_z, it's possible to calculate the torque matrices:

$$M_x(j) = \sum_{i,k}(f_z(i,k) \cdot b(k)) \tag{5.36a}$$
$$M_y(j) = -\sum_{i,k}(f_z(i,k) \cdot \tan(\bar{\varphi}) \cdot z_t(j) + \sum_{i,k}(f_x(i,k) \cdot z_t(j)) \tag{5.36b}$$
$$M_z(j) = \sum_{i,k}(f_y(i,k) \cdot \tan(\bar{\varphi}) \cdot z_t(j)) + \sum_{i,k}(f_x(i,k) \cdot b(k)) \tag{5.36c}$$

It's important to notice that the torque calculated with Equation 5.36 are referred to the road plane (X_R, Y_R). This means that when the wheel is cambered the torque M_y, needed to calculate the rolling resistance, can't be calculated with Equation 5.36, but the effective resistance torque will be:

$$M_{y,w} = M_y \cdot \cos(\gamma) + \sin(\gamma) \cdot M_z \tag{5.37}$$

In this way the rolling resistance f_r can be calculated as:

$$f_r(j) = \frac{M_{y,w}(j)}{F_z(j) z_t(j)} \tag{5.38}$$

where F_z is the vertical load applied on the wheel, $z_t(j)$ is the distance between the contact patch central point and the wheel rotational axis (Y_W).

The relation in Equation 5.38 for the calculus of the rolling resistance coefficient is valid only when the longitudinal force f_x is zero (i.e. $\kappa_x = 0$), otherwise the torque $M_{y,w}$ becomes equal to the driving or braking torque, plus the rolling resistance torque.

5.8 Flexible lateral carcass

The original Brush Tire model assumes the carcass as infinitely stiff. However this is not the real case, since the carcass is not stiff, but flexible. In this work an attempt to include this feature has been made.

The sidewalls are modelled as rotating springs with a damper (the damper is needed to make the solution converges). They have an initial inclination α_0. When a lateral force occurs, the sidewalls rotate of an angle λ, defined in this way:

$$\lambda(j) = \frac{0.5 \cdot F_y(j) \cdot cos(\gamma) \cdot s_w + \lambda(j-1) d_r/dt}{k_r + d_r/dt} \tag{5.39}$$

where $k_r = 500$ Nm/rad and $d_r = 10$ Nms/rad are the elastic torsional stiffness and the torsional damping respectively of each sidewall. When the inclination of the sidewall changes, the values of the width b and radius R_w of the tread change as well. Defining the initial inclination of the sidewall with the angle α_0, each line of the model has an inclination about the Z_w axis equal to:

$$\alpha_{sw,0} = (-\alpha_0, \ldots, \alpha_0) \tag{5.40}$$

The inclination is updated with the angle λ in this way:

$$\alpha_{sw}(j) = \alpha_{sw,0} + \lambda(j) \tag{5.41}$$

Thus the new radius coordinate and width coordinate will be:

$$R_w = R_r + S_w \cdot cos(\alpha_{sw}(j)) \tag{5.42a}$$
$$b = w_r + S_w \cdot sin(\alpha_{sw}(j)) \tag{5.42b}$$

Figure 5.11 shows the lateral deflection of the carcass if a lateral force is applied. It is possible to observe the angle λ and the variation of the contact patch shape. When the tire is cambered, the deflection of the carcass causes a more even vertical force distribution, making the tire generate more lateral force, because of the load sensitivity coefficients. As shown in Figure 5.12 the camber allows a more even distribution of the vertical distribution, increasing the generated force.

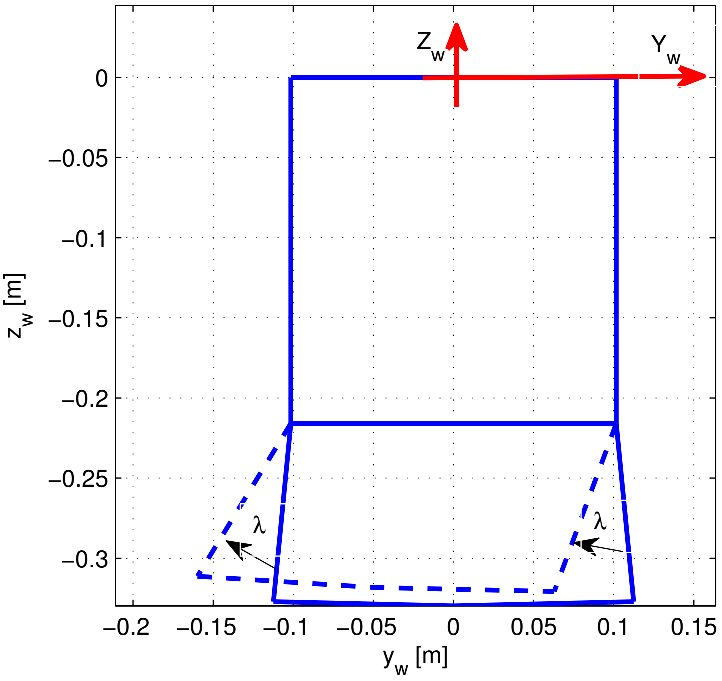
Z_w
Y_w
λ
λ
z_w [m]
y_w [m]
0
−0.05
−0.1
−0.15
−0.2
−0.25
−0.3
−0.2
−0.15
−0.1
−0.05
0
0.05
0.1
0.15

Figure 5.11: Flexible carcass (dashed line) and stiff carcass (solid line), $F_y = -4050$ N

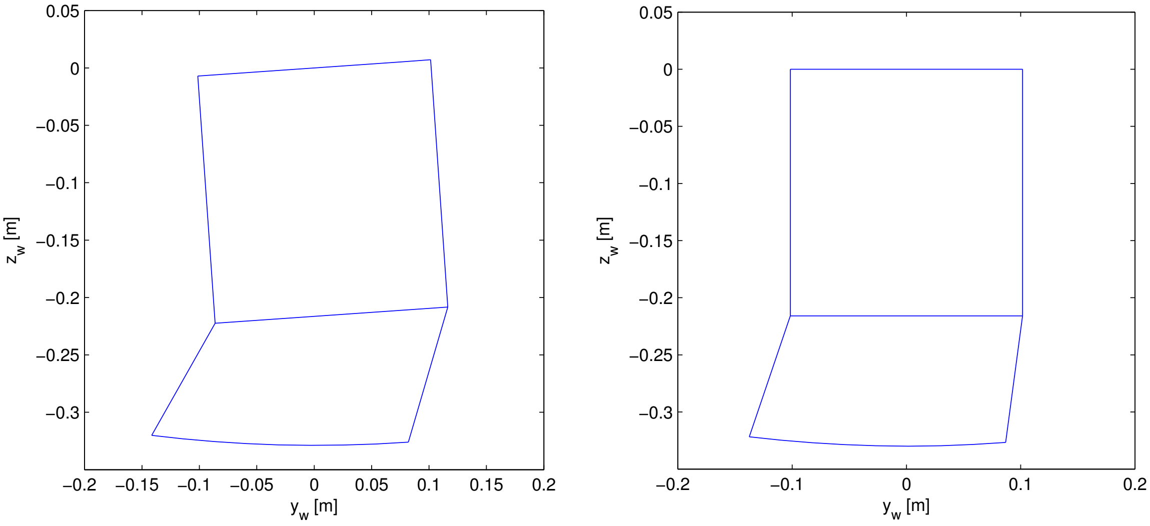

(a) $\gamma = 4°$, $\alpha = 2°$ **(b)** $\gamma = 0°$, $\alpha = 2°$

Figure 5.12: Carcass deformation for (a) cambered wheel and for (b) not cambered wheel

5.9 Energy and work

Depending on how the model is set up, different kinds of work and energy losses can be estimated. A first attempt to classify the energy losses is made up dividing them into *internal energy loss* and *external energy loss*: the first category is referred to the energy losses inside the *rubber element*, i.e. the visco-elastic and friction model of rubber, the second one is referred to the energy losses outside the *rubber element*, i.e. the sliding of the bristles with the road.

5.9.1 External losses

The main external loss in the wheel is caused by the sliding between the tread and the road surface in the sliding region of the contact patch. The model allows the prediction of the amplitude of the sliding region, where it's possible to know the force (longitudinal, lateral and vertical) applied in that part, as well as the sliding velocity of the bristles (see Equation 5.27). Thus the instantaneous power dissipated for each bristle element is:

$$p_{s,x}(i,k) = f_{s,x} \cdot v_{slid,x} \tag{5.43a}$$

$$p_{s,y}(i,k) = f_{s,y} \cdot v_{slid,y} \tag{5.43b}$$

The total instantaneous power dissipated through sliding is then:

$$P_s(j) = \sum_{i,k} p_{s,x}(i,k) + \sum_{i,k} p_{s,y}(i,k) \tag{5.44}$$

The work can simply be calculated integrating the power in time:

$$W_s(t) = \int_{t_0}^{t} P_s \mathrm{d}t \tag{5.45}$$

Numerically, the integer is approximated with the simple trapezoidal rule:

$$W_s(j) = \frac{P_s(j) + P_s(j-1)}{2} dt \tag{5.46}$$

The Equation 5.46 describes the work made by sliding forces in the time interval dt, thus the total work developed in time will be the sum of the work developed for each time step.

5.9.2 Internal losses

The internal losses are identified as the energy dissipation that occurs inside the *rubber element*. As previously described, the rubber element is made of three parts: an elastic element, a viscous element and a friction element. The first one, modelled as a spring doesn't dissipate energy, since all the energy used to compress the spring is released in the recovery phase. The viscous and the friction elements, instead, cause energy losses.

Each bristle is made of three rubber elements for each direction, thus it is possible to calculate the energy dissipated for internal friction and the total internal energy for each direction. The energy dissipation for friction is:

$$w_f = \int \bar{f}_f \cdot \mathrm{d}\bar{s} \tag{5.47}$$

Dividing it into the three components along the three axis directions and using the trapezoidal rule for the approximation of the integrals, it results:

$$w_{f,x}(j) = \frac{f_{f,x}(j) + f_{f,x}(j-1)}{2} \cdot \big(\delta_x(j) - \delta_x(j-1)\big) \tag{5.48a}$$

$$w_{f,y}(j) = \frac{f_{f,y}(j) + f_{f,y}(j-1)}{2} \cdot \big(\delta_y(j) - \delta_y(j-1)\big) \tag{5.48b}$$

$$w_{f,z}(j) = \frac{f_{f,z}(j) + f_{f,z}(j-1)}{2} \cdot \big(\delta_z(j) - \delta_z(j-1)\big) \tag{5.48c}$$

w_f is a matrix describing the friction work of each bristle. Thus the total energy dissipated by friction in the time dt is:

$$W_{f,x}(j) = \sum_{i,k} w_{f,x}(j) \tag{5.49a}$$

$$W_{f,y}(j) = \sum_{i,k} w_{f,y}(j) \tag{5.49b}$$

$$W_{f,z}(j) = \sum_{i,k} w_{f,z}(j) \tag{5.49c}$$

$$W_f(j) = W_{f,x}(j) + W_{f,y}(j) + W_{f,z}(j) \tag{5.49d}$$

The energies fraction of each time-step will then be added together. In a case of perfect elasticity (no friction and no viscous effects) the sum of the energies dissipated in time is different than zero (because of oscillations caused by the physics of the problem), but the mean in time is always null. In real cases, the mean has a positive rate, different than zero. The friction effect causes the dissipation of a part of energy since the force released in the recovery phase is not the same of the loading phase. The dissipated energy will be then equal to the loop-area described in the force-displacement graph and it represents its rate-independent fraction. Thus it will create a rolling resistance torque, because the wheel is rolling, no matter its speed. The energy rate dissipated by internal friction will be just the derivatives in time of the previous relations:

$$\dot{W}_{f,x}(j) = \frac{W_{f,x}(j) - W_{f,x}(j-1)}{dt} \tag{5.50a}$$

$$\dot{W}_{f,y}(j) = \frac{W_{f,y}(j) - W_{f,y}(j-1)}{dt} \tag{5.50b}$$

$$\dot{W}_{f,z}(j) = \frac{W_{f,z}(j) - W_{f,z}(j-1)}{dt} \tag{5.50c}$$

$$\dot{W}_f(j) = \frac{W_f(j) - W_f(j-1)}{dt}(j) \tag{5.50d}$$

The total energy dissipated by the rubber element is:

$$w_t = \int \bar{f} \cdot \mathrm{d}\bar{s} \tag{5.51}$$

where $\bar{s}$ is the displacement vector of the bristle. Applying the same rule as before, it results:

$$w_{t,x}(j) = \frac{f_x(j) + f_x(j-1)}{2}(\delta_x(j) - \delta_x(j-1)) \tag{5.52a}$$

$$w_{t,y}(j) = \frac{f_y(j) + f_y(j-1)}{2}(\delta_y(j) - \delta_y(j-1)) \tag{5.52b}$$

$$w_{t,z}(j) = \frac{f_z(j) + f_z(j-1)}{2}(\delta_z(j) - \delta_z(j-1)) \tag{5.52c}$$

$$\tag{5.52d}$$

Also in this case w_t is the matrix of the energy dissipated of each bristle. The total energy dissipated in the time dt will be the sum of the energies of each bristle:

$$W_{t,x}(j) = \sum_{i,k} w_{t,x}(j) \tag{5.53a}$$

$$W_{t,y}(j) = \sum_{i,k} w_{t,y}(j) \tag{5.53b}$$

$$W_{t,z}(j) = \sum_{i,k} w_{t,z}(j) \tag{5.53c}$$

$$W_t(j) = W_{t,x}(j) + W_{t,y}(j) + W_{t,z}(j) \tag{5.53d}$$

For a generic time t^* the total energy dissipated until then will be the cumulative value of W_t, i.e. the sum of all the values from $t = 0$ to $t = t^*$. Instead the rate of internal energy dissipated is the derivative in time of the previous relations, thus:

$$\dot{W}_{t,x}(j) = \frac{W_{t,x}(j) - W_{t,x}(j-1)}{dt} \tag{5.54a}$$

$$\dot{W}_{t,y}(j) = \frac{W_{t,y}(j) - W_{t,y}(j-1)}{dt} \tag{5.54b}$$

$$\dot{W}_{t,z}(j) = \frac{W_{t,z}(j) - W_{t,z}(j-1)}{dt} \tag{5.54c}$$

$$\dot{W}_t(j) = \frac{W_t(j) - W_t(j-1)}{dt}(j) \tag{5.54d}$$

5.10 Conclusion

In this section the Multi-Line Brush model developed for this work has been explained and discussed. The Brush Tire model and the models for the prediction of the rubber behaviour have been combined together in order to obtain a more realistic tire model, that can deal with dynamics and energy dissipation as well. The visco-elastic and friction characteristics of rubber elements are modelled with the *Three Parameters Maxwell* model and the *Masing* model respectively. The dynamics of each rubber elements is, instead, governed by the dynamics of the Brush Tire model. The model obtained is not simple, the number of parameters is much more greater than the Brush Tire model, but it is more complete and with a strong physical basis.

Chapter 6

Validation and results

In this chapter the results deriving from the Multi-Line Brush Tire model are analysed and compared with the *Magic Formula* Tire model and some experimental data. In the first section, the results are validated, and in the second section, all the other results, coming from the model, are discussed and analysed, based on the literature about tire behaviour.

6.1 Validation

In this section the results of the Multi-Line Brush model are compared with the Magic Formula Tire model by Pacejka and with some experimental results. These are steady-state tests, meaning that the time response of the tire is not taken into account. Data for the Magic Formula Tire model is available for the pure slip tests (pure longitudinal and pure lateral slip). Experimental data is available just for combined slip.

6.1.1 Comparison with Magic Formula

The Figure 6.1 shows a comparison between the Magic Formula Tire model and the Multi-Line Brush Tire model for the longitudinal pure slip. The two curves are very similar, except for the elastic region, where the two models behave differently in function of the vertical force applied. It's important to notice that in this case the Magic Formula Tire model is just given as that graph, all the data about the tire are not available. This could be the cause of the difference in the Figure 6.1. Furthermore, in this case the Magic Formula results are symmetric about the y-axis, which is why in the graph just positive values of longitudinal slip κ_x are reported.

Figure 6.2 shows a comparison between the Magic Formula Tire model and the Multi-Line Brush Tire model for the lateral force. The two curves agree quite well, except for very low vertical load. Again, all the data are not available, so the values of the Multi-Line Brush Tire model are calculated in order to fit as good as possible the Magic Formula Tire model results. That could be the cause of the not so good fit in some parts of the curve. However, the approximation is still acceptable. A possible solution to the

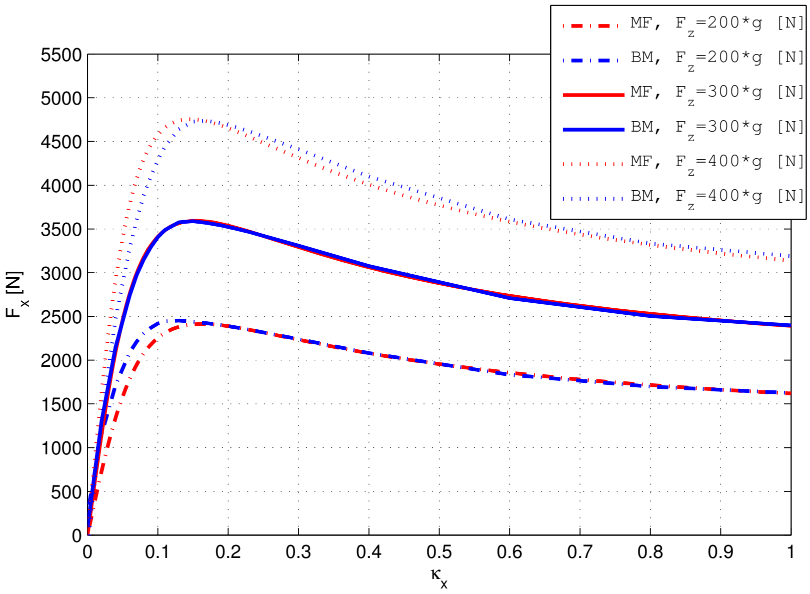

Figure 6.1: Longitudinal force vs longitudinal slip, comparison between Magic Formula Tire model (red lines) and Multi-Line Brush model (blue lines) for different vertical load on the wheel

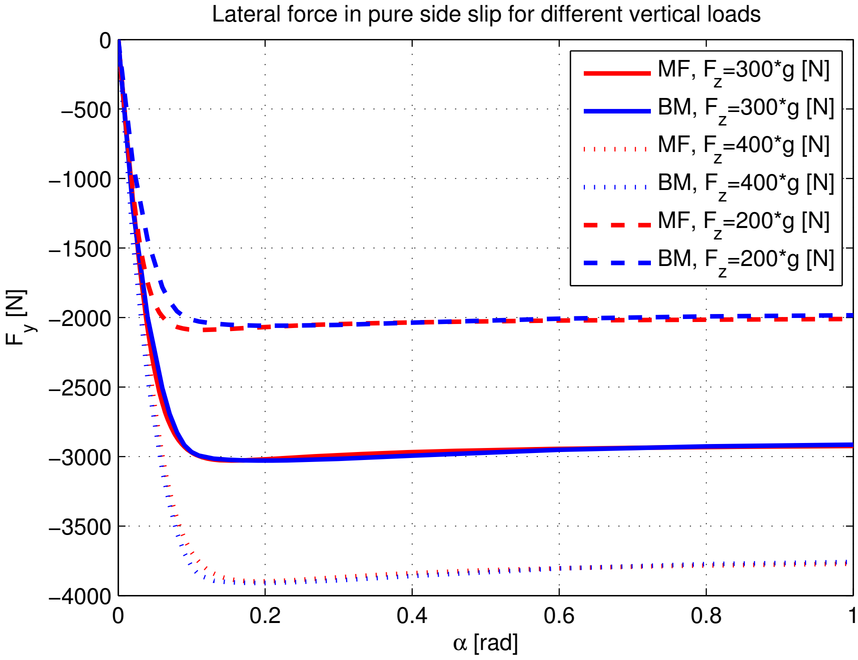

Figure 6.2: Lateral force vs side slip, comparison between Magic Formula Tire model(red line) and Multi-Line Brush Tire model (blue line) for different loads on the wheel

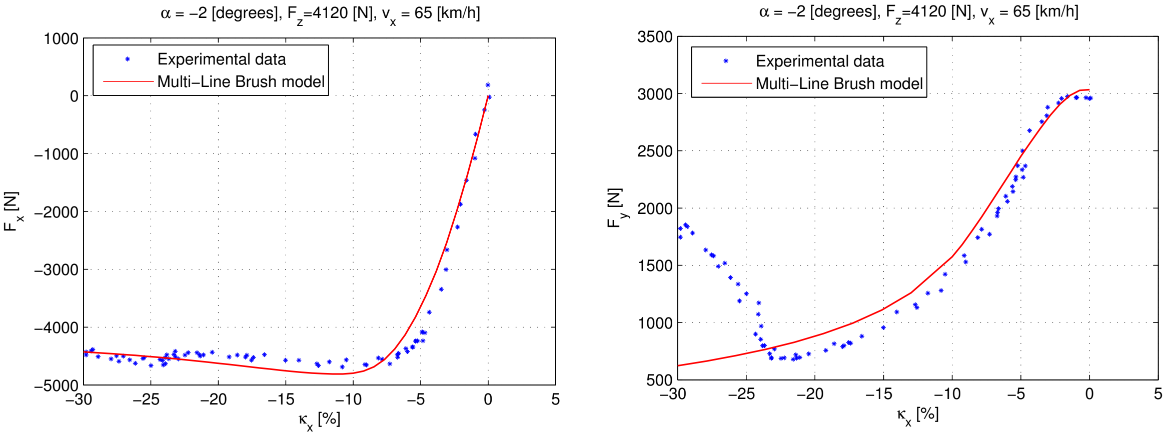

(a) Longitudinal force F_x

(b) Lateral force F_y

Figure 6.3: Comparison between experimental data (marker) and Multi-Line Brush Tire model (Red line) for $\alpha = -2°$

difference between the two methods in the elastic region could be the linear elastic stiffness in the vertical direction. Indeed, in real cases the vertical stiffness of the tire is not linear, but it could be approximated better with a cubic curve. In that case, for high vertical load, the contact patch is bigger, it means that more bristles are in contact, thus the longitudinal and lateral force transmitted should be bigger.

6.1.2 Comparison with experimental data

Some data regarding an experimental test on a 225/45R17 Pirelli tire have been available to compare with data coming from the Multi-Line Brush Tire model. The tests are conducted for two different fixed slip angle ($\alpha_1 = -2°$ and $\alpha_2 = 4°$), whereas the longitudinal slip κ_x varies. The longitudinal velocity of the vehicle is fixed to 65 km/h and the normal load is constant (except for dynamic oscillations) equal to 4120 N. From the data, knowing the loaded radius of the wheel (measured data) and the unloaded one (from the tire geometry), it's possible to determine the vertical stiffness of the wheel. Later, the values of lateral and longitudinal stiffness are derived in such a way that the curve of the Multi-Line Brush Tire model fits the experimental data of longitudinal and lateral force in the elastic region. The data about the friction between the tire and the ground are derived from the sliding region of the force-slip curve, in order to fit as best as possible the experimental data. The results are shown in Figure 6.3 for a fixed slip angle of -2° and in Figure 6.4 for a slip angle of 4°.

It's possible to observe how the Multi-Line Brush Tire model generally agrees with the experimenetal data, except for Figure 6.3b, where for high values of longitudinal slip the lateral force decreases almost instantaneously. It's hard to say why this behaviour occurs, since the author of this work has not performed the experimental test, and there is no complete and commented report of the experimental tests. Of course, the model in the two

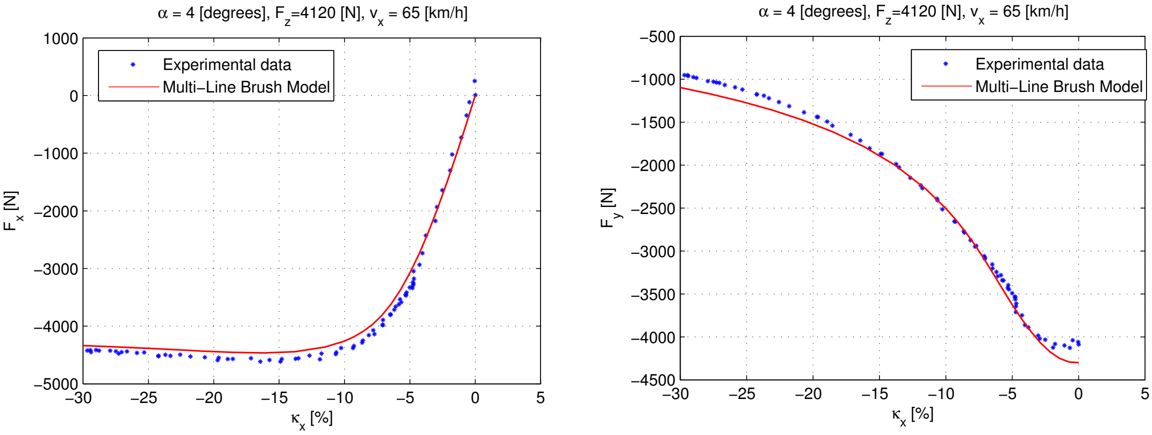

(a) Longitudinal force F_x **(b)** Lateral force F_y

Figure 6.4: Comparison between experimental data (marker) and Multi-Line Brush Tire model (Red line) for $\alpha = 4°$

tests ($\alpha = -2°$ and $\alpha = 4°$) has exactly the same values (stiffness, friction, vertical load etc), except for the slip angle. This means that the model can simulate various situations of combined slip, maintaing costant its coefficients, which are characteristics of the particular tire. The coefficients used in the model are reported in the Appendix C.

6.2 Results

The previous paragraph shows that the Multi-Line Brush Tire model reflects the results obtained with the *Magic Formula* Tire model and experimental data for combined slip. After this validation, a series of simulations (for which there are no experimental data available at the moment) are performed with the Multi-Line Brush Tire model. The results from those simulations are presented and discussed in this chapter.

6.2.1 Effect of camber

In Figure 6.5 the lateral force is plotted as function of the slip angle α and the camber angle γ, with $\kappa_x = 0$. As experimental data suggest, a positive camber wheel (positive if the angle γ is positive about the x-axis) increases the lateral force for positive slip angle α. This because the camber angle counteracts the carcass deflection, making the distribution of the vertical load more even, thereby increasing the lateral force. The effect of camber is very clear in Figure 6.6, where the lateral force distribution in the contact patch is shown. For a cambered wheel (on the right) the distribution of the lateral force is more even than for the non-cambered wheel. This is because the vertical load distribution is different. The dark zones represent the bristles that create more force, thus, in the second figure, there are more dark zones, especially in the middle of the contact patch, instead of the figure

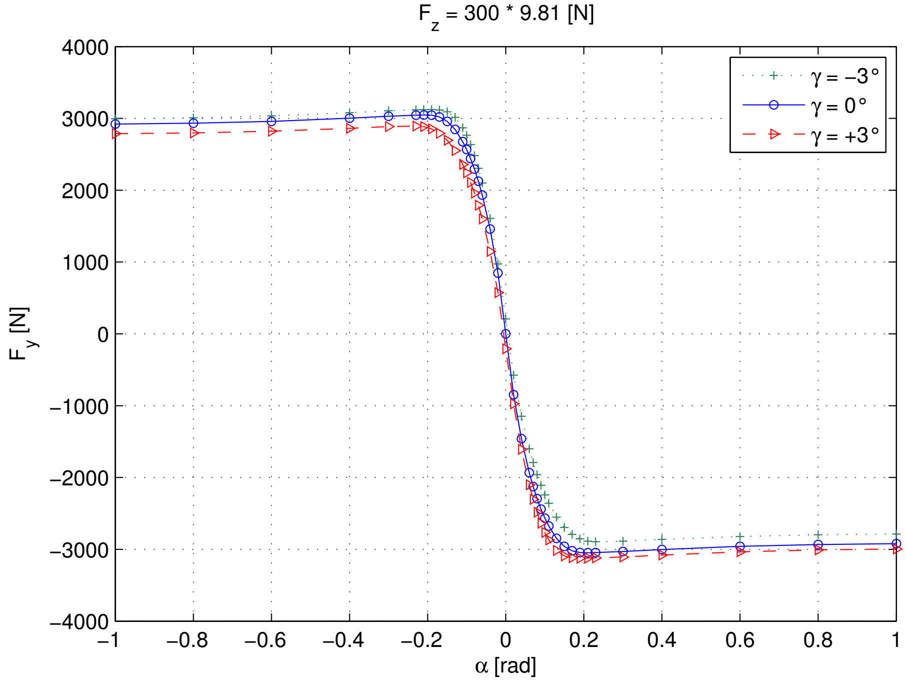

Figure 6.5: Lateral force for different camber angles

on the left, where the dark zones are positioned near the lateral edge of the contact patch, reducing the total lateral force generated.

It exists an optimum value for the camber angle that maximize the lateral force generated for a given slip angle α. As an example the Figure 6.7a shows this behaviour where, in this case, the maximum force generated corresponds to an angle slightly larger than 3°. A camber angle creates a lateral force even with slip angle equal to zero. It is called *camber thrust* and the force generated is shown in Figure 6.7b.

In Figure 6.8 the contact patch with the bristles which are sliding (pink zones) is shown, for the slip angle $\alpha = 2°$. On the left, the wheel is not cambered, the contact patch is shifted a bit more through the positive part of the y-axis than in the cambered wheel (on the right). The tilting angle γ makes the distribution of the lateral force to be more even, indeed in the not cambered wheel 1387 bristles are in contact with the ground, against the 1402 of the cambered wheel (with $n = 100$ and $l = 25$), this means that the vertical load in the cambered wheel is more even on the contact patch, thus its distribution is more even. This causes a total lateral force bigger in the cambered wheel case, than in the not cambered, because of the load distribution factors.

6.2.2 Combined slip

The comparison of the Multi-Line Brush Tire model with the experimental data of the previous paragraph deals with a case of combined slip. In this section different situations are studied: combined slip with zero camber angle

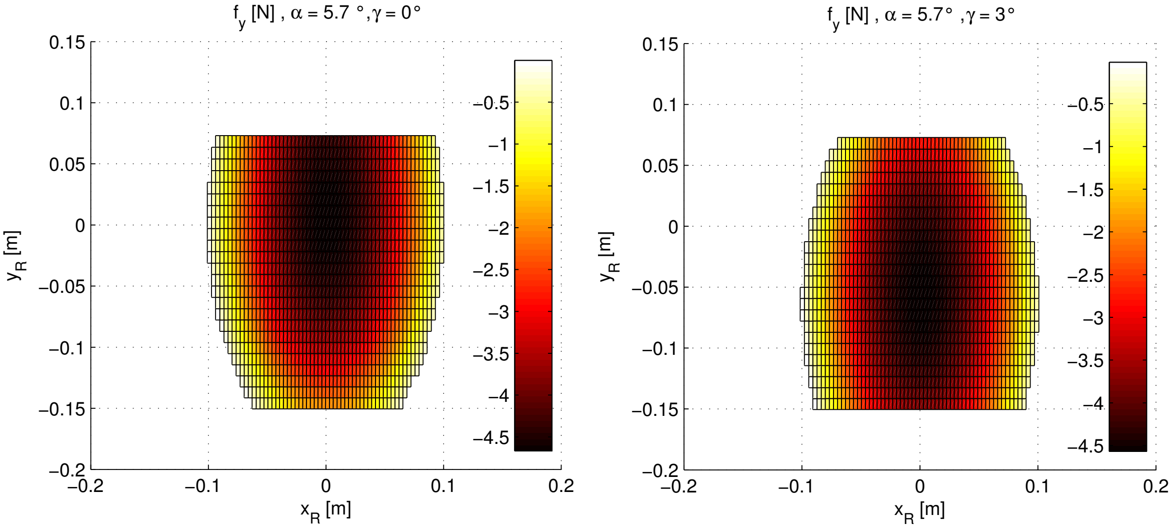

(a) $\gamma = 0°$ **(b)** $\gamma = 3°$

Figure 6.6: Lateral force distribution on the contact patch for (a) non-cambered wheel (a) and (b) for a positive cambered wheel, both for $\alpha = 5.7°$ ($n = 100$, $l = 25$)

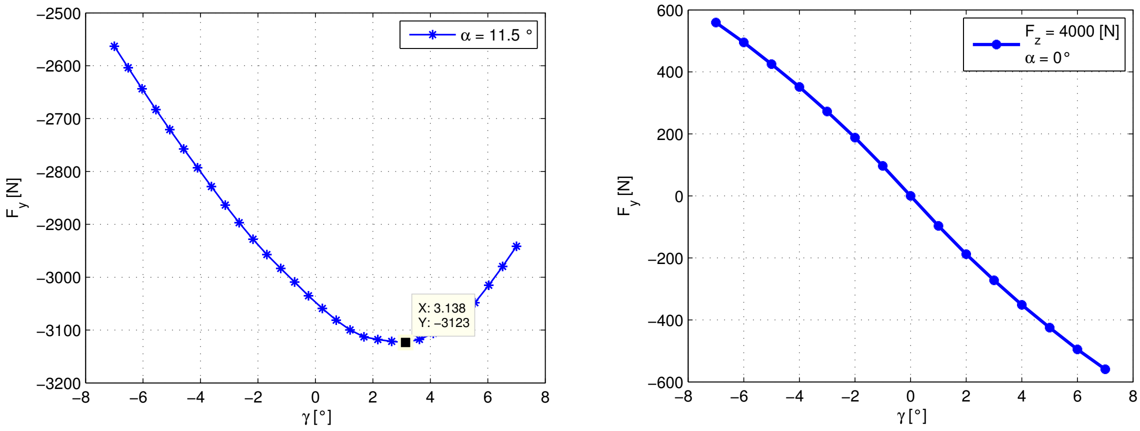

(a) $\alpha = 11.5°$ **(b)** $\alpha = 0°$

Figure 6.7: Lateral force vs camber angle for $\alpha = 11.5°$ in (a); camber thrust ($\alpha = 0°$) for different camber angles γ in (b).

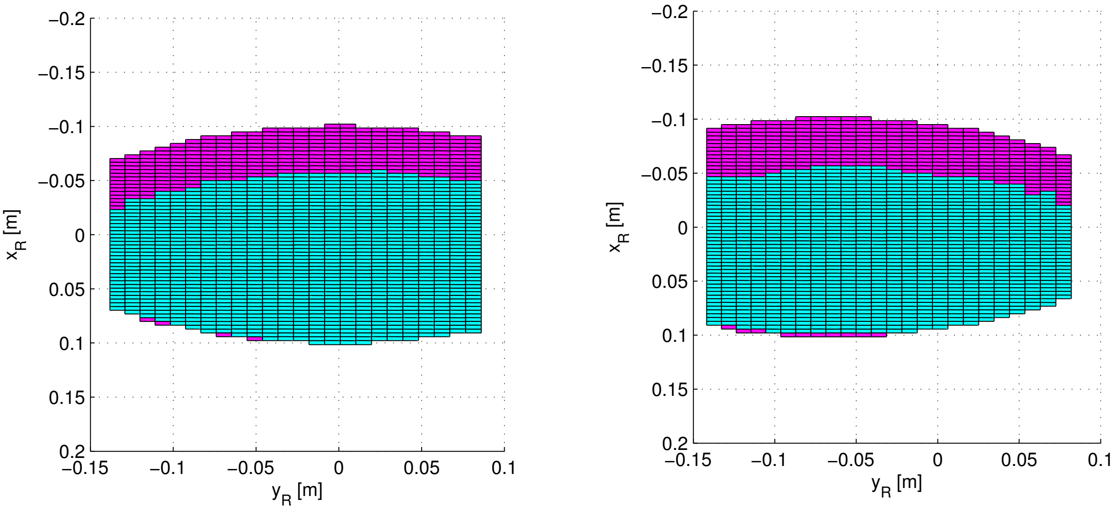

(a) $\gamma = 0°$, $F_y = -2541$ N

(b) $\gamma = 3°$, $F_y = -2928$ N

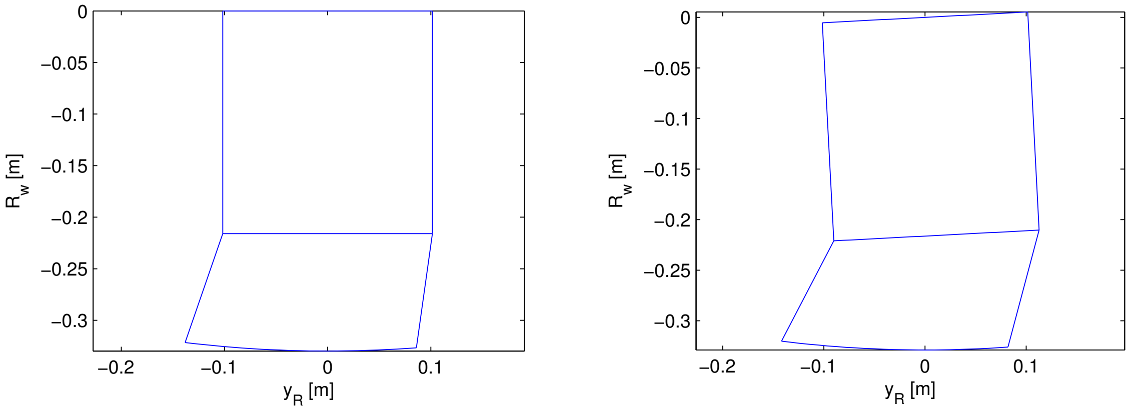

(c)

(d)

Figure 6.8: Contact patch with sliding region in pink in 6.8a and 6.8b; frontal view of half wheel in 6.8c and 6.8d, $F_z = 4$ kN, $\alpha = 3°$

first, and combined slip with various camber angle later.

Longitudinal and lateral force with zero camber angle

Figure 6.9 shows the force-slip diagram for a null camber angle and $F_z = 4000$ N. In Figure 6.9a the longitudinal slip κ_x varies from -1 to +1, with five different slip angle α. As can be seen, the longitudinal force is maximized for a null slip angle, instead with increasing slip angle the longitudinal force decreases. This is because the total force that can be transmitted between the tire and the road is limited by friction, thus if longitudinal and lateral slip exists simultaneously, the total force will be split in two components, basing on the friction coefficients of each direction. It's important to notice that the drop of the longitudinal force is not function of the sign of the slip angle, because the lateral friction coefficient is considered independent on the direction of the lateral sliding velocity. From Figure 6.9b it's a bit hard

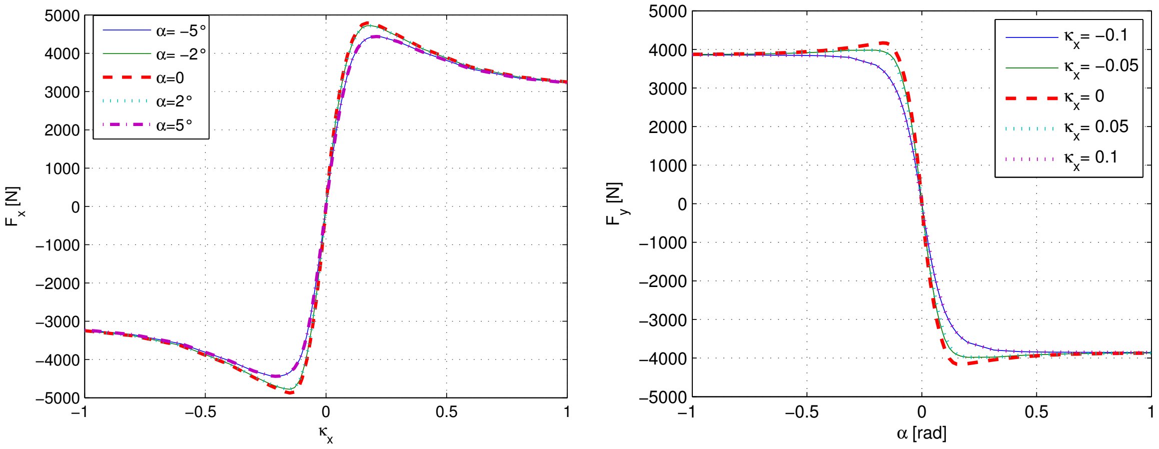

(a) Longitudinal force **(b)** Lateral force

Figure 6.9: Combined slip for $\gamma = 0°$

to see, but in the elastic region, near the peak of the curve, the force values corresponding to negative values of longitudinal slip are slightly greater than those for positive values of κ_x. It means that in the braking phase ($\kappa_x < 0$) the lateral force achievable for a given slip angle is bigger than that one during the accelerating phase with the same slip angle, and the same value of longitudinal slip (positive). This behaviour is predicted also by the simple brush theory.

Effect of camber in combined slip

In this section the effect of a camber angle for the force generation on combined slip is studied. Figure 6.10 shows the effects of camber angle on the longitudinal force for two slip angles. Regardless the sign of the slip angle and of the inclination of tilting angle, the maximum longitudinal force is always achieved with zero camber angle. The figures are focused just on the peaks of the curves, because the difference will not be evident. From Figure 6.10a, it is possible to see that for positive side slip angle and positive camber angles the force generated is higher than for negative values of camber angle. A possible explanation could be that a positive camber angle associated to a positive slip angle makes the vertical distribution more even, thus a bigger force (both lateral and longitudinal) can be generated, comparing with the case of negative slip angle. The same could be say about the Figure 6.10b.

The camber has a completely different effect on the lateral force. As said in the previous chapter, a positive camber angle coupled with a positive slip angle makes the lateral force increase. The curves in Figures 6.11 show this effect.

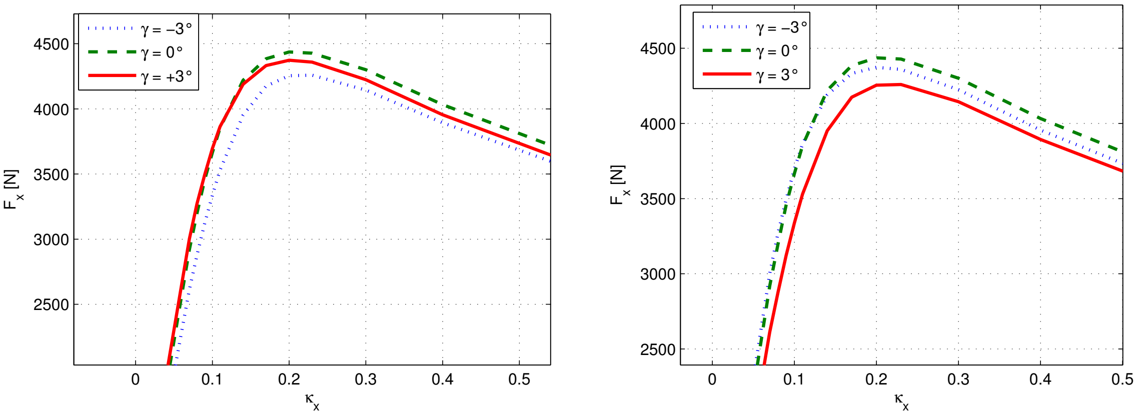

(a) $\alpha = 5°$ (b) $\alpha = -5°$

Figure 6.10: Longitudinal force with fixed slip angle and various camber angles

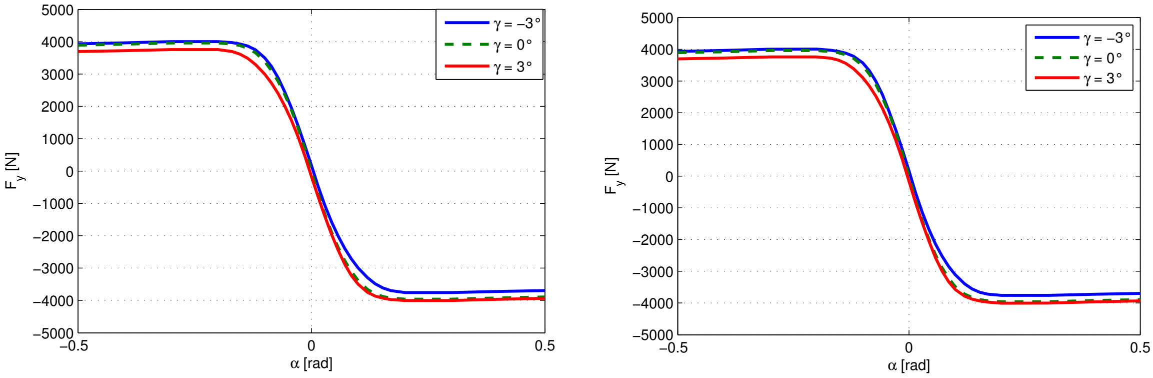

(a) $\kappa_x = 5\%$ (b) $\kappa_x = -5\%$

Figure 6.11: Lateral force with fixed longitudinal slip and various camber angles

6.2.3 Self-aligning torque

The self-aligning torque M_z arises from the different distribution of the lateral force along the contact patch. It's calculated using Equation 5.36c of the previous chapter. The results are shown in Figure 6.12. The values of the M_z torque show a behaviour similar to reality in the first part, where the torque presents a peak. For high slip angles α, the torque value reaches an asymptote, different than zero. This is because for high values of side slip angle all the bristles are sliding, thus the distribution of the lateral force, that generates the aligning torque, has the same "shape" of the vertical force, with a corrective factor equal to the friction between the road and the tread. However, the distribution of the vertical force has a parabolic distribution with the total force shifted a bit forward and, since the lateral force has the same kind of distribution, it creates a constant torque. There are no experimental data available at this moment, in order to compare the results

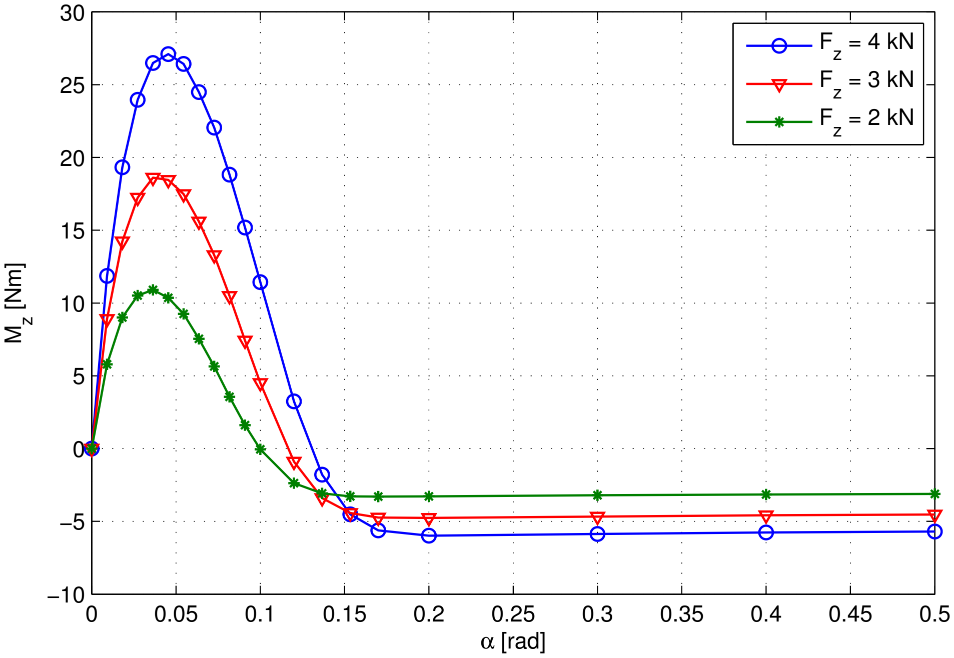

Figure 6.12: Self aligning torque M_z for different vertical loads

obtained with the Multi-Line Brush Tire model.

6.2.4 Rolling resistance

As explained in the paragraph 2.2.1, the main contribution to the rolling resistance is given by the non-symmetric vertical load distribution about the y-axis. This is shown in Figure 6.13a, where the vertical application point (i.e. the point where the force has zero moment) is not positioned along the vertical axis of the tire, but shifted forward, at $x_R = 0.0033$ m. This creates a rolling resistance coefficient equal to $f_r = 0.0105$.

The main reason for this kind of distribution is the internal friction force, acting inside the *rubber element*. Using the Masing model, the internal friction forces have the behaviour shown in Figure 6.13b for a single line. It's possible to see that in the leading edge, where the bristles start to deflect, the friction force increases, reaching a maximum value, meaning that all the Jenkin elements in the Masing model are sliding. When the bristle starts to decompress, the forces change sign, until all the elements slide again. This change in sign causes an imbalance in the force distribution, the bristles corresponding to positive x values (in the front of the tire) generate a vertical force greater than the ones corresponding to negative x values. This effect allows the shifting of the application point forward, generating a resistant M_y torque on the wheel axis. In order to have a constant velocity speed of the wheel, a tractive torque must be applied at the wheel. In order to transmit the torque to the road, a little sliding between tread and road must occur but in the same time this sliding makes the rolling coefficient slightly

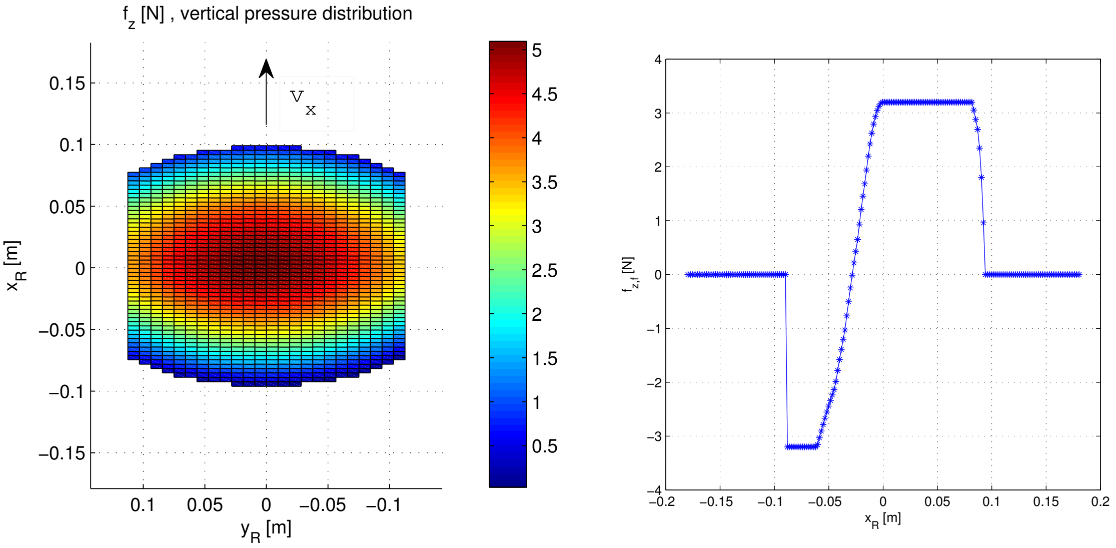

(a) Vertical force distribution $f_r = 0.0105$, $F_z = 4$ kN

(b) Internal friction forces, calculated using the Masing model

Figure 6.13: Vertical force distribution ($n = 100$, $l = 25$) in 6.13a; internal friction forces using Masing model in 6.13b, for one single line

increases. However, this effect is not considered in this work, since it's not easy to be implemented in a Matlab code and the error committed with this approximation is quite small. The peak value of the friction force is function of the coefficients in the Masing model, thus a deeper analysis on the tire material should be done, in order to identify with good approximation these parameters.

Dependence on vertical load

The literature suggests that the rolling resistance coefficient is vertical load dependent, however, its behaviour depends a lot on the tire construction and materials. According to [17] the rolling resistance coefficient generally increases for increasing vertical load, but for some tires it decreases. The Figure 6.14a shows the results coming from the model. In this case the rolling resistance coefficient decreases with increasing vertical load, this can be explaining considering that, in the model, the vertical stiffness of the tire is linear, instead of decreasing with the normal load. If a cubic elastic stiffness is introduce in the model, the rolling coefficient will increase, since a decreasing vertical stiffness makes the rolling resistance coefficient increases, as can be seen from Figure 6.14b. In order to obtain more precise data about the behaviour of rolling resistance under different loads, the data about the Masing model should be investigated deeper, because in this situation, all the Jenkin elements are sliding when the tire is rolling, thus the friction force can't increase, even if the vertical load (thus the vertical deflection) increases.

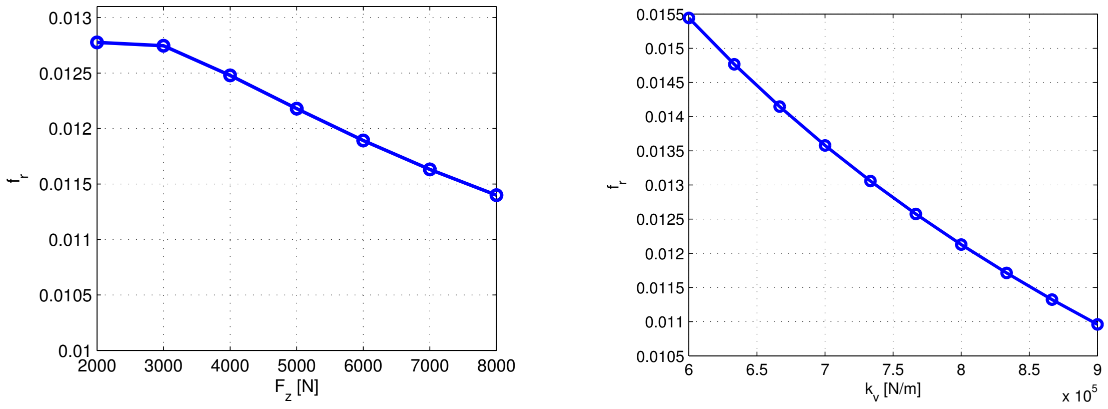

(a) **(b)**

Figure 6.14: Dependence of the rolling resistance on the vertical load F_z in 6.14a; Dependence of the rolling resistance on the vertical stiffness in 6.14b

Dependence on the longitudinal speed

The rolling resistance coefficient is function of the vehicle speed [21]. Typically it increases with increasing vehicle speed, however this function is not so distinct, but depends on the tire characteristic and construction. But, generally, the rolling resistance increases with increasing vehicle speed. The results are shown in Figure 6.15. The dependency on the rolling speed arises from the dynamic model of the *rubber element*, in effect the viscous part is the only rate-dependent element, and, for vehicle typical speed, the loss factor increases with increasing speed, before reaching the peak.

The behaviour of the coefficient reflects the Bode diagram of the Three Parameters Maxwell model. Thus it can simulate the reality until a certain limit of speed. The value of the limit depends on the value of the viscous coefficient in the visco-elastic model along the z-direction, as can be seen in Figure 6.16.

For increasing values of vertical viscous coefficient the rolling resistance increases in its maximum value and decreases the velocity corresponding to the maximum value. After the peak the rolling resistance decreases because of the frequency response of the Three Parameters Maxwell model, where the loss factor has a peak and then it decreases.

Dependence on camber angle

The tilting angle of the wheel, i.e. the camber angle, affects the rolling resistance coefficient. In Figure 6.17 it is shown two simulations obtained from the model with two different vertical tire stiffness. For the "hard" tire (circle markers) the camber has almost no effect. Actually for small angles the rolling resistance coefficient decreases a bit, but the decrease is almost negligible. For the "soft" wheel instead, the camber angle has a

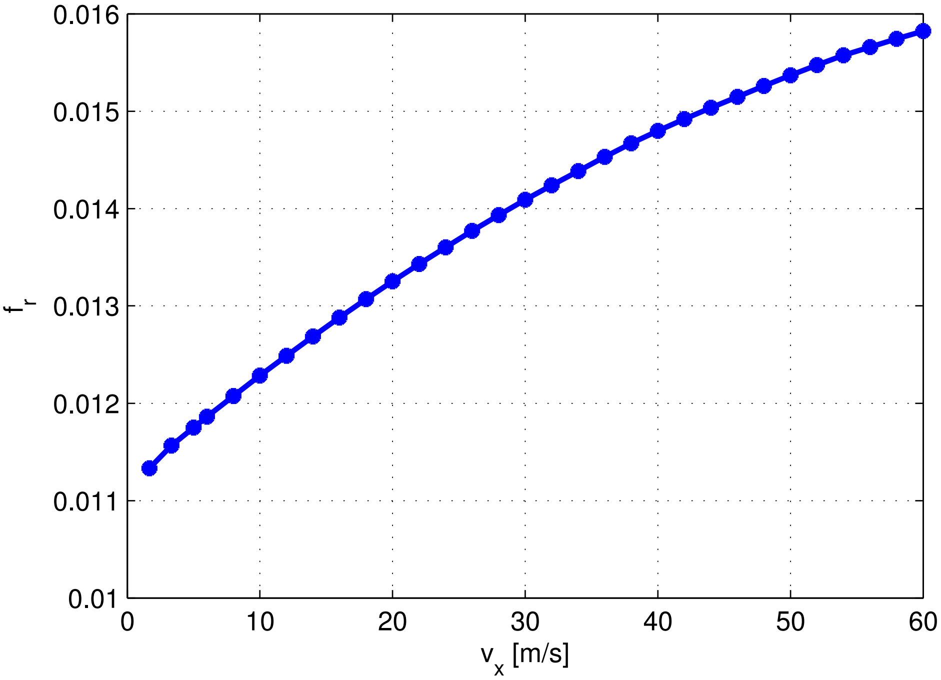

Figure 6.15: Dependence of the rolling resistance coefficient on the longitudinal speed

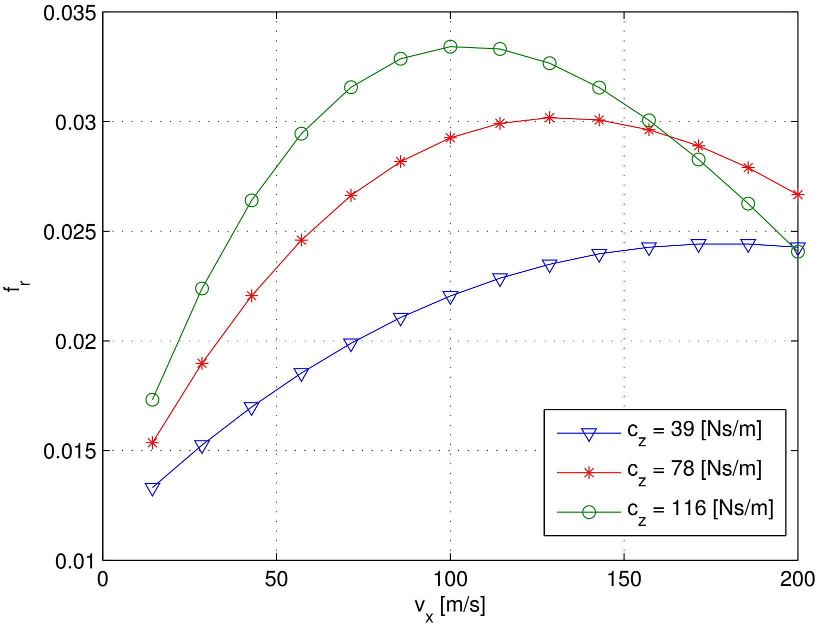

Figure 6.16: Rolling resistance coefficient for different viscous coefficient in the z-axis

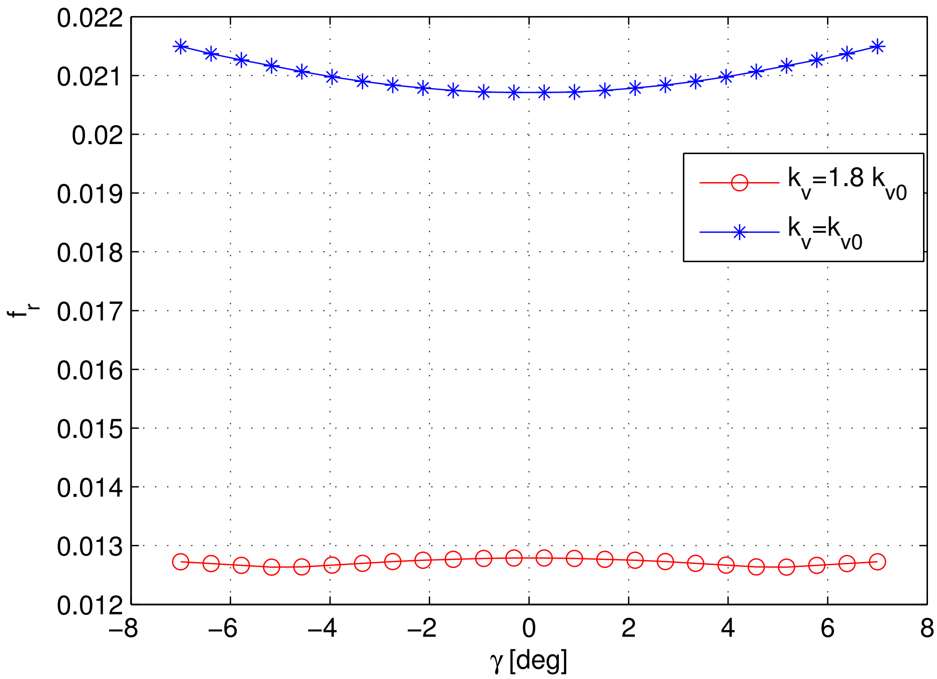

Figure 6.17: Rolling resistance dependence on camber angle, for two different vertical tire values of stiffness

more evident effect, with increasing the camber angle the rolling resistance coefficient increase. The coefficient has been calculated using Equation 2.7.

Dependence on the tire geometry

It's predictable that the tire geometry has a certain influence on the rolling resistance. In Table 6.1 the "soft" tire is used, in such a way that the influence of camber can be observed. The main geometric dimensions of the tire are: the tread width, the rim radius, the rim width and the side-wall length.

All the other coefficients in the model are the same (stiffness, damping, etc.) for all the simulations. First of all it is possible to notice that for larger rim radius the rolling resistance coefficient is smaller, and this effect is verified in reality. In the same way, if the ratio between the side-wall length and the tread width decreases (thus the sidewall length decreases, maintaining constant the tread width) the rolling resistance coefficient increases significantly. For a bigger tread width the rolling resistance coefficient is smaller, this because the contact patch has a larger width, thus the application point of the vertical load is less shifted forward. The rim width has no direct effect on the rolling resistance, however, the rolling coefficient of a small rim width tire is more sensible to camber angle, since it increases more maintaining constant the camber angle (line 2 and 5).

Table 6.1: Rolling resistance coefficient for different geometries

Rim Diameter [in]	Tread Width [in]	Rim Width [in]	Sidewall length / Tread Width	f_r for $\gamma = 0°$	f_r for $\gamma = 5°$	Δ
17	255	8	0.55	0.0195	0.0208	+6.67%
17	225	8	0.55	0.0201	0.0213	+5.97%
17	225	8	0.35	0.0221	0.0233	+5.43%
17	225	7	0.35	0.0221	0.0234	+5.88%
17	225	7	0.55	0.0201	0.0214	+6.47%
15	225	8	0.55	0.0211	0.0224	+6.16%
15	225	8	0.35	0.0234	0.0247	+5.55%

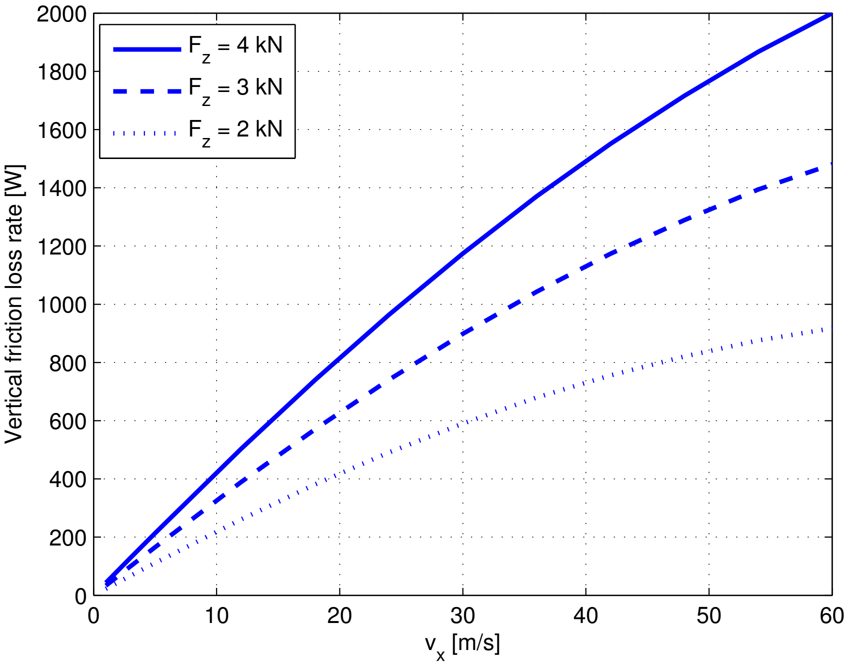

Figure 6.18: Energy dissipation rate by friction elements along the z-axis for different vertical loads

6.2.5 Energy losses

In this section the energy losses, both internal and external, are studied and discussed.

Internal Loss

The internal losses are represented by that fraction of energy dissipated inside the *rubber element*. How to calculate them has already been discussed in paragraph 5.9.2.

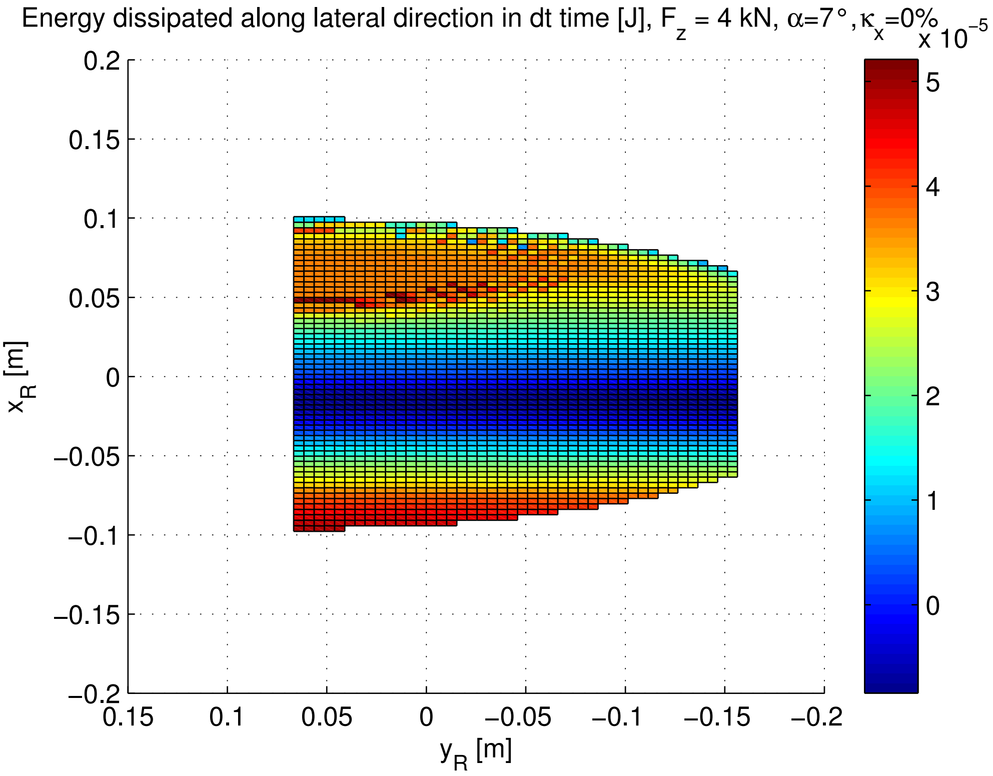

Figure 6.19: Energy dissipated along the lateral direction in the time interval dt, $\alpha = 7°$

Figure 6.18 shows the power dissipated by internal friction (from the Masing model) in the rubber element along the z-axis for different longitudinal speeds and different vertical loads. The dependence on the vehicle speed and the vertical load is obvious: if the wheel rolls faster, it turns more times per unit of time, thus the bristles deflect more often, increasing the power dissipated by internal friction. However it is not linear, and this reflects the behaviour of the rolling resistance coefficient with the vehicle speed (see Figure 6.15). Moreover it is almost linear with the vertical load.

Figure 6.19 shows the energy dissipated by internal friction (thus inside the *rubber elements*) along the lateral direction for $\alpha = 7°$ in the interval time $dt = 0.0005$ s. It's possible to observe that the largest part of the energy dissipated is situated on the trailing and on the leading edge of the contact patch, this because those are the places where the deflection rate is maximum. Instead of the center part, where the deflection reaches its maximum, but its rate is very low.

In Figure 6.20 the lateral power loss by internal friction and the total (visco-elastic and friction) lateral internal power loss are shown as function of the camber angle. The curves shapes reflect the shape of the force-slip diagram. The internal power loss increases in the first region, where the bristles are sticking and it is constant where the bristles are sliding. However, the total (friction plus visco-elastic) power loss for a cambered wheel is slightly lower than the non-cambered tire in the sliding region. This could

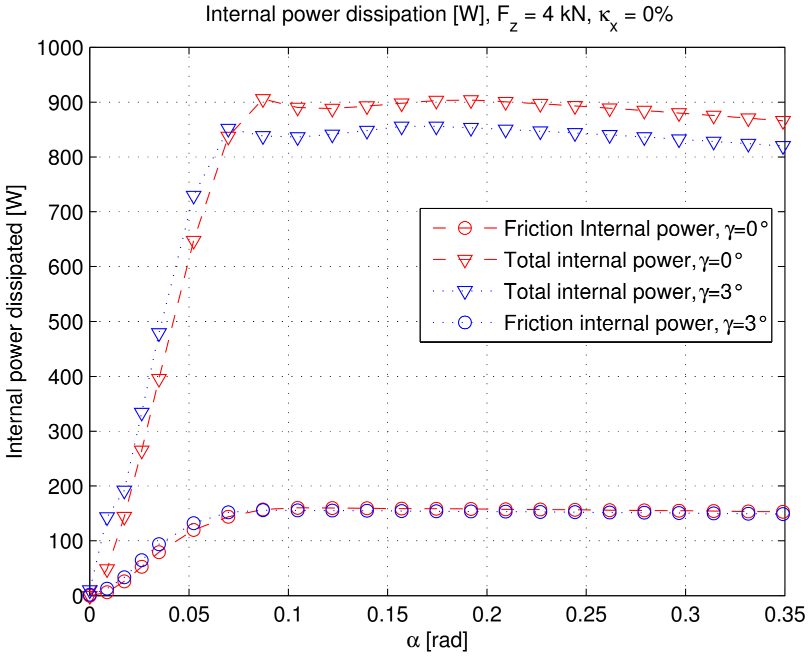

Figure 6.20: Total internal power loss and internal friction power loss for different side slip angle α and camber angle γ along the lateral direction

happen since for a cambered tire with a side slip angle different than zero the distribution of the lateral deflection along the contact patch is more uniform.

It's interesting to compare the total internal friction power loss, i.e. the sum of the power dissipated by internal friction along the three directions, for different camber angles and different side slip angles. However, since for a certain side slip angle the lateral force developed is function of the camber angle, the total power dissipated by internal friction has been normalized on the lateral force developed, as can be seen in Figure 6.21. The ratio of the power loss on the lateral force is smaller for a cambered wheel than for an non-cambered wheel, thus the power dissipated to obtain a certain value of lateral force is smaller for a cambered wheel. Further more simulations should be done in order to find the optimal camber angle to minimize the internal friction power loss.

In Figure 6.22 the longitudinal friction power loss $\dot{W}_{f,x}$ is shown, function of the longitudinal slip κ_x. It's important to notice that the value of the longitudinal slip κ_x affects the value of the angular wheel speed ω. In effect for $\kappa_x = -1$ the angular wheel speed is $\omega = 0$, thus the friction loss becomes null. That is why in Figure 6.22b the friction loss has been normalized on the angular speed. In this last graph, it shows a certain symmetry between the positive and negative values of longitudinal slip. As said for the friction loss for the y-axis, the peak corresponds to the maximum force generated, then it decreases.

The behaviour of the friction power losses has a predictable behaviour, thus the friction power is maximum where the force generated, thus the

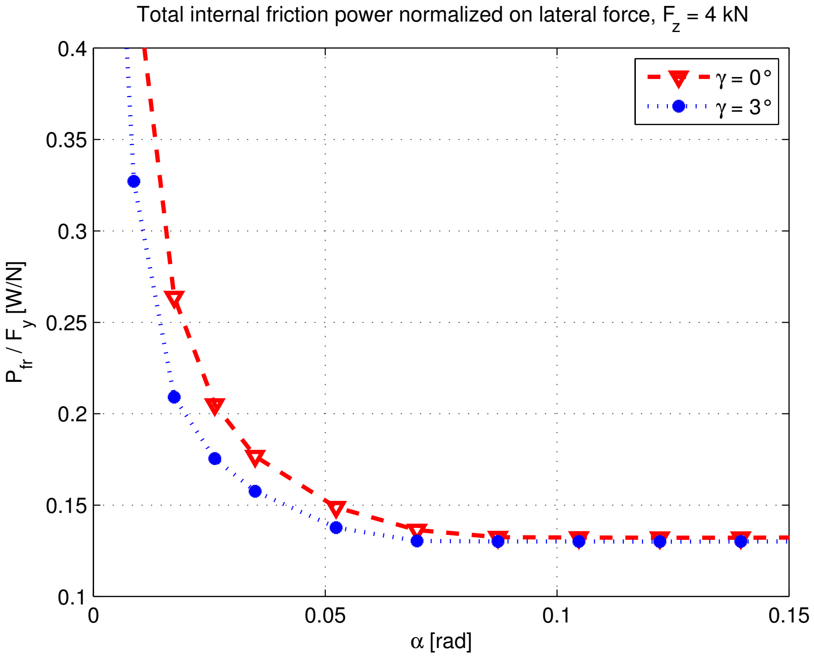

Figure 6.21: Total internal friction force normalized on the lateral force

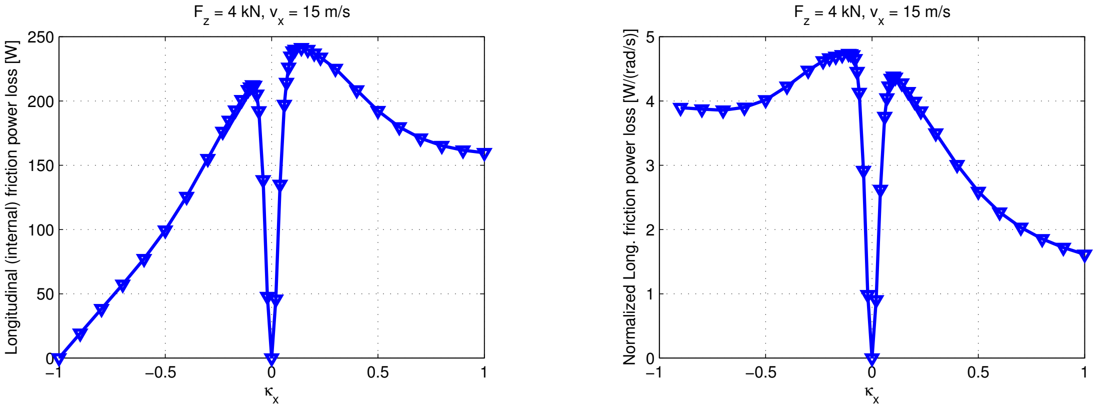

(a) $\dot{W}_{f,x}$ **(b)** $\dot{W}_{f,x}/\omega$

Figure 6.22: Longitudinal friction power loss $\dot{W}_{f,x}$ in 6.22a, normalized with the wheel rotational speed ω in 6.22b

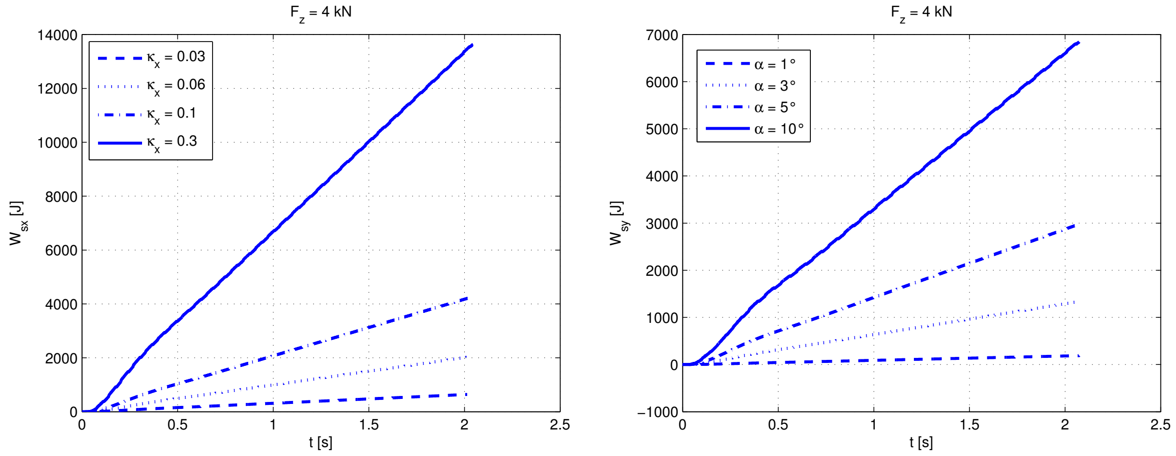

(a) $W_{s,x}$ **(b)** $W_{s,y}$

Figure 6.23: Sliding energy in the x-axis in 6.23a, in the lateral direction in 6.23b

bristle deflection, is maximum.

External loss

The external losses are represented by that part of energy dissipated outside the *rubber element*, i.e. the sliding between the tire and the road.

In Figure 6.23 the energy dissipated by sliding for different slip on the time is shown. Obviously the energy dissipated increases with increasing the slip. The energy dissipated during the sliding between the tire and the road is mainly converted in heat and wear.

Lateral sliding

In Figure 6.24 two different situations are shown, both for a side slip angle of 3°. In Figure 6.24a the local power dissipation, due to sliding, is shown in the contact patch, for a null camber angle. It's possible to see how the most part of the energy dissipated is located near the edge of the contact patch. This because the carcass is deflected, thus the vertical load is shifted to the side opposite to the curving direction. In Figure 6.24b the wheel has a camber angle equal to 2°, thus it generates more lateral force, but, most of all, it shows a more even power dissipation along the contact patch, focused more in the center of the contact patch. This allows a more even wear and heat distribution. The blue area is the sticking region, where the sliding power is null.

In the lateral case it is possible to define an output power of the system "tire", that is the product between the lateral speed of the tire and the lateral force developed:

$$P_{y,out} = F_y \cdot v_y \tag{6.1}$$

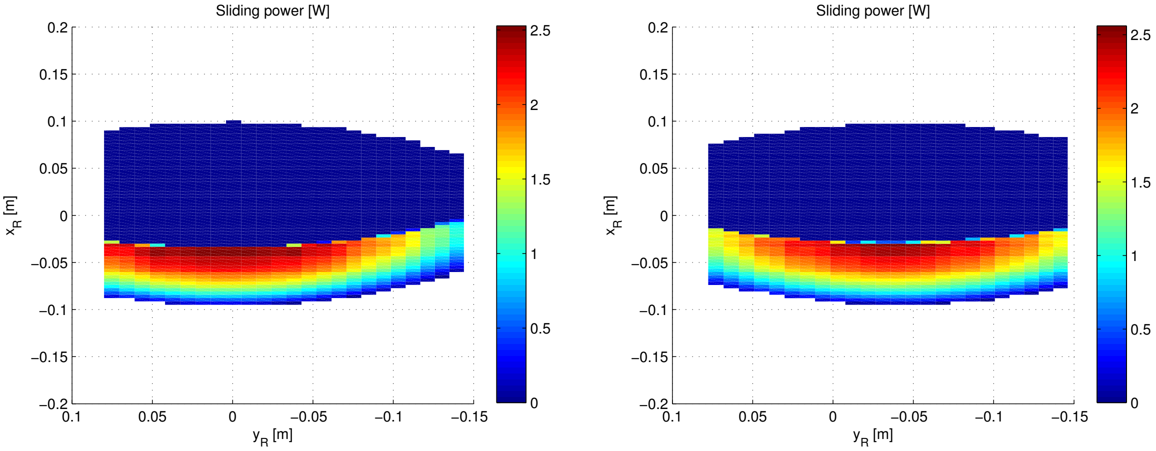

(a) $\dot{W}_{s,y}$, $\gamma = 0°$ **(b)** $\dot{W}_{s,y}$, $\gamma = 2°$

Figure 6.24: Sliding power along the y-axis for a side slip angle $\alpha = 3°$

and a sliding power, defined as the product between the lateral force generated in the sliding region and the sliding velocity of the bristles with road:

$$P_{y,slid} = F_{y,slid} \cdot v_{y,slid} \tag{6.2}$$

In Figure 6.25 they are plotted for different side slip angles and two different camber angles. It's possible to notice that the values between the two camber angles are not so different, both the powers are larger for the cambered wheel, this means that cambering the tire it's possible to obtain an higher value of lateral force, as said in the previous paragraphs.

Longitudinal case

In the longitudinal case the distribution of the power dissipated by sliding has a different shape, as can be seen in Figure 6.26.

The main amount of sliding power is located in the center of the contact patch, this because for high values of slip ratio κ_x the longitudinal force follows the vertical force distribution, because all the bristles are sliding. Thus the maximum of the force is located in the middle, where the vertical force is maximal. In the same way as done before, it's possible to define an output power for the longitudinal case as the product between the longitudinal force and the longitudinal speed of the wheel:

$$P_{x,out} = F_x \cdot v_x \tag{6.3}$$

and the sliding power, defined as before:

$$P_{x,slid} = F_{x,slid} \cdot v_{x,slid} \tag{6.4}$$

However, in this case, it is possible also to define an input power, as the product between the driving torque and the angular speed of the wheel:

$$P_{x,in} = M_y \cdot \omega \tag{6.5}$$

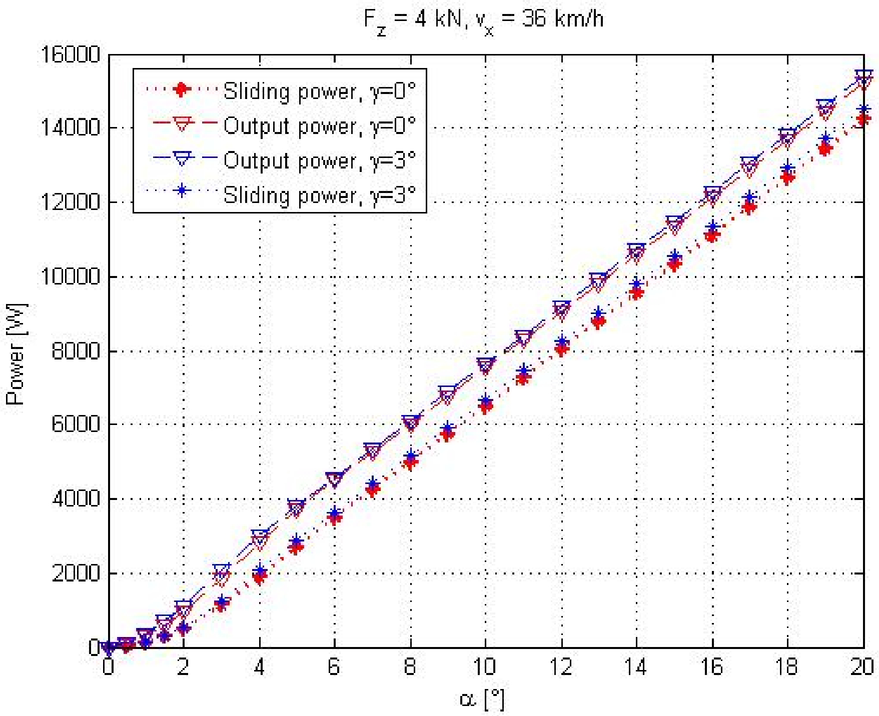

Figure 6.25: Power dissipated by lateral sliding for different camber angles

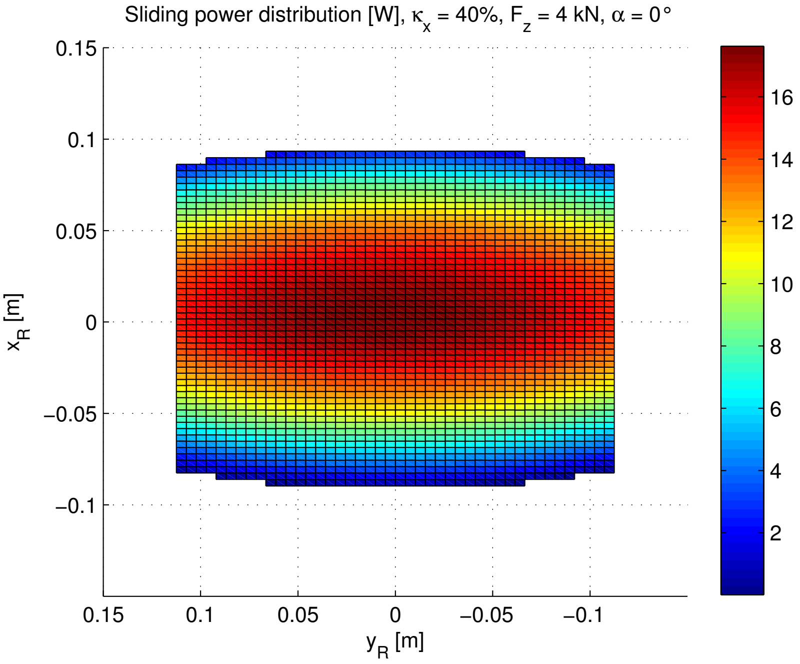

Figure 6.26: Sliding power distribution for $\kappa_x = 40\%$

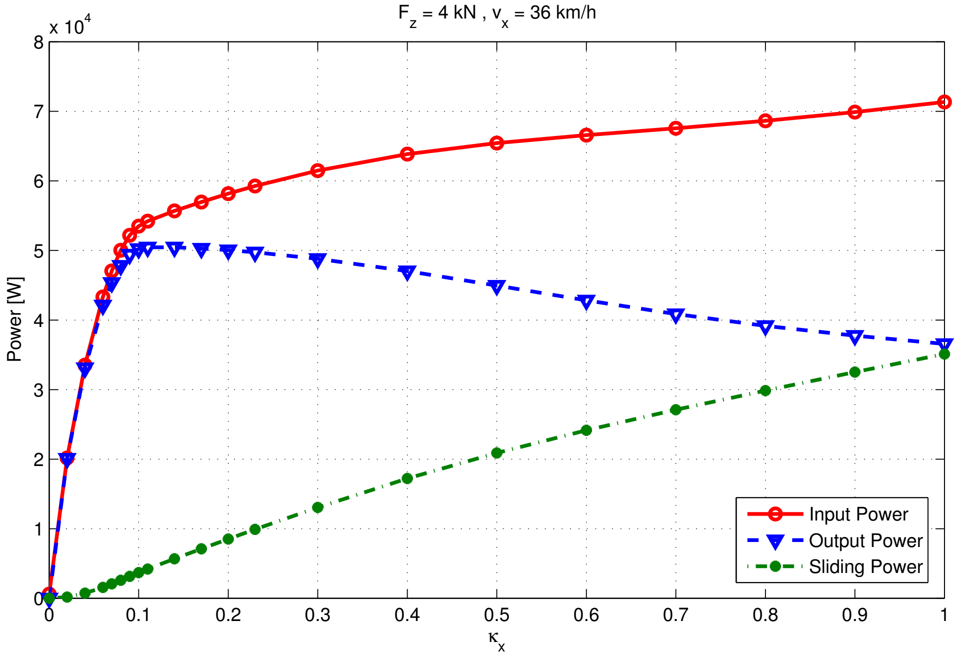

Figure 6.27: Longitudinal input, output and sliding power.

In Figure 6.27 these three powers are diagrammed for different slip ratio κ_x. The input power increases in all the range of the longitudinal slip ratio, even for high values of κ_x. In the same time, the output power in the first part increases, in the same way of the input power, instead in the last part, the output power decreases because of the reduction of the longitudinal force for high values of κ_x. In the same time the sliding power increases in all the range, because of the increasing sliding velocity. Moreover, it results that the output power is not exactly the difference between the input power and the sliding one, because of the power dissipated by internal friction (Masing model), but its amount is almost negligible (less than 1 kW, see previous chapter).

Defining an input and an output power, it is possible to define a sort of efficiency of the wheel, as the ratio between the output and the input power, and it is shown in Figure 6.28. As experience can suggest, it decreases with increasing the slip ratio, but it is not dependent on the vertical load applied to the wheel and on the longitudinal speed. However, it doesn't take into account the internal losses, that characterizes the rolling resistance coefficient.

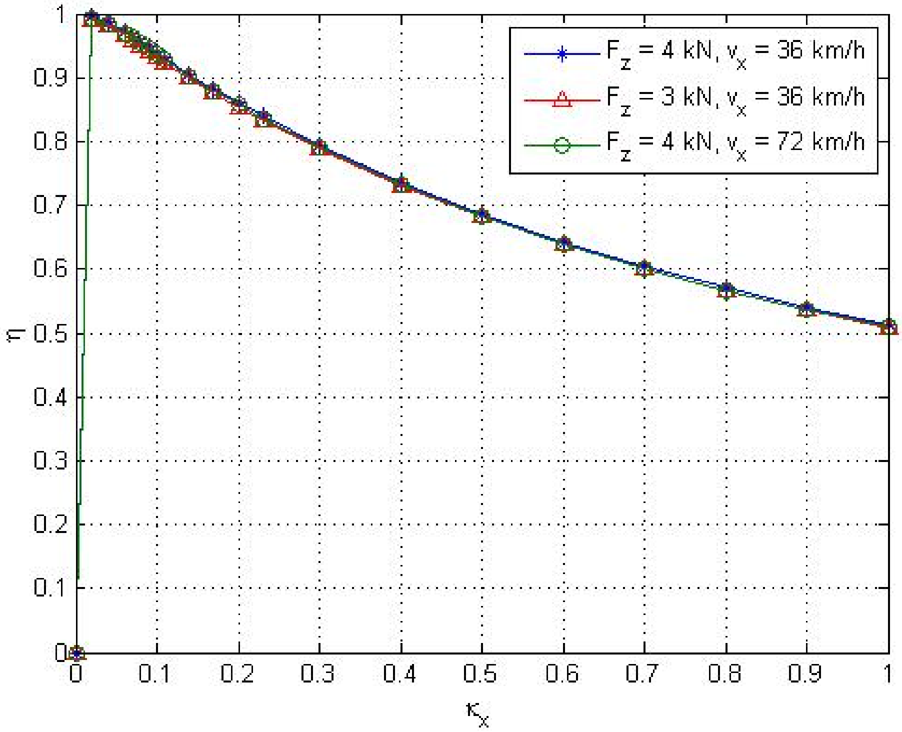

Figure 6.28: Tire efficiency for different slip ratio

Chapter 7

Conclusions and recommendations

In this chapter some conclusions and some recommendations about future work are presented.

7.1 Conclusions

This thesis work has been conducted with the target of studying the energy dissipation in rolling tires. Two different factors are involved in energy dissipation:

- internal losses: these are the losses due to deflection of the tire material, mainly the rubber. The continuous successions of compression and stretching of the material, due to the fact that the tire is rolling, creates hysteresis phenomena that allows the dissipation of energy, mainly transformed into heat;
- external losses: this part is represented by the losses that occur for certain situations, and they are due to the fact that the tread of the tire slides on the road surface, dissipating energy for external friction.

The main aim of this work is the development of a new tire model, the Multi-Line Brush Tire model, which can described these two energy dissipation phenomena for different dynamic situations. The developed model can describe quite well the generation of the rolling resistance force, using the laws of the rubber mechanics, and its behaviour in different dynamics case. The model takes into account the tire geometry as well, which can be a parameter in order to minimize the energy dissipation of a vehicle in motion. In the same way the camber angle could be a parameter that could be varied in order to reduce the internal friction losses when the vehicle is turning.

A lot of other dynamics cases and situations can be studied using the Multi-Line Brush Tire model.

7.2 Drawbacks

The developed Multi-Line Brush Tire model have some drawbacks, that can be corrected in the future:

- number of parameters: comparing to the simple Brush Tire model the number of parameters needed for the Multi-Line Brush Tire model is much higher, this because it can describe phenomena that the simple brush tire model can't, like the dynamic friction between the tread and the road, or the energy analysis;
- numerical instability issues: all the equations in time have been solved using numerical models of the first or second order. This could creates some instability issues in those equations. This problem can be solved by implementing solver relation with a higher order (like Runge-Kutta equations), but this will increase the calculation time;
- not adapt for on-board analysis: since the code divides the contact patch in a certain number of bristles, for each one of them a lot of equations have to be solved for each time step, thus the software (MATLAB) takes 7-8 seconds for a 2 seconds simulation, this disqualifies the model for on-board use.

7.3 Recommended future work

The model can be improved by implementing other features, like a flexible carcass along the vertical and longitudinal direction, or implementing a more high order solver for the numerical equations. In the same way the model can be implemented into a 4 wheel car model, in this way some more generic conclusions about the total energy dissipation in the tires of a vehicle for different dynamics cases can be stated, and the problem about the optimization of the energy loss can be faced. In order to allow the implementation of a on-line control strategy of the wheel parameters (particularly the camber angle) some maps can be created with the model, where the energy dissipation is calculated for different variables (such as longitudinal speed, side slip angle, slip ratio, etc.), with the target of finding the best combination of these parameters to minimize the energy dissipation. These "maps" could be implemented then into the Electronic Control Unit of the vehicle.

Bibliography

[1] *Vehicle Population.* Date visited: May 2014. 2011. URL: `http://wardsauto.com/ar/world_vehicle_population_110815`.

[2] Michael Sayers. *Standard Terminology for Vehicle Dynamics Simulations.* report. 1996.

[3] Sigvard Zetterstrom. “Vehicle wheel suspension arrangement”. U.S. Patent. 2002.

[4] *Road vehicles - Vehicle dynamics and road-holding ability - Vocabulary.* ISO 8855, 1991.

[5] Howard Dugoff, Paul Fancher, and Leonard Segel. *Tire performance characteristics affecting vehicle response to steering and braking control inputs.* Ed. by Michigan Highway Safety Research Institute. 1969.

[6] Hans Bastiaan Pacejka. *Tyre and Vehicle Dynamics.* 2002.

[7] Dieter Schramm, Manfred Hiller, and Roberto Bardini. *Modellbildung und Simulation der Dynamik von Kraftfahrzeugen.* Ed. by Springer. 2010.

[8] Hans Bastiaan Pacejka. *Modeling of pneumatic tyre and its impact on vehicle dynamic behavior.* Ed. by Delft Technische Universiteit. 1972.

[9] Jo Yung Wong. *Theory of ground vehicles.* Ed. by John Wiley and Sons. 2001.

[10] Jacob Svendenius. *Tire modeling and friction estimation.* Master Thesis, Royal Institute of Technology, 2007.

[11] Reza N. Jazar. *Vehicle dynamics, theory and application.* Ed. by Springer. 2008.

[12] David Roylance. *Engineering Viscoelasticity.* Ed. by Massachusetts Institute of Technology. 2001.

[13] Marc Andre Meyers and Krishan Kumar Chawla. *Mechanical behavior of Materials.* Ed. by Inc. Prentice Hall. 1999.

[14] Magnus Lahti. *Modelling Rubber Bushings.* Master Thesis, Royal Institute of Technology, 2004.

[15] Mohammad Mehdi Davari et al. *Investigating the potential of wheel corner modules in reducing rolling resistance of tires.* Ed. by FISITA. Maastricht, Netherland, 2014.

[16] Mats Berg. “A Non-Linear Rubber Spring Model for Rail Vehicle Dynamics Analysis”. In: *Vehicle System Dynamics: International Journal of Vehicle Mechanics and Mobility* (2007).

[17] Dodge Clark. *A Handbook for the rolling resistance of pneumatic tires.* Ed. by Institute of science Industrial development division and University of Michigan technology. 1979.

Appendix A

Force code implementation

In this appendix the formula used to implement the rubber model equation in Matlab are explained and discussed.

A.1 Visco-elastic force

The differential equation for the calculus of the force developed by the visco-elastic parts has been presented in Chapter 4.2.1. In particular, since in the model the Three Parameters Maxwell model has been used, the equation to be analysed is equation 4.4, here reported:

$$\dot{\sigma}(t,\varepsilon) = -\frac{k_2}{c}\sigma(t) + \frac{k_1 k_2}{c}\varepsilon(t) + (k_1 + k_2)\dot{\varepsilon} \tag{A.1}$$

where, referring to Figure 4.4a:

- $\sigma(t)$ is the force developed by the system along one axis (x-, y- or z-axis);
- $\varepsilon(t)$ is the deformation applied to the model along one axis (x-,y- or z-axis);
- k_1 and k_2 are the stiffness of the elastic springs;
- c is the viscous coefficient of the damping;

In the model the deformation ε is the input, and the output is the force developed. As it is possible to see that the derivative of the force is a function of the derivative of the deformation, thus an analytical solution is quite tough to be found. That's why a numerical solution is used instead of the analytical one, in order to simplify the calculation, even with a final error due to the numerical solution.

The method adopted is the Crank-Nicolson method for the solution of the differential Equation 4.4. It's a second order method in time, implicit and numerically stable, consisting in a combination of the forward Euler method and the backward Euler method. The differential equation 4.4 can be written in this form:

$$\dot{\sigma}(t,\varepsilon) = F\left(\sigma,\varepsilon,t\right) \tag{A.2}$$

Assuming that Δt is the time-step interval, the equation A.2 can be approximated with:

$$\frac{\sigma_{t+\Delta t} - \sigma_t}{\Delta t} \approx \frac{1}{2}\left(F_{t+\Delta t}\left(\sigma, \varepsilon, t\right) + F_t\left(\sigma, \varepsilon, t\right)\right) \tag{A.3}$$

where:

- $\sigma_{t+\Delta t}$ is the force developed at the time $t + \Delta t$, thus it is the unknown variable;
- σ_t is the force developed in the time t, it's known since it is the initial condition of the differential problem;
- $F_{t+\Delta t}$ is the Equation 4.4 calculated at the time $(t + \Delta t)$;
- F_t is the same function calculated in the time t;

The derivative of the deflection ε is approximated with a first-order Euler method, thus:

$$\dot{\varepsilon}_{t+\Delta t} \approx \frac{\varepsilon_{t+\Delta t} - \varepsilon_t}{\Delta t} \tag{A.4a}$$

$$\dot{\varepsilon}_t \approx \frac{\varepsilon_t - \varepsilon_{t-\Delta t}}{\Delta t} \tag{A.4b}$$

Here the first order is used since the value of the next step of the deflection is unknown, in fact it is calculated from the value of the force, that is the product of code.

Using Equation A.4 in Equation A.3 the final relation implemented in Matlab is obtained:

$$\sigma_{t+\Delta t} = \left(\frac{c}{2c + k_2\Delta t}\right)\Big((2 - k_2\Delta t/c)\sigma_t + (k_1k_2\Delta t/c + k_1 + k_2)\varepsilon_{t+\Delta t} + (k_1k_2\Delta t/c)\varepsilon_t - (k_1 + k_2)\varepsilon_{t-\Delta t}\Big) \tag{A.5}$$

The Equation A.5 is calculated for each time step, and the output of one time step became the input of the next time step.

A.2 Friction force

The model used for the estimation of the internal friction forces is the Masing model, explained in the paragraph 4.2.2. It consists of five spring plus dashpots elements in parallel (Figure 4.6), thus five equations are needed to be solved for each time step.

The general equation for the Masing model is:

$$\sigma(\varepsilon) = \sum_{i=1}^{n} \sigma_i(\varepsilon(t)) \tag{A.6}$$

where σ_i is the force of the i:th Jenkin element, thus:

$$\dot{\sigma}_i = \begin{cases} k_i\dot{\varepsilon} & |\sigma_i| < R_i \text{ or } (|\sigma_i| = R_i \text{ and } sgn(\dot{\varepsilon}\sigma_i)) \leq 0 \\ 0 & \text{else} \end{cases} \tag{A.7}$$

where ε is the deformation applied to each Jenkin element (equal for all of them, since the elements are connected in parallel), it could be along the x-, y- or z-axis; σ_i is the force developed by the i:th Jenkin element; R_i is the static Coulomb friction force of the i:th Jenkin element; k_i is the stiffness of the spring in the Jenkin element.

Defining the incremental deflection as $\Delta\varepsilon = \varepsilon_{t+\Delta t} - \varepsilon_t$ the Equation A.7 is implemented in Matlab in this way:

$$\sigma_{i,tr} = \sigma_i + k_i\Delta\varepsilon \tag{A.8a}$$

$$\sigma_i = \Big((|\sigma_{i,tr}| > R_i) \cdot sign(\sigma_{i,tr}) \Big) \cdot R_i + \Big(|\sigma_{i,tr}| \leq R_i \Big) \cdot \sigma_{i,tr} \tag{A.8b}$$

The $\sigma_{i,tr}$ is a trial value of the friction force, if it is larger than the static friction force R_i, it becomes equal to the same R_i, and this behaviour is described by Equation A.8b. The absolute values are needed to make the relation works for both negative and positive velocities.

It's important to notice that the Equation A.8b is not linear, but *piecewise* defined. Thus the result is not smooth.

Appendix B

Magic Formula Tire Model implementation

B.1 Longitudinal slip

In this appendix the values of the coefficients of the Magic Formula used in this work are listed. It is divided into two sections: in the first part the coefficients for the longitudinal slip diagram are listed, as well as in the second part the coefficients values for the lateral slip are listed.

```
% Magic Formula for longitudinal slip
Fz=2000;    %Vertical load
F_z0=4000;  %Nominal vertical load
p_Cx1=1.685;
p_Dx1=1.21;      p_Dx2=-0.037;
p_Ex1=0.344;     p_Ex2=0.095;     p_Ex3=-0.02;     p_Ex4=0;
p_Hx1=-0.002;    p_Hx2=0.002;
p_Kx1=21.51;     p_Kx2=-0.163;    p_Kx3=0.245;
p_Vx1=0;         p_Vx2=0;
lambda_Hx=0;     lambda_Vx=0;
dfz=(Fz-F_z0)/F_z0;
mu_x=p_Dx1+p_Dx2*dfz;
Dx=mu_x*Fz;
Cx=p_Cx1;
Kxk=Fz*(p_Kx1+p_Kx2*dfz)*exp(p_Kx3*dfz);
Bx=Kxk/(Cx*Dx+eps);
Shx=(p_Hx1+p_Hx2*dfz)*lambda_Hx;
Svx=Fz*(p_Vx1+p_Vx2*dfz)*lambda_Vx;

Ex=@(k)(p_Ex1+p_Ex2*dfz+p_Ex3*dfz^2)*(1-p_Ex4*sign(k+Shx));

Fx=@(k)Dx*sin(Cx*atan((Bx*(k+Shx)-
     (p_Ex1+p_Ex2*dfz+p_Ex3*dfz^2)*(1-p_Ex4*sign(k+Shx))*
     *(Bx*(k+Shx)-atan(Bx*(k+Shx))))))+Svx;
```

B.2 Lateral slip

```
% Magic Formula for lateral slip
Fz=9.82*200*1;
gamma=0*pi/180;
R_0=0.3;
F_z0=4000;
Vxc=16;
p_Cy1=1.193;
p_Dy1=-0.99;    p_Dy2=0.145;   p_Dy3=-11.23;
p_Ey1=-1.033;   p_Ey2=-0.537;  p_Ey3=-0.083;   p_Ey4=-4.787;   p_Ey5=0;
p_Hy1=0.001;    p_Hy2=-0.001;  p_Hy3=0;
lambda_Hy=0;    lambda_Vy=0;
p_Ky1=-14.95;   p_Ky2=2.130;   p_Ky3=-0.028;   p_Ky4=2;
p_Ky5=0;    p_Ky6=-0.92;    p_Ky7=-0.24;
p_Vy1=0.045;    p_Vy2=-0.024;  p_Vy3=-0.532;   p_Vy4=0.039;

dfz=(Fz-F_z0)/F_z0;
mu_y=(p_Dy1+p_Dy2*dfz)*(1-p_Dy3*gamma^2);
D_y=mu_y*Fz;
C_y=p_Cy1;
K_ysy=p_Ky1*F_z0*sin(2-atan(Fz/(p_Ky2*F_z0)))*(1-p_Ky3*abs(gamma));
B_y=K_ysy/(C_y*D_y+eps);
S_Hy=(p_Hy1+p_Hy2*dfz)*lambda_Hy+p_Hy3*gamma;
S_Vy=Fz*((p_Vy1+p_Vy2*dfz)*lambda_Vy+gamma*(p_Vy3+p_Vy4*dfz));

Ey=@(alfa)(p_Ey1+p_Ey2*dfz)*(1-(p_Ey3+p_Ey4*gamma)*sign(alfa));

Fy=@(alfa)D_y*sin(C_y*atan((B_y*(alfa+S_Hy)-((p_Ey1+p_Ey2*dfz)*
    *(1-(p_Ey3+p_Ey4*gamma)*sign(alfa))*(B_y*(alfa+S_Hy)-
    atan(B_y*(alfa+S_Hy)))))))+S_Vy;
```

Appendix C

Pirelli test, Multi-Line Brush Tire model coefficients

Here the values of the Multi-Line Brush Tire model coefficients used to fit the Pirelli test data are shown.

```
B=0.225;                    %Width of the tire [m]
w_r=7*25.4*0.001;           %Rim width [m]
S_w=w_r*0.45;               %Length of the tire side wall [m]
R_r=17/2*25.4*0.001;        %Radius of the tire rim [m]

load_sensitivity_y=0.15;
load_sensitivity_x=0.1;
cpx = 2578500/n/lines;      %Longitudinal bristle stiffness [N/m]
cpy = 2664450/n/lines;      %Lateral bristle stiffness [N/m]
cpz = 1117350/n/lines;      %vertical bristle stiffness [N/m]
dpx = 133/n/lines;          %Longitudinal damping for each bristle [Ns/m]
dpy = 133/n/lines;          %Lateral damping for each bristle [Ns/m]
dpz = 38/n/lines;           %Vertical damping for each bristle [Ns/m]

k_rs=600;            %torsional stiffness carcass
d_rs=10;             %Damping carcass

k=45000;         %Spring suspension stiffness[N/m]
d=1000*5;        %Damping suspension car     [Ns/m]

%% Friction tire-Ground
%longitudinal friction
mux_s=1.3;          % Static friction coefficient
mux_c=1.05;         % Coulomb friction coefficient
vx_str=3.5;         % Stribeck velocity

%lateral friction
muy_s=1.24;         % Static friction coefficient
muy_c=0.9;          % Coulomb friction coefficient
vy_str=2;           % Stribeck velocity
```